The Effect of Cloud Type on Earth's Energy Balance

Author:

Yun Hang

Advisor:

Dr. Tristan S. L'Ecuyer

A thesis submitted in partial fulfillment of

the requirements for the degree of

Master of Science

(Atmospheric and Oceanic Sciences)

at the

UNIVERSITY OF WISCONSIN-MADISON

May 2016

Abstract

The Effect of Cloud Type on Earth's Energy Budget

by Yun Hang

Clouds have long been recognized as one of the largest uncertainties to Earth's changing energy budget. Previous research indicates that improved assessment of cloud impacts on climate requires a better understanding of individual cloud types and their radiative effects. This work documents the effects of nine distinct cloud types on atmospheric radiative balance and heating using 2007-2010 data from CloudSat's multi-sensor radiative fluxes and heating rates product (FLXHR-LIDAR). This dataset leverages high-resolution vertical cloud and aerosol information from CloudSat and CALIPSO to provide the most accurate estimates of vertically-resolved radiative fluxes available to date. The effects of three common cloud classes will be highlighted in detail: cirrus, stratocumulus, and deep convection, to contrast their dramatically different effects on climate. The findings support the qualitative conclusion that cirrus clouds warm the planet and stratocumulus clouds cool the planet, while the longwave and shortwave cloud radiative effect of deep convective cloud cancel each other in the tropics. In addition, cloud types will be regrouped in order to compare the results with classical cloud classifications based on passive sensors including those from the International Satellite Cloud Climatology Project (ISCCP) and Earth Radiation Budget Experiment (ERBE) archives. The new CloudSat/CALIPSO estimate of annual average shortwave forcing is -53 W/m^2 in good agreement with previous estimates

but CloudSat/CALIPSO observations suggest a 20% lower longwave forcing than other sources. This analysis provides an improved distinction of the radiative effects of low-level clouds, and the cloud boundary information from the active sensors used greatly enhances our ability to accurately discern cloud forcing at the Earth's surface.

Acknowledgements

I would like to thank many people who have helped me through the completion of this thesis. I express sincere gratitude to my advisor, Tristan L'Ecuyer, whose expertise, kindness, and patience has enriched my graduate experience. His guidance has helped me develop into a better scientific writer, researcher, and critical thinker. I could not imagine a better advisor and mentor for my graduate studies.

In conjunction with the mentorship of my advisor, I am grateful to work with dynamic and intelligent committee members Grant Petty and Pao Wang and appreciate their inputs, insights, and feedback to make this work better. Completion of this thesis would not be possible without the support of AOS faculty, administrators, students, and staff and I appreciate all of their helpful guidance through this process.

I am grateful for the technical support from Pete Pokrandt, who has helped me solve computer and printer problems over the past three years. I would like to thank Alex Matus whose advice and tips in data processing has been invaluable. I am grateful to collaborate with such talented graduate students and officemates whose peer support have helped me along the way. I extend my deepest gratitude to my family for the constant encouragement and support they have provided me.

Contents

3 Data and Methodology

4 Global Observations

5 Advances Relative to Previous Assessments

6 Summary and Future Work

List of Figures

List of Tables

Abbreviations

Ac	Altocumulus
As	Altostratus
AR5	Fifth Assessment Report of the IPCC
CALIOP	Cloud–Aerosol Lidar with Orthogonal Polarization
CALIPSO	Cloud Aerosol Lidar and Infrared Pathfinder Satellite Observation
CF	Cloud Fraction
Ci	Cirrus
CMIP5	the Fifth phase of the Coupled Model Intercomparison Project
CPR	Cloud Profiling Radar
CRE	Cloud Radiative Effect
CRH	Cloud Radiative Heating
Cu	Cumulus
DJF	December-January-February
D.C.	Deep Convective Cloud
ECMWF	European Centre for Medium-range Weather Forecasting
EH	Eastern Hemisphere
ERBE	Earth Radiation Budget Experiment

GCM	General Circulation Model
hPa	hectoPascals
IPCC	Intergovernmental Panel on Climate Change
ITCZ	Intertropical Convergence Zone
JJA	June-July-August
K	Kelvin
km	kilometer
LW	Longwave
LWP	Liquid Water Path
m	meter
M.L.	Multi-layered Cloud
NH	Northern Hemisphere
Nb/Ns	Nimbostratus
SH	Southern Hemisphere
St	Stratus
Sc	Stratocumulus
SW	Shortwave
TOA	Top of Atmosphere
WH	Western Hemisphere

Symbols

$F^{\uparrow}$	upward broadband flux	W m^{-2}
$F^{\downarrow}$	downward broadband flux	W m^{-2}
F_{net}	net flux, defined as $F^{\uparrow}$ - $F^{\downarrow}$	W m^{-2}
C_P	specific heat capacity	J kg^{-1} K^{-1}
ρ	air density	kg m^{-3}

Chapter 1

Introduction

1.1   Overview of Cloud Types

Clouds are masses of liquid water, ice, or mixtures of both phases suspended in the atmosphere. The temperature, wind, and different condensation nuclei form the shape, size, and texture of clouds. The dynamics and features of clouds are accurate indicators of important atmospheric properties, including air stability, moisture content, and its role in energy balance.

Cloud classification began with Lamarck in France and Howard in England. Luke Howard (1772-1864) originated a cloud classification in 1803 in a famous talk on "Cloud Modification". J. B. de Lamarck (1744-1839), better known for an erroneous theory of inheritance, an inveterate classifier, put forward a classification based mainly on height. In meteorology, clouds are commonly divided into four clouds families: high-level clouds (5-13 km), mid-level clouds (2-7 km), low-level clouds (0-2 km) and clouds with large vertical extent (0-13 km).

Previous studies of clouds that focused on their radiative forcing have improved the parameterization of clouds in General Circulation Models (GCMs) and improved the understanding of the role of clouds in the Earth-atmosphere climate system (Hartmann et al., 1992). Fig. 1.1 shows the nine cloud types that constitute one modern cloud classification scheme and Table 1.1 presents their features including clouds base, rainfall, horizontal or vertical dimension, and liquid water path (LWP; Wang et al. 2013).
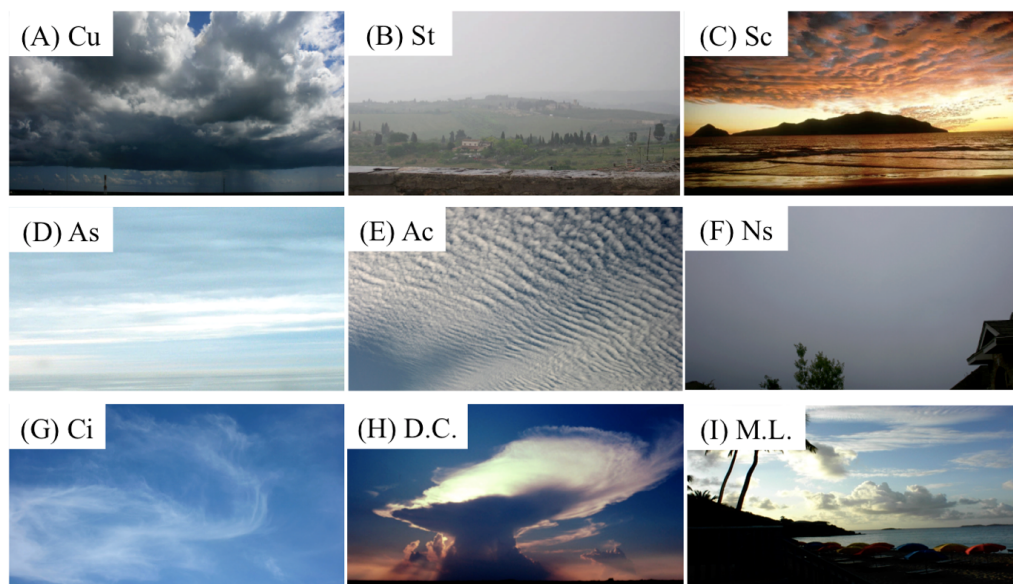
Figure 1.1 Cloud types: (A) cumulus, (B) stratus, (C) stratocumulus, (D) altostratus, (E) altocumulus, (F) nimbostratus, (G) cirrus, (H) deep convective clouds, (I) multi-layered clouds.

Cloud Class	Cloud Features	
High Cloud	Base	> 7.0 km
	Rain	no
	Horiz. Dim.	1 to 10^3 km
	Vert. Dim.	moderate
	LWP	= 0.
As	Base	2.0-7.0 km
	Rain	none
	Horiz. Dim.	10^3 km, homogeneous
	Vert. Dim.	moderate
	LWP	$\sim$ 0, dominated by ice
Ac	Base	2.0-7.0 km
	Rain	virga possible
	Horiz. Dim.	10^3 km, inhomogeneous
	Vert. Dim.	shallow or moderate
	LWP	> 0
St	Base	0-2.0 km
	Rain	none or slight
	Horiz. Dim.	10^2 km, homogeneous
	Vert. Dim.	shallow
	LWP	> 0.
Sc	Base	0.-2.0 km
	Rain	drizzle or snow possible
	Horiz. Dim.	10^3 km, inhomogeneous
	Vert. Dim.	shallow
	LWP	> 0.
Cu	Base	0-3.0 km
	Rain	drizzle or snow possible
	Horiz. Dim.	1 km or larger, isolated
	Vert. Dim.	shallow or moderate
	LWP	> 0.
Nb	Base	0-4.0 km
	Rain	prolonged rain or snow
	Horiz. Dim.	50 -1000 km
	Vert. Dim.	thick
	LWP	> 0.
Deep convective clouds	Base	0-3.0 km
	Rain	intense shower of rain or hail possible
	Horiz. Dim.	10 km or large
	Vert. Dim.	thick
	LWP	> 0.

Table 1.1 Cloud types features (Wang et al., 2013).

Cumulus (Cu), stratus (St) and stratocumulus (Sc), Fig. 1.1a-c, are low-level clouds. As illustrated in Table 1.1, these clouds' bases are less than 3 km, where cloud tops are always warm and gray due to their low height and high

moisture. Cu clouds experience vertical growth, unlike St and Sc clouds, and appear relatively big and fluffy, like giant cotton balls in the sky. St clouds appear uniformly gray in color and look like fog that doesn't reach the surface. Sc clouds are relatively low, lumpy, and gray, with large horizontal scale around 5-50 km.

In Fig. 1.1d-f, altostratus (As), altocumulus (Ac) and nimbostratus (Ns/Nb) are mid-level clouds with cloud bases lower than 7 km but higher than 2-3 km. Their tops are frequently the hardest to differentiate in satellite imagery, so scientists rely heavily on computers and additional information to identify mid-level clouds.

Altostratus clouds can float like parallel strips of clouds. They appear gray or blue-gray, and are sometimes thin enough to reveal the sun. These clouds are often indicative of a coming storm with rain or snow. Ac clouds are white or gray and generally layered with one part darker than the other. Ac clouds are generally accompanied by other clouds, and the presence of Ac clouds in the morning hours often indicates possible thunderstorms in the afternoon. Ns clouds are thick, continuous, rain clouds that appear dark gray.

Fig. 1.1g shows cirrus (Ci) clouds, which are high-level clouds with bases higher than 7 km, causing them to be composed of ice crystals. Ci clouds are thin and light and often flow with the wind. High cloud tops are cold and

almost always bright. Fig. 1.1h shows deep convective (D.C.) clouds, which are many kilometers thick and high, typified by cumulonimbus clouds with bases near the surface and cloud tops always higher than 10 km. Fig. 1.1i shows multi-layered (M.L.) clouds, which are fairly common in the tropics. M.L. clouds have both low Cu clouds and high Ci clouds present.

1.2   Climate Effects of Clouds

Depending on their characteristics and height in the atmosphere, clouds' most important roles in climate are (i) transporting water from one place to another, and (ii) influencing the energy balance and latent heating in regulating Earth's temperature through their effects on sunlight and infrared light through atmosphere. These effects are illustrated in Fig. 1.2 where it is shown that clouds reflect 20% of incoming solar energy and absorb 3%. The fraction of solar energy that is reflected back to space is called albedo. Albedo is depends on surface. For example, ocean surface and rain forests have low albedo while deserts, ice, and clouds have high albedos. The cloud reflects more shortwave radiation back to space than the surface would in the absence of the cloud. At the heart of the difficulty in understanding how clouds affect climate is that clouds both cool and heat the planet. During the day, clouds reflect sunlight and

keep Earth cooler. During the night, clouds trap upwelling heat back to the surface and keep Earth warmer. Another difficulty in understanding clouds' affect on climate is that clouds can warm and dry Earth's atmosphere as well as supply water to the surface by forming precipitation.

EARTH'S ENERGY BUDGET

Reflected by atmosphere 6%
Reflected by clouds 20%
Reflected from earth's surface 4%
64%
6%

Incoming solar energy 100%

Radiated to space from clouds and atmosphere

Absorbed by atmosphere 16%

Radiated directly to space from earth

Absorbed by clouds 3%

Radiation absorbed by atmosphere 15%

Conduction and rising air 7%

Carried to clouds and atmosphere by latent heat in water vapor 23%

Absorbed by land and oceans 51%

Figure 1.2 Earth's energy budget (Kiehl and Trenberth, 1997).

Clouds affect the climate but changes in the climate also affect clouds. Clouds are created by motions in atmosphere; if the climate changes, then cloud effects would change as a result. Any change in a cloud process that is caused by climate change in turn influences climate, representing a cloud–climate

feedback. Because clouds interact so strongly with both solar radiation and terrestrial radiation, small changes in cloudiness can have a large effect on the climate system.
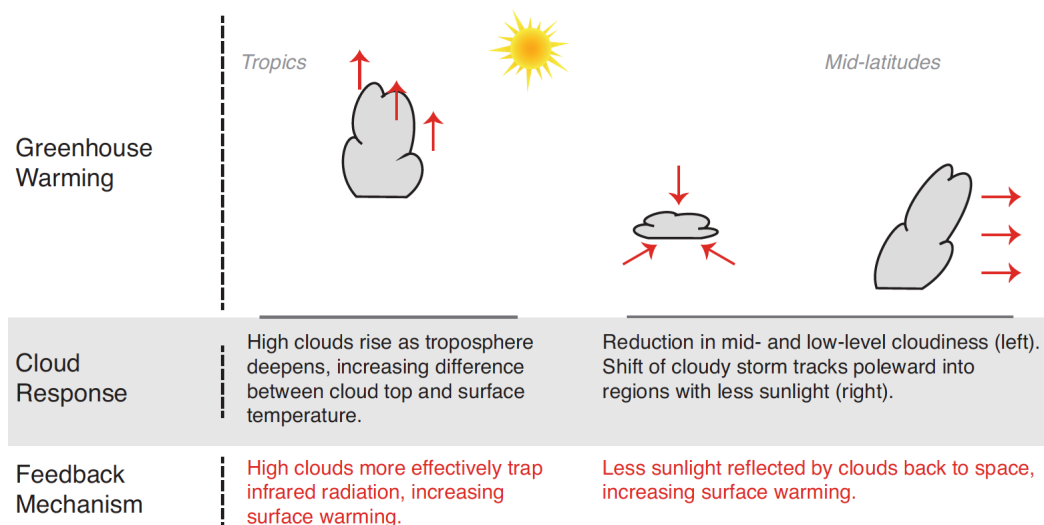
Figure 1.3 Cloud feedback mechanisms (IPCC AR5).

Three types of cloud–climate feedbacks are illustrated in Fig. 1.3 (IPCC AR5). The temperature difference between high clouds' cold cloud tops and the surface is large, trapping more infrared radiation and in turn increasing surface warming. In addition, reduction in mid- and low-level cloudiness and shifts of cloudy storm tracks poleward into regions with less sunlight result in less sunlight reflected by clouds back to space, also increasing surface warming.

1.3   Cloud Radiative Effects

Atmospheric scientists have learned a great deal in past decades about how clouds form and move, but clouds' radiative role in energy balance is still not well understood. This study will focus entirely on assessing cloud radiative effects (CRE) using state-of-the-art satellite observations. CRE refers to the impacts of clouds on radiative fluxes, also called cloud radiative forcing (Ramanathan et al., 1989; Henderson et al., 2013), defined as

$$CRE = (F^\uparrow - F^\downarrow)_{\text{Clear}} - (F^\uparrow - F^\downarrow)_{\text{All-Sky}} \qquad (1.1)$$

where $F^\uparrow$ and $F^\downarrow$ are upward and downward fluxes in clear-sky and all-sky conditions in atmosphere, respectively. The all-sky radiative energy values include clear and cloudy observations. The difference between the radiative energy budgets of these two conditions is the CRE. In the shortwave (SW), CRE reduces the absorbed solar radiation which results in a cooling effect on Earth. However, in the longwave (LW), CRE generally reduces radiative emission to space and thus results in a heating effect on Earth. LW CRE is dominated by cold high clouds while SW CRE depends on the available sunlight, making it sensitive to the diurnal and seasonal cycle of cloudiness.
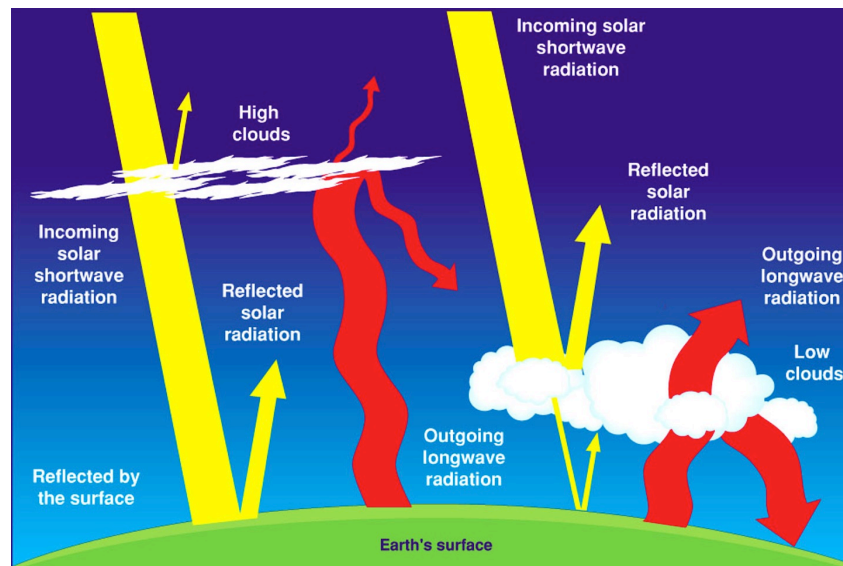
Figure 1.4 CREs of different cloud types (www.climate4you.com)

Fig. 1.4 provides a conceptual illustration of the CREs of different cloud types. A cloud's height in the atmosphere influences how effective it is at trapping outgoing heat. High-level clouds strongly restrict emission out to space resulting in positive CRE while low-level clouds strongly reflect sunlight back to space resulting in negative CRE. However, for thick high clouds, which strongly reflect and restrict emission, these effects cancel resulting in nearly zero net CRE.

1.4   Cloud Radiative Heating

Cloud radiative heating (CRH) is the difference in CRE at TOA minus SFC, which can be used to estimate the impact of clouds on radiative heating within the atmosphere. Clouds affect the earth's climate by modulating the vertical and horizontal distributions of solar radiative heating, latent heating, and cooling by thermal radiation that drive atmospheric circulation (Chen et al., 1999). Although the net impact of clouds on global atmospheric heating is small, they exhibit significant impacts on regional scales that directly interact with large-scale circulation patterns by adjusting the local energy budget (Sohn and Smith, 1992c).

CRH is similar to CRE but does not include feedbacks. CRH is the component of radiative heating that would be absent if clouds were instantaneously removed from the scene (Haynes et. al., 2013). The CRH at a given atmospheric level is defined as the all-sky minus clear-sky radiative heating rate; it is the heating contribution to the atmosphere at a given level that arises from the presence of clouds anywhere in the same vertical column (Haynes et. al., 2013). Below is an equations diagram (Fig. 1.5) to calculate CRH. For example, the net SW flux is often defined as:

$$F_{net}(z) = F^{\uparrow}(z) - F^{\downarrow}(z). \qquad (1.2)$$

So the net SW flux divergence is

$$\Delta F_{net} = F_{net}(z + \Delta z) - F_{net}(z). \qquad (1.3)$$

The radiative heating rate at level z is given by

$$\left(\frac{dT}{dt}\right)_{SW} = -\frac{1}{c_p \rho}\frac{dF_{net}}{dz} = \frac{g}{c_p}\frac{dF_{net}}{dp} \qquad (1.4)$$

$$(g = 9.81,\ C_p = 1004)$$

where C_p is the specific heat capacity of air at constant pressure. The minus sign

is need because an increase in F_{net} with height implies a net loss of energy from

level z.
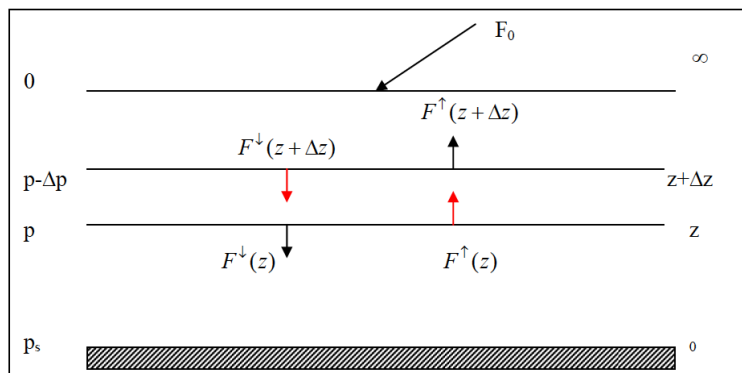
Figure 1.5 Diagram of calculating CRH.

Previously, without active sensors onboard satellites, profiles of CRH are

typically not observed directly but rather are calculated using a radiative

transfer model. Only active remote sensors, such as CloudSat and CALIPSO provide detailed information on the vertical structure of clouds necessary to calculate atmospheric radiative heating that require cloud base information. Fig. 1.6 uses CloudSat/CALIPSO data to explain where global cloud radiative heating is broken down into contributions from low-, middle-, and high-topped clouds (L'Ecuyer et al., 2008). It is shown that there is a cancellation between the cooling effects of low clouds and the heating from high-topped clouds.
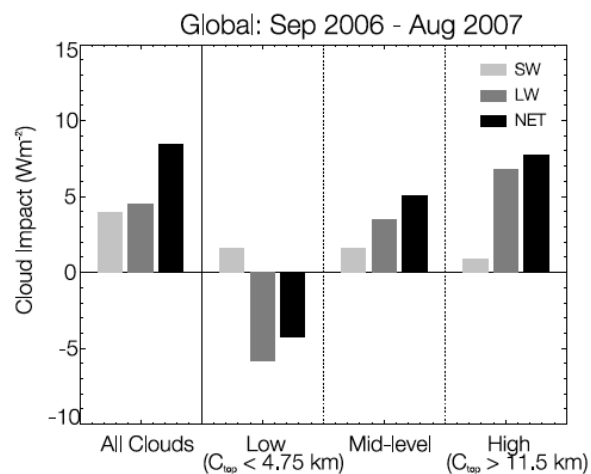
Figure 1.6 Global and annual mean cloud impacts on atmospheric radiative heating and its breakdown into high-, middle-, and low-topped cloud pixels (L'Ecuyer et al., 2008).

CRH is an important component of tropical circulation (Ramanathan et

al., 1987). In the tropics, CRH over large scales balance latent heating (Stephens, 2005) and is largely responsible for determining vertical transport through the tropical tropopause layer (Lin et al., 2013). Recently, it has been shown that cloud radiative heating enhances convections near the equator (Harrop et al., 2016).

1.5   Importance of Research

Clouds are a particularly difficult variable to constrain when quantifying the global energy budget (Trenberth et al., 2009). They play a role in almost all aspects of the system: increasing the planetary albedo by reflecting incoming solar radiation, trapping outgoing terrestrial emissions, and heating the atmosphere through latent heat processes. Each of these contributions varies widely depending on cloud microphysics, cloud location, underlying atmosphere and surface characteristics, and so forth. Clouds themselves also vary widely spatially and temporally, making them both difficult to measure and difficult to model. Despite tremendous advances in satellite technology, the details of global cloud climatology are still debated within the scientific community (Harrison et al., 1990). All of this variability leads to large uncertainties in surface fluxes, transport, and the total effect that clouds have on

them (Stephens and Greenwald, 1991).

This study addresses key issues in understanding the radiative effects of clouds in the climate system through the synthesis of active sensor and passive sensors onboard satellites. It embraces NASA's goal of using Earth system observations to improve understanding of important processes in the Earth-atmosphere system and improve climate predictability. The results of this study are expected to advance current understanding of cloud radiative effects and reduce uncertainties in representing these effects in climate models.

Clouds are an important part of Earth's general circulation (Fig. 1.7). Warm air rises at the equator producing clouds and causing instability in the atmosphere. From 30° latitude to 60° latitude exists a different circulation pattern, known as the Ferrel Cell. With converging air masses at the surface, the low surface pressure at 60° latitude causes air to rise and form clouds.
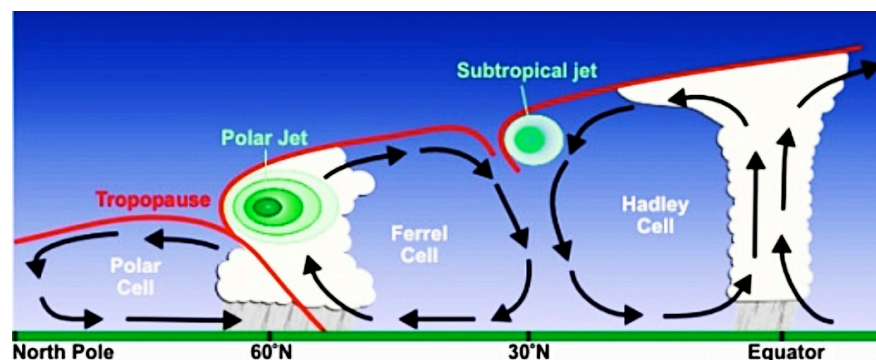
Figure 1.7 Northern Hemisphere general circulation (Schuttenhelm, 2015).

Atmospheric general circulation is expected to change as a result of increasing greenhouse gases. Greenhouse gases like carbon dioxide are perhaps more widely discussed, but clouds have similar impacts on the atmosphere. Clouds both reflect incoming sunlight and restrict the heat radiation from the surface, thereby affecting both sides of the global energy balance. Thus, any changes in clouds will modify the radiative energy balance in the climate. Furthermore, the air temperature, which is affected by clouds, in turn affects cloud formation. This circular relationship makes climate research all the more difficult. Cloud responses to changes in the climate are complex and require more focus. According to the Intergovernmental Panel on Climate Change (IPCC) Forth Assessment Report (AR4), the dominant source of spread among general circulation models' (GCM) climate sensitivities is due to diverging cloud feedbacks. IPCC Fifth Assessment Report (AR5) reports that the cloud feedback from all cloud types is +0.6 (-0.2 to +2.0) $Wm^{-2}\,°C^{-1}$.
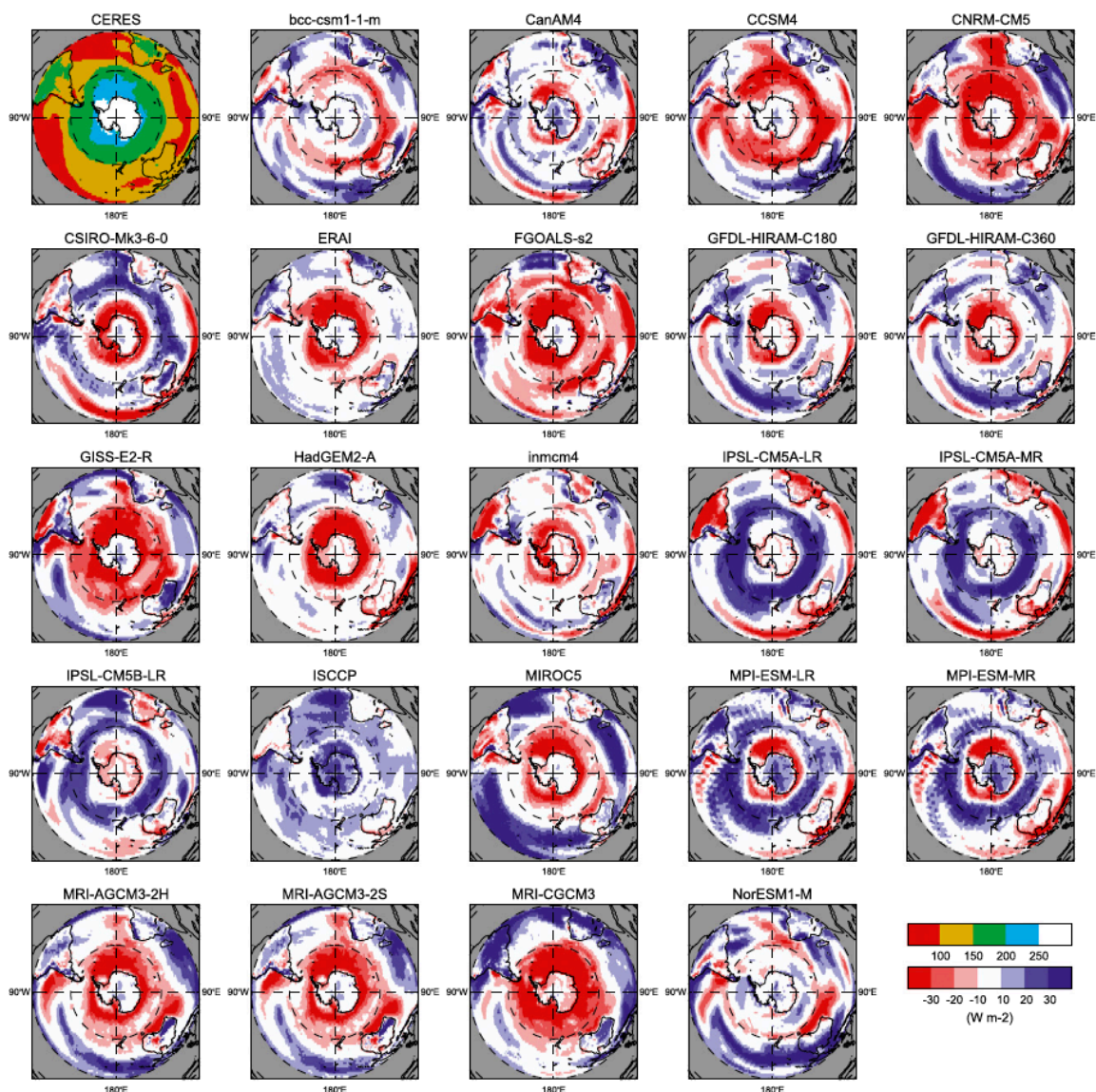
Figure 1.8 Southern Hemisphere DJF climatology for top-of-atmosphere reflected shortwave radiation. (Top left) CERES-EBAF observations. All other panels show the model biases with respect to CERES. ISCCP-FD is also shown as an additional model (Bodas-Salcedo et al., 2014).

The NCEP Climate Forecast System model shows warm sea surface

temperature biases are primarily a result of the insufficient amount of stratus clouds (Xie et al., 2006). Models generally reflect too little solar radiation over the Southern Ocean, which may be the leading cause of the prevalent sea surface temperature biases (Bodas-Salcedo et al., 2014).

Fig. 1.8 shows the December–February (DJF) reflected shortwave (SW) radiation climatology over the Southern Hemisphere (SH) from the CERES-EBAF observations (top left) and model differences from it. Out of 22 models, 16 show moderate to strong negative biases in SW south of 40$^{\text{o}}$S, 2 show a mixed pattern or small biases (BCC-CSM1.1-M and NorESM1-M), and 3 show a strong positive bias (IPSL models). This suggests that most models underestimate the top-of-atmosphere reflected SW in the Southern Ocean (Bodas-Salcedo et al., 2014). Because clouds have a leading role in controlling solar radiation's effect on the energy budget, the role of clouds on the radiation biases needs to be studied.

Clouds remain one of the largest uncertainties in the climate system's response to temperature changes. More detailed observations are needed to understand how real clouds behave. Clouds absorb and reflect solar radiation and absorb and emit thermal radiation. The resulting heating affects the atmospheric circulation and water content, which determines where clouds form. Changes in CRE in response to increased global temperatures can produce a

substantial feedback in Earth's temperature. CRE and CRH are both key components to understanding the sensitivity of climate model and making climate predictions from models more reliable (Cess et al., 1990).

Collectively, clouds have an enormous influence on Earth's energy balance, climate, and weather. Even small changes in the abundance or location of clouds could change the climate more than the anticipated changes caused by greenhouse gases, human-produced aerosols, or other factors associated with global change. Studying clouds helps scientists improve GCMs and predict Earth's future weather and climate. Satellite observations of global cloudiness used in this research will lead to the most accurate and comprehensive database of Earth's clouds ever obtained. The sensors aboard the A-Train satellite constellation offer an unprecedented dataset for assessing the climate impact of clouds. A key advantage of these measurements is the ability to detect vertical structure of clouds. Vertically resolved profiles of cloud radiative properties are achieved using a combination of active and passive sensors from the A-Train. Together, these sensors provide the accuracy and spatial coverage necessary for improving global assessments of CRE. These observations are important for improving and validating models of Earth's climate, and for seasonal and longer-term climate predictions.

Chapter 2

Previous Assessments of Cloud Fraction, Cloud Radiative Effects and Cloud Radiative Heating

Many studies have sought to characterize cloud radiative effects (CRE) and radiative heating on regional and global scales. However, global assessments have been particularly challenging since climate models have traditionally taken an overly simplified view of clouds, largely owing to a lack of high-quality, global observations of clouds and their optical properties.

2.1   Cloud Measurement Capability

2.1.1   Ground-based Networks

Scientists have been observing and monitoring clouds for decades. Ground-based observations have made important contributions to our current understanding of clouds, but don't provide cloud information at a sufficient spatial resolution necessary to improve their representation in global climate models.

The Atmospheric Radiation Measurement (ARM) program is the premier source for global, ground-based observations of atmospheric radiative fluxes. The ARM Program was created in 1989 by the U.S. Department of Energy (DOE) to develop several highly instrumented ground stations for the purpose of studying cloud formation processes and their impact on radiative fluxes. The scientific motivation for the ARM Program arose from a decade of comparison of biases among different climate models (Ackerman and Stokes, 2003). A primary objective of the program is improved scientific understanding of the fundamental physics related to radiative feedback processes in the atmosphere.

Ground-based cloud radars penetrate most optically thick clouds layers but may miss thin cirrus clouds (Comstock et al., 2002; Mace et al., 2006; Protat et al., 2006). Conversely, ground-based lidars have a greater capability to detect thin cirrus clouds, but the backscatter signals will often be extinguished by cloud layers containing supercooled liquid cloud water or cloud layers with an optical depth larger than 2–3 (e.g., Sassen and Cho 1992; Protat et al., 2006).

Clouds can also be detected by single images from an infrared camera (Shaw et al., 2005; Thurairajah and Shaw, 2005). This technique is employed by Stephen and Toumi (2008), who estimated cloud forcing directly for the first time by ground-based thermal infrared camera. A dataset of over 17,000 images was collected at the UK Meteorological Office Research Site in Cardington,

Bedfordshire, using an eastward-facing camera operating over a period of three months. Surface CRE in the 7.5–13 μm region is plotted as a function of cloud cover in Fig. 2.1. Results suggest a nonlinear relationship between cloud forcing and cloud cover, a finding that is in agreement with previous studies (Shupe and Intrieri , 2004; Dong et al., 2006; Town et al., 2007).
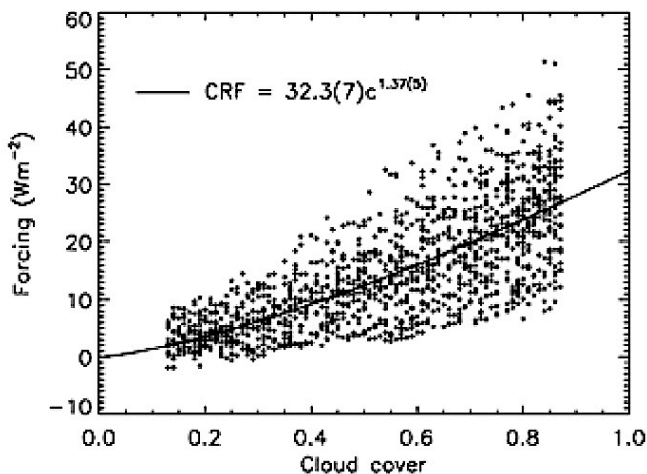
Figure 2.1 The 7.5–13 μm surface CRE as a function of cloud cover for all conditions (Stephen and Toumi, 2008).

2.1.2   Intensive Field Campaigns

Field experiments provide the opportunity to combine in situ and remotely sensed observations of physical cloud properties from a variety of measurement

platforms. Ground-based, aircraft, ship, and satellite observations are synthesized over limited spatial and temporal domains to study cloud processes in extensive detail. Field campaigns are typically conducted downwind of known continental cloud source regions, such as North America, East Asia, and North Africa. Intensive measurements coupled with model simulations allow field experiments to vastly improve physical and microphysical understanding of regional cloud in the atmosphere over time periods ranging from weeks to months.

2.1.3 Satellite Remote Sensing

Several satellite missions provide unprecedented Earth observing capabilities that allow for global observations of the planet. In the 1970's, the National Aeronautics and Space Administration (NASA) recognized the importance of understanding Earth radiation budget and its effects on the climate. Earth Radiation Budget Satellites (ERBS) was first launched in 1984 to make accurate regional and global measurements of the components of the radiation budget. Then two satellite instruments NOAA 9 and NOAA 10 were launched jointly in 1984 and 1986, which constitute the Earth Radiation Budget Experiment (ERBE).

The International Satellite Cloud Climatology Project (ISCCP) was established in 1982 as part of the World Climate Research Program (WCRP) to collect weather satellite radiance measurements. Since then, visible and infrared imagery from an international network of weather satellites have been routinely processed to produce a global cloud climatology to infer information about the distribution of clouds, their properties, and diurnal, seasonal and interannual variability (Rossow et al., 1991). In the ISCCP dataset, cloud types are categorized by their top height and optical thickness (Chen et al., 1999).

The Clouds and Earth's Radiant Energy System (CERES) instrument, developed by NASA, was launched in 1997 onboard the Tropical Rainfall Measuring Mission (TRMM) satellite. CERES satellite instruments provide highly accurate radiance estimates globally at 20-km spatial resolution (Loeb et al., 2005). CERES supplies radiometric measurements at various levels of the atmosphere from three broadband channels for top of atmosphere (TOA) and surface LW, SW and net fluxes under clear and all sky conditions (Rose and Rutan, 2013). These estimates are derived by applying empirical angular distribution models from high-resolution imager based cloud retrievals.

The Moderate Resolution Imaging Spectroradiometer (MODIS) is one of satellites aboard the Terra Earth Observing System (EOS) platform launched in December 1999 (Platnick et al., 2003). MODIS provides an extensive cloud

mask: cloud-top properties like temperature, pressure, effective emissivity; cloud thermodynamic phase; cloud optical; microphysical parameters like optical thickness, effective particle radius and water path. A true-color composite image of the MODIS granule is shown in Fig. 2.2. The image shows extensive marine stratocumulus boundary layer clouds off the coasts of Peru and Chile.

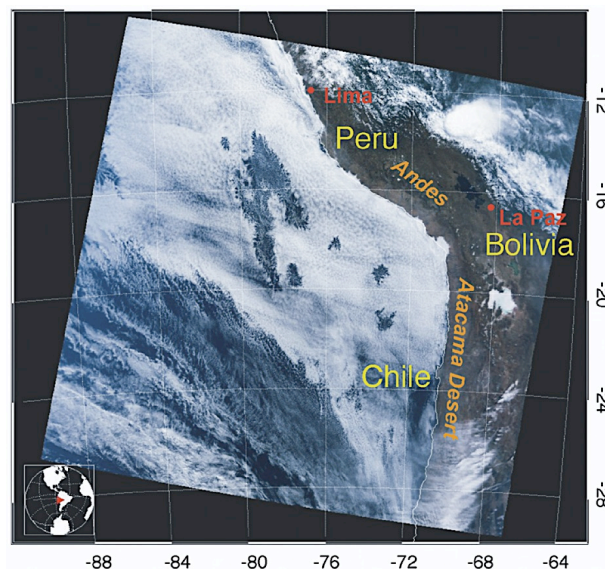**Figure 2.2 True-color composite of a granule of Terra MODIS data from July 18, 2001, 1530 UTC. The image shows widespread boundary layer stratocumulus clouds off the coasts of Peru and Chile, associated with cool upwelling water along the Humboldt current (Platnick et al., 2003).**

Launched in 2006, CloudSat is a sun-synchronous, polar orbiting satellite that is part of the A-Train constellation. The satellites fly at an equatorial

altitude of approximately 705 km with an inclination of 98.2^{o} (L'Ecuyer and Jiang 2010). CloudSat is in tight formation with the Cloud Aerosol Lidar and Infrared Pathfinder Satellite Observation (CALIPSO) satellite, which combines active radar and lidar sensors to obtain the internal structure of cloud and aerosol layers (Winker et al., 2003). CloudSat's 2B-FLXHR-LIDAR dataset, which combines data from CloudSat and CALIPSO, is used to estimate the downwelling LW and SW flux profiles at the surface and TOA. Henderson et al. (2013) combined vertical cloud information from CloudSat and CALIPSO with MODIS data to assess the impacts of clouds on the top-of-atmosphere (TOA) and surface radiative fluxes to improve errors relative to CloudSat-only products. It is suggested that uncertainties in SW fluxes are dominated by uncertainties in CloudSat liquid water content estimates and the sources of LW flux uncertainty are surface temperature and lower-tropospheric humidity (Henderson et al., 2013).

2.2   Measurement-based Estimates

Ground-based estimates provide accurate measurements of cloud properties at fixed locations over extended periods of time. Wang and Sassen (2001) used ground-based remote sensors to identify cloud type and microphysical

properties. The study illustrates how extended-time remote sensing datasets can be converted to cloud properties of concern to climate research (Wang and Sassen, 2001).
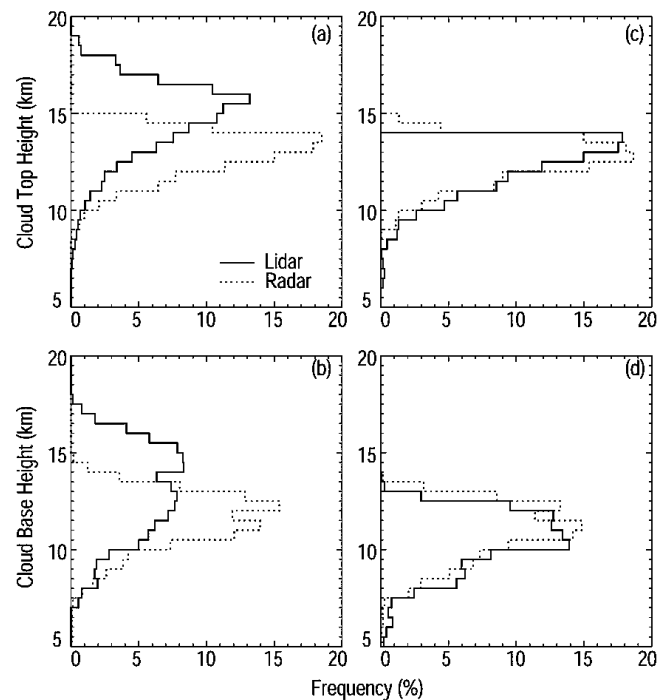
Figure 2.3 Frequency of occurrence (%) of cloud bases and top heights detected by radar and lidar between April and November 1999. (a) and (b) are for all retrievals. (c) and (d) are for coincident radar and lidar observations (Comstock and Ackerman, 2002).

Comstock and Ackerman (2002) used ARM eight months of cirrus ground-based observations to demonstrate that the millimeter cloud radar fails to detect 13% of cirrus clouds with a cloud base higher than 15 km. Fig. 2.3 is the cloud fraction (CF) observed by lidar and radar between April and

November 1999. It is shown that lidar detects significantly higher cloud tops while radar misses 45% of cloud tops height above 15 km. Moreover, new estimates of CRE and CRH for specific cirrus clouds cases suggest that the radiative impact of tropical cirrus clouds is larger than previously thought.

While ground-based measurements make significant contributions, particularly in regards to the temporal variability of clouds, they are largely limited to areas over land. Satellite observations complement and extend the ground-based observations by providing increased spatial coverage and multiple observational capabilities.

Ramanathan (1987) used the ERBE dataset to evaluate the role of Earth's radiation budget in climate and general circulation. It is shown that the LW effect of clouds enhances the meridional heating gradient in the troposphere, while the albedo or SW effect of clouds largely reduces the available solar energy at the surface (Ramannthan, 1987). Harrison et al. (1988) first estimated the diurnal variation of LW radiation from ERBE, and used monthly averaged clear-sky and cloudy sky flux data derived from the ERBE to assess the impact of clouds on the Earth' s radiation balance and concluded that clouds appear to cool the Earth-atmosphere system (Harrison et al., 1990)

Ockert-Bell and Hartmann (1992) compared the cloud information

between ISCCP and ERBE dataset. The 35 possible ISCCP cloud types (Rossow and Schiffer, 1991) were regrouped into 5 groups. Clouds were divided into high, middle, and low according to cloud top pressure, and thin and thick according to their optical depth. It was found that total cloud fraction is a relative poor predictor of radiation budget quantities. However, if the regions only have one main cloud type, the predictions become better. They also asserted that the total fractional area covered by clouds needs to be divided into contributions from different cloud types. Thus, the fractional coverage by cloud types together forms a more accurate prediction of radiation budget quantities (Ockert-Bell and Hartmann, 1992).

Hartmann et al. (1992) took this analysis a step further and compared cloud forcing estimated using the ISCCP-ERBE regression with that derived from the ERBE scene identification. Their results show good agreement except over snow, tropical convective regions, and regions that are either nearly clear sky or always cloudy with multilayered clouds. The June-July-August (JJA) and DJF seasonal averages for the one-year period from March 1985 to February 1986 show that a substantial fraction of the disagreement appears in tropical convective regions. Hartmann at al. (1992) point out that the reason might be

that the ERBE scene identification does not take into account variations in upper-tropospheric water vapor.

Hartmann et al. (1992) further concluded that, of the five cloud categories described above, low clouds make the largest contribution to the net energy balance of the Earth. Low clouds have the strongest net cloud forcing, especially in the summer hemisphere. This is because low clouds cover a large area of Earth and their albedo effects dominate their impacts on emitted thermal radiation. However, high thin clouds make a positive contribution, about 5 W m^{-2} in the zonal average, to the net radiation in the tropics.

Rossow et al. (1993) compared ISCCP by surface observations over an eight-year period. The ISCCP cloud occurrence statistics appear too low over land by about 10% (Rossow et al., 1993). Zhang et al. (1995) calculated surface and TOA radiative fluxes from physical quantities based on ISCCP datasets. It is suggested that clouds are the most important modulator of the SW fluxes; however, over land the uncertainties in net SW fluxes at the surface depend almost as much on uncertainties in surface albedo (Zhang et al., 1995). Chen et al. (1999) investigated radiative flux changes induced by the occurrence of different cloud types from ISCCP cloud data. Cloud-type variations are shown to be as important as cloud cover in modifying the radiation field of the Earth

atmosphere system. Other variables, such as the solar insolation and atmospheric and surface properties, also play significant roles in determining regional cloud radiative effects (Chen et al., 1999).

Li et al. (2004) examined the spatial distributions and seasonal variations of total cloudiness and fractional cloud amount of high, middle and low clouds over China by using ISCCP satellite data and World Meteorological Organization (WMO) surface synoptic observations. It was found that low clouds occur most frequently along the southeast coast of China, middle clouds dominated southern China, and high clouds mainly occurred over northern China (Li et al., 2004). Town et al. (2006) compared cloud cover over the South Pole from visual observations, satellite retrievals, and surface-based infrared radiation measurements. Their analysis concluded that the best surface-based source of cloud cover in terms of the combination of accuracy and length of record is determined to be surface-based broadband IR data. Haynes et al. (2007) used early results from CloudSat to detect tropical oceanic cloudiness and the incidence of precipitation. Kotarba (2008) compared MODIS-derived cloud amount with visual surface observations. It was found that MODIS observed 4.38% greater cloud amount in summer conditions and 7.28% in winter conditions. Furthermore, differences were greater at nighttime than during daytime.

As reproduced from IPCC AR5, Fig. 2.4 (Mace et al., 2009) illustrates the annual mean cloud fraction from the Cloud Profiling Radar (CPR) on CloudSat and the Cloud–Aerosol Lidar with Orthogonal Polarization (CALIOP) onboard CALIPSO, showing that clouds cover roughly two thirds of the globe. According to Fig. 2.5, high clouds occur most frequently near the equator and tropics, middle clouds are prominent in the Intertropical Convergence Zone (ITCZ), low clouds always occur in cool subtropical oceans and in polar regions.
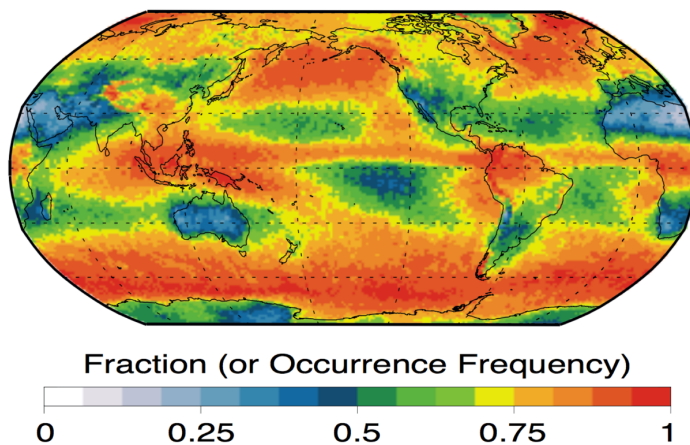
Figure 2.4 Annual mean cloud fraction (CloudSat/CALIPSO 2B GEOPROF-LIDAR data set for 2006–2011) (Mace et al., 2009).
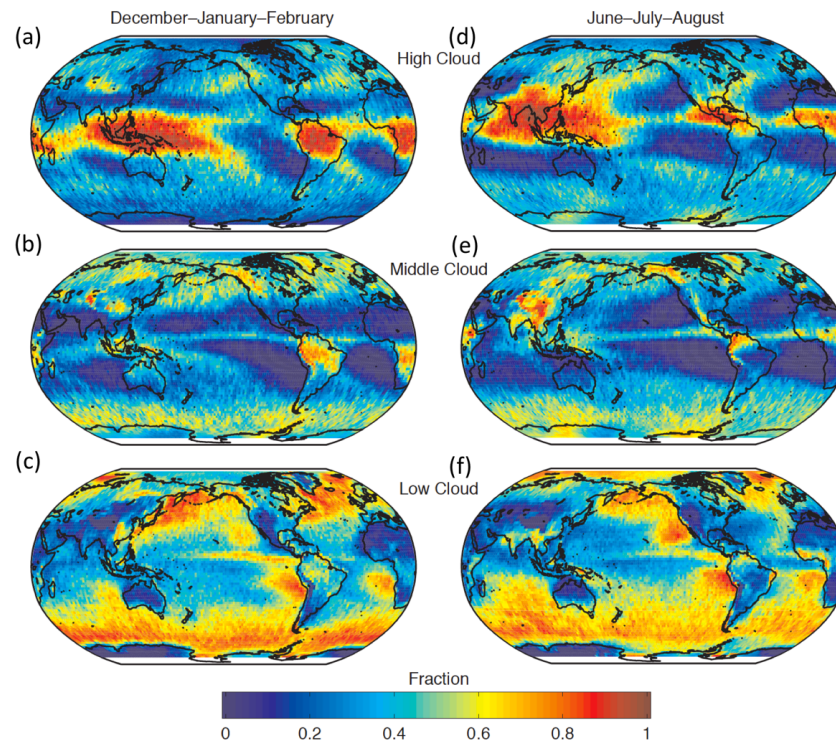
Figure 2.5 (a–c) DJF mean high, middle and low CF from CloudSat/CALIPSO 2B-GEOPROF R04 and 2B-GEOPROF-LIDAR P1. R04 datasets for 2006–2011, (d–f) same as (a–c), except for JJA (Mace et al., 2009).

Protat et al. (2009) evaluated CloudSat and CALIPSO tropical ice clouds using ground-based cloud radar and lidar observations from the ARM site in Darwin, Australia. Results show that all satellite methods produce ice water contents and extinctions in a much narrower range than the ground-based method and overestimate the mean vertical profiles of microphysical parameters below a height of 10 km.

Fig. 2.6 shows annual-mean TOA CRE from CERES. The global mean SW CRE is -47.3 W m^{-2}, LW CRE is 26.2 W m^{-2}, and net CRE is -21.1 W m^{-2}. High clouds dominate patterns of LW CRE while SW CRE is sensitive to thick clouds at all latitudes. SW CRE also depends on solar insolation, and therefore, is sensitive to the diurnal and seasonal cycles of cloudiness. In Fig. 2.6c, the net CRE is negative over most of the globe, especially in regions of stratus and stratocumulus clouds such as the mid-latitude and eastern subtropical oceans, where SW CRE is strong but LW CRE is weak.
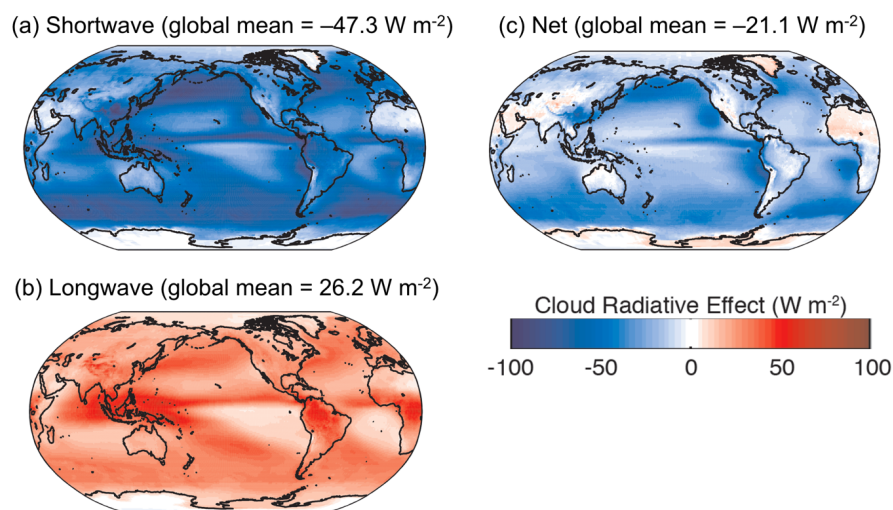
2.6 Distribution of annual-mean TOA CRE: (a) SW, (b) LW, (c) net, during 2001–2011 from CERES (Loeb et al., 2009).

Haynes et al. (2011) quantified the organization and structure of Southern

Hemisphere (SH) mid-latitude clouds by combining measurements from ISCCP and CALIPSO datasets and found that ISCCP overestimates midlevel cloudiness. Henderson et al. (2013) used combined data products 2B-FLXHR-LIDAR from CloudSat, CALIPSO, and MODIS to estimate the radiative impacts of clouds, and compared with CERES estimates, which is more consistent with past modeling studies than with observational estimates that were based on passive sensors. Haynes et al. (2013) used CloudSat and CALIPSO datasets to examine radiative heating features in the atmosphere between 2006 and 2010. It is found that there is a minimum in cooling in the tropical lower to middle troposphere, and clouds tops tend to strongly cool the upper boundary layer all year in the mid- to high-latitudes of the SH (Haynes et al., 2013). Protat et al. (2013) tested ground-based estimates of CF and CRH around Darwin, Australia and found that a ground-based radar-lidar combination does not detect most of the cirrus clouds above 10 km. The reason is likely attributed to a limitation of lidar detection capability and signal obscuration by low-level clouds (Protat et al., 2013).

Liu et al. (2013) compared cloud properties from the whole-sky infrared cloud-measuring system (WSIRCMS) and measurements of visual observations and a ceilometer during the period July–August 2010 at the

Chinese Meteorological Administration Yangjiang Station, Guangdong Province, China. The WSIRCMS is a ground-based passive sensor installed on the rooftop of the Yangjiang observing station. WSIRCMS provides a way to obtain cloud distribution, calculate cloud amount, and estimate cloud-base height, and to classify cloud types every 15 min with no difference in sensitivity during day and night. While Cu and Ci clouds are classified with high accuracy, Sc and Ac clouds are not (Liu et al., 2013).
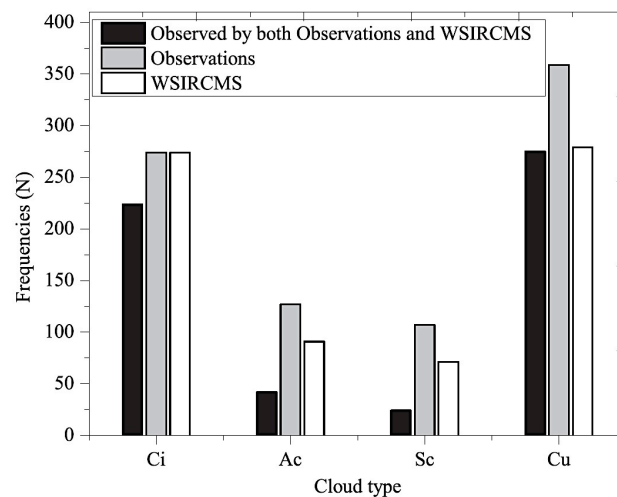

Figure 2.7 Frequency distribution of the cloud types from WSIRCMS and visual observations during JJA 2010 at Yangjiang Station (Liu et al., 2013).

The occurrences of detected cloud type from WSIRCMS and visual observations datasets are shown in Fig. 2.7. It indicates that the frequencies in each cloud type detected by WSIRCMS are smaller than those from visual

observations. In addition, Cu and Ci clouds derived from WSIRCMS show good agreement with visual observation data, while Ac and Sc clouds do not. Cloud type with a small CF can be easily detected by human eyes, while it is difficult for instruments (Liu et al., 2013).

Johansson et al. (2015) studied the vertical structure of cloud radiative heating over the Indian subcontinent during summer monsoon using CloudSat and CALIPSO datasets. It is suggested that contrasting CRE in the atmosphere and at surface, and during active and break periods have direct implications for the monsoonal circulation (Johansson et al., 2015).

Using all of these observations, the role that clouds play in global climate is better understood. In this study, CloudSat and CALIPSO datasets will be used to measure cloud radiative effects in Earth's energy balance.

2.3   Model-based Estimates

Representing clouds parameters in climate model is challenging, which affects modeled climate sensitivity. It is critical that models accurately assess cloud forcing if used to predict future climate. The simulation of clouds in modern climate models is a combined estimation of turbulence, cumulus clouds convection, microphysical process, radiative transfer and cloud fraction. The system of parameterizations must balance simplicity, realism, computational

stability and efficiency (IPCC AR5).

Recent researches make advances in parameterizing CRE. Some models have improved representation of sub-grid scale cloud variability, which has important effects on grid-mean radiative fluxes and precipitation fluxes, for example, based on the use of probability density functions of thermodynamic variables (Sommeria and Deardorff, 1977; Watanabe et al., 2009). Stochastic approaches for radiative transfer can account for this variability in a computationally efficient way (Barker et al., 2008).

Parameterizing clouds in climate models is challenging due to microphysical processes of ice- and mixed-phase clouds are poorly understood. GCMs overestimate multi-layered clouds, especially over high-latitude continents and subtropical oceans (Naud et al., 2008; Mace et al., 2009).

New treatments of cloud overlap have been motivated by new observations. Previously, we only have horizontal scale of cloud amount and ignore the vertical overlap between different grid levels. New observations from active sensors on CloudSat and CALIPSO have led to revised treatments of overlap in some models, which significantly affects CRE (Pincus et al., 2006; Shonk et al., 2012). Active sensors have also been useful in detecting low-lying Arctic clouds over sea ice (Kay et al., 2008), improving our ability to test climate model simulations of the interaction between sea ice loss and cloud

cover (Kay et al., 2011).

The fifth phase of the Coupled Model Intercomparison Project (CMIP5) is an international group of climate model experiments used for the IPCC AR5 report in order to provide a framework of integrated climate change experiments using coupled models. Each model in CMIP5 has its own limitations depending on its modeling parameters.

Su et al. find that the cloud parameterization errors contribute to the total errors for all climate models. The errors are closely associated with large-scale temperature and moisture structures. All models capture deep and shallow clouds well, although failing to capture the vertical structures of high and low clouds. CALIPSO simulator CF generally agrees better with CloudSat/CALIPSO combined retrieval than the model CF, especially in the mid-troposphere (Su et al., 2013).

Calisto et al. (2014) compared radiative fluxes for 10 years from 11 models participating in the CMIP5 and from CERES satellite observations. The global mean seasonal CRE is averaged over 10 years for the CMIP5 models as well as for CERES satellite data is given in Table 2.1. The majority of the investigated CMIP5 models show a tendency towards a too-negative global mean net CRE as compared to CERES (Calisto et al., 2014). Several other papers, including Zhang et al. (2005) and Klein et al. (2013), have also shown

that models may not have a CRE that fits well with the satellite data.

Model	LWCRF DJF [W m^{-2}]	LWCRF JJA [W m^{-2}]	SWCRF DJF [W m^{-2}]	SWCRF JJA [W m^{-2}]	NetCRF DJF [W m^{-2}]	NetCRF JJA [W m^{-2}]
ACCESS1-0	24.4	25.7	−47.7	−43.6	−23.3	−17.9
bcc-csm1	26.3	27.9	−58.5	−52.1	−32.2	−24.2
CanESM2	24.7	25.9	−52.6	−44.9	−27.9	−19
CCSM4	25.1	26.4	−50.9	−45.8	−25.8	−19.4
GFDL	23.2	24.6	−51.8	−48.3	−28.6	−23.7
HadCM3	20.7	21.9	−53.9	−49.8	−33.2	−27.9
inmcm4	20.4	21.3	−45.7	−38.1	−25.3	−16.8
IPSL-CM5A-LR	30.7	30.9	−58.1	−45.1	−27.4	−14.2
MIROC5	25.2	26.9	−58.2	−51.7	−33	−24.8
MPI-ESM-P	23.6	25.9	−53.5	−48.9	−29.9	−23
Nor-ESM1-ME	28.9	30.7	−59.4	−51.9	−30.5	−21.2
CERES (satellite)	25.9	27	−52.4	−44.8	−26.5	−17.8

Table 2.1 Global mean LW CRE, SW CRE, and Net CRE for DJF and JJA for several CMIP5 models as well as for CERES satellite data averaged over 10 years (Calisto et al., 2014).

2.4   Reducing Uncertainties in Estimates

Estimates of cloud fraction from visual observations are poor because of optically thin clouds and inadequate moonlight at nighttime (Hahn et al., 1995). It is difficult to determine CF from satellite data over the poles because of the small contrast in both albedo and temperature between the snow surface and clouds (Rossow and Schiffer, 1999).

Cloud vertical profile remained poorly resolved brings uncertainties in estimates due to multilayered clouds and ambiguity in cloud base. CloudSat's cloud profiling radar has been operating since 2006 (Stephens et al., 2008) and the largest uncertainties in cloud detection are related to the inability of the CPR to resolve low clouds within the radar's ground clutter region below 1 km. But high, thin clouds were also identified as uncertainty. After 2012, above limitations been overcome in the new CloudSat 2B-FLXHR-LIDAR, which combines data from CloudSat, CALIPSO and lidar-based aerosol retrievals. CALIPSO focused on profiling aerosols and thin clouds with lidar, and CloudSat profiling thicker clouds using radar (L'Ecuyer et al., 2010).

Overall, most previous observational assessments of CF and CRE have been based on retrievals from passive satellite sensors. Cloud vertical structures should be considered more than before. Due to the limitation of instruments, cloud feedback is considered as a single type of parameter before, which ignores the difference among different cloud types. In climate models, CRE should be considered separately based on cloud thickness, height and shape.

2.5   Remaining Questions

Most assessments of CRE from passive satellite observations have instrument

limitations, which inhibit current global estimates of the cloud radiative effects. It is critically essential that clouds are adequately represented in assessments of global cloud radiative effects. Evaluating CRE over land and in cloudy skies requires characterization of the vertical cloud distributions. This has proved challenging for both models and observations due to the large errors introduced by incorrect assumptions of three-dimensional cloud fields. The lack of cloud observations over cloudy-sky conditions ultimately hinders global assessments of cloud radiative effects. High-quality measurements of cloud properties in poorly sampled regions are necessary to reduce uncertainties in current global estimates of CRE.

2.6   Science Questions and Objectives of This Research

This thesis describes recent efforts to address these questions using data from CloudSat's multi-sensor radiative fluxes and heating rates product (FLXHR-LIDAR), which leverages high-resolution vertical cloud information from CloudSat and CALIPSO. The cloud fraction and cloud radiative effects from nine cloud types are evaluated by comparing with previous maps of ISCCP cloud fraction and CERES forcing. Three specific cloud classes will be highlighted in greater detail, including cirrus, stratocumulus, and deep

convection clouds to contrast their different implications for climate feedbacks. In addition, cloud types will be regrouped in order to compare the results more directly with classical cloud classifications based on passive sensors.

Chapter 3

Data and Methodology

3.1   The Afternoon Constellation

The Afternoon Constellation (A-Train) consists of six Earth-observing satellites operated by NASA and its international partners flying along the same orbit "track". As shown in Fig. 3.1, these six satellites are Aura, CloudSat, CALIPSO, Aqua, GCOM-W1 (Global Change Observation Mission-Water), and OCO-2 (Orbiting Carbon Observatory). All of these satellites cross the equator northbound at about 1:30 p.m. local time which allows near-simultaneous observations of clouds, aerosols, atmospheric chemistry, and other elements critical to understand Earth's changing climate.
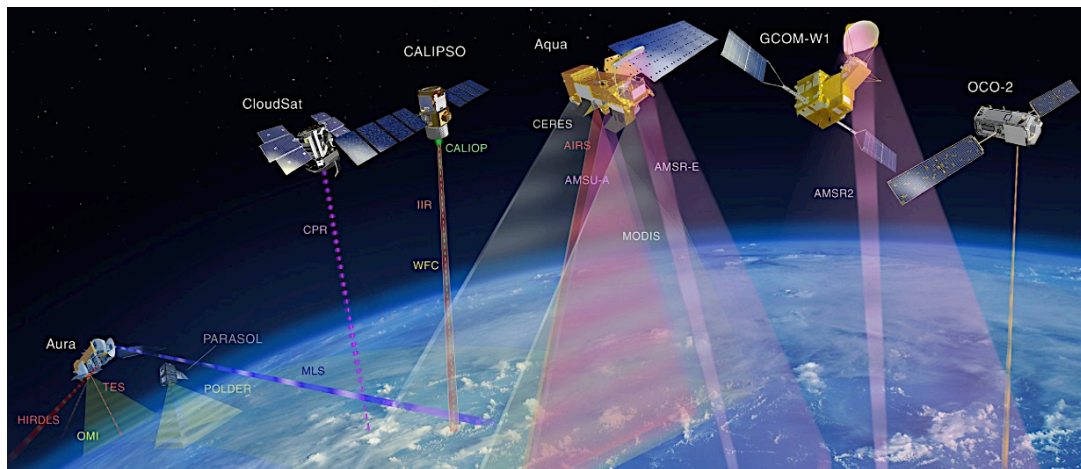
Figure 3.1 The A-Train Constellation.

3.1.1   CloudSat

CloudSat is a part of A-Train constellation launched by NASA on April 28, 2006, providing much needed measurements of the vertical structure of clouds from space (Stephens et al., 2002). The only sensor aboard CloudSat is the CPR. CPR is a 94-GHz nadir-looking radar that provides cloud measurements at a 500 m vertical resolution and a 1.5 km horizontal resolution (Im et al., 2005). Because clouds weakly scatter microwave radiation, CPR's -28 dBZ detection sensitivity enables the first global view of the vertical structure of atmospheric clouds. The major components of the radar hardware are shown in Fig. 3.2 (Stephens et al., 2008). Both the 94 GHz Extended Interaction Klystron (EIK)

contributed by the Canadian Space Agency and the 20 kV power supply on CloudSat are the first of their kind being flown in space.
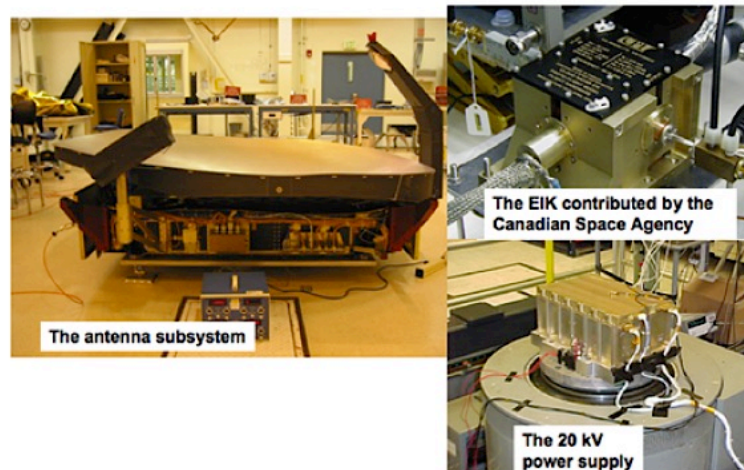

Figure 3.2 Photographs of three important components of the CPR. The extended interaction klystron and high voltage power supply integrate to form the High Power Amplifier subsystem (Stephens et al., 2008).

Fig. 3.3 presents the historic first-look CPR image of the vertical structure of a warm front over the North Atlantic observed on 20 May 2006 (Stephens et al., 2008). The top figure is a MODIS image of a warm frontal system intersected by CloudSat along the orbit track highlighted. The bottom figure is the first quick-look image of Cloudsat's CPR reflectivity over an approximate 1400 km section of orbit on 20 May 2006. The bottom figure clearly shows the clouds' vertical structures.
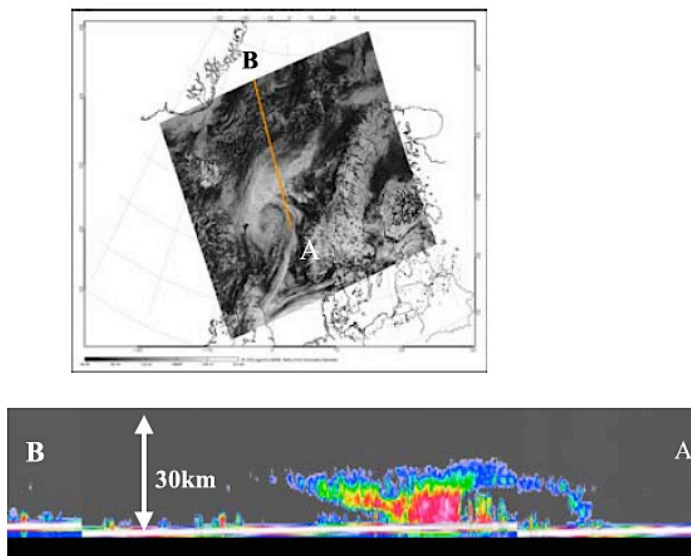
Figure 3.3 (Top) A MODIS image of a warm frontal system intersected by CloudSat along the orbit track highlighted. (Bottom) The very first quick-look image of Cloudsat CPR reflectivity gathered for an approximate 1400 km section of orbit on 20 May 2006, captured immediately after powering on the CPR (Stephens et al., 2008).

3.1.2   CALIPSO

The CALIPSO satellite was launched on April 28, 2006 along with the CloudSat satellite. CALIPSO combines active and passive sensors together to provide new insight into the vertical structure and properties of thin clouds and aerosols in the atmosphere. In particular, cloud observations from the CALIPSO lidar and the CloudSat radar will be complementary, together

encompassing the variety of clouds found in the atmosphere, from thin cirrus to deep convective clouds (Winker et al., 2004).

CALIOP is a spaceborne two-wavelength polarization lidar carried by the CALIPSO satellite, which provides high resolution vertical profiles of clouds and aerosols and has been designed with a very large linear dynamic range to encompass the full range of signal returns from aerosols and clouds (Winker et al., 2007). CALIOP is the first spaceborne lidar optimized for aerosol and cloud measurements and is also the first polarization lidar in space. Lidars take direct measurements and provide the most detailed and accurate information on cloud and aerosol height. With sufficient averaging, CALIOP is also able to detect and characterize weak aerosol layers and thin clouds with optical depths of 0.01 or less (McGill et al., 2007). Fig. 3.4 shows a nighttime transect from northern Europe southward across Africa into the Atlantic Ocean west of South Africa (Winker et al., 2007). The three panels show lidar return signals from the three CALIOP channels. Shown are (top) total 532 nm return, (middle) 532 nm perpendicular return, and (bottom) total 1064 nm return. Strong returns from clouds and from the surface appear in gray scale. Yellows and reds represent weak cloud and strong aerosol scattering, and greens and blues represent molecular scattering and scattering from weak aerosol and cloud layers.
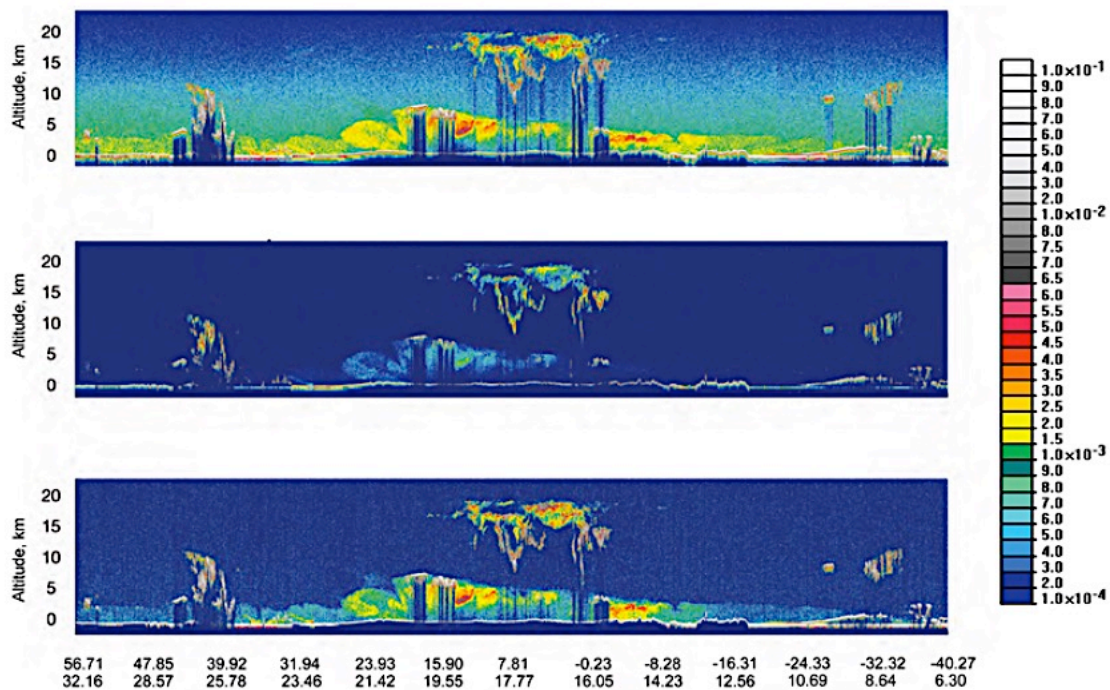
Figure 3.4 CALIOP observations on June 9, 2006, acquired along an orbit track from northern Europe across Africa into the south Atlantic (Winker et al., 2007).

3.2 CloudSat's 2B-CLDCLASS-LIDAR Data Product

CloudSat supports a 94 GHz CPR as part of the innovative A-train formation of satellites studying the Earth's clouds and atmosphere. Using vertical profiles of clouds and precipitation, 2B-CLDCLASS-LIDAR is a product developed to determine the type of clouds present (Sassen et al., 2008). 2B-CLDCLASS-LIDAR provides 8 classes of cloud type, including precipitation identification

and likelihood of mixed phase conditions (Stephens et al., 2008). 2B-CLDCLASS-LIDAR combines measurements from CloudSat, CALIPSO and other ancillary data to classify clouds into different types. As shown in Fig. 3.5, according to cloud features like height, temperature, phase and cloud thickness, clouds are sorted to eight types: St, Sc, Cu (including Cu congestus), Ns, Ac, As, D.C, and high (Ci and cirrostratus) clouds. Compared with the previous radar-only 2B-CLDCLASS product, this dataset incorporates CALIPSO lidar information for improved detection of thin clouds, more precise cloud boundaries, and information about cloud phase in each cloud layer. The current version of the 2B-CLDCLASS-LIDAR data product is the 2B-CLDCLASS-LIDAR P_R04, which is a four-year dataset covering the period from 2007 to 2010.
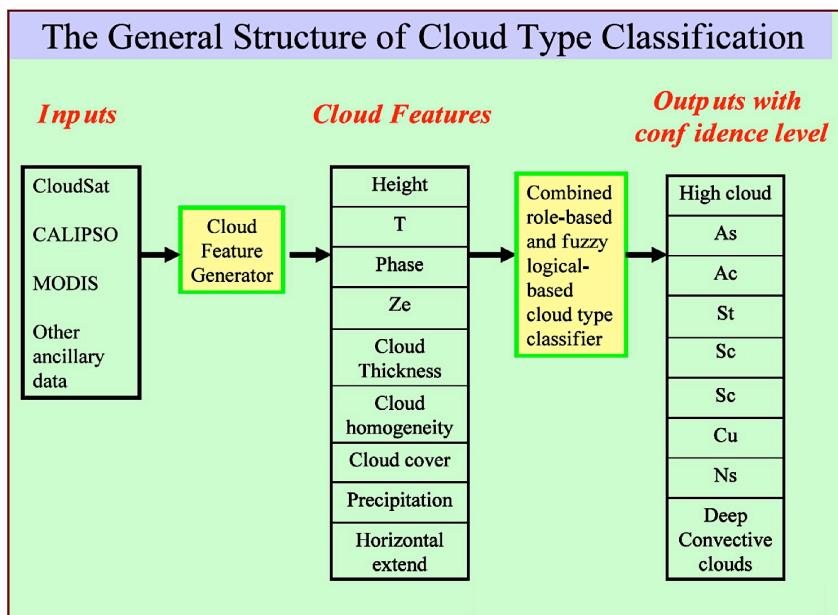
The General Structure of Cloud Type Classification

Inputs	Cloud Features	Outputs with confidence level
CloudSat / CALIPSO / MODIS / Other ancillary data	Cloud Feature Generator → Height, T, Phase, Ze, Cloud Thickness, Cloud homogeneity, Cloud cover, Precipitation, Horizontal extend	Combined role-based and fuzzy logical-based cloud type classifier → High cloud, As, Ac, St, Sc, Sc, Cu, Ns, Deep Convective clouds

Figure 3.5 The general function blocks of the classification algorithm.

3.3   CloudSat's 2B-FLXHR-LIDAR Data Product

CloudSat's 2B-FLXHR-LIDAR data product provides observationally constrained radiative transfer calculations of broadband radiative fluxes and heating rates (Henderson et al., 2013). The underlying goal of the 2B-FLXHR-LIDAR algorithm is to produce a vertically resolved radiative flux and heating rate data set that is consistent with observed reflectivities from CloudSat's CPR (L'Ecuyer et al., 2008). This product combines data from CPR, CALIPSO, and MODIS to estimate broadband fluxes and radiative heating rates consistent with liquid and ice water content in the atmosphere. Fig. 3.6 presents the process of the 2B-FLXHR-LIDAR data product. The blue ovals represent inputs including profiles of cloud ice and liquid water content and cloud particle effective radii from the CloudSat level-2B algorithms, as well as gas extinction and temperature profiles from the European Centre for Medium-Range Weather Forecasts (ECMWF) analyses. Properties of thin and low clouds are based on CALIPSO data and surface albedo, solar zenith angle, etc. from ancillary datasets. The product's output includes vertical profiles of upwelling and

downwelling LW and SW fluxes at CPR resolution and profiles of atmospheric radiative heating. The version of 2B-FLXHR-LIDAR used in this work is P2_R04.
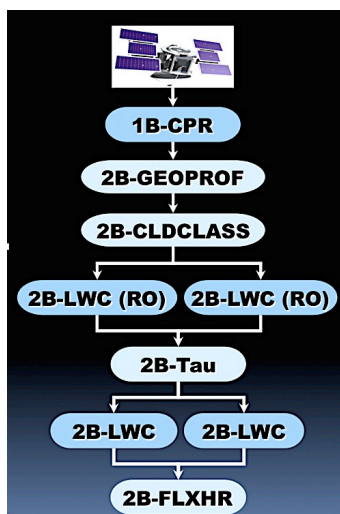

Figure 3.6 Diagram of producing 2B-FLXHR-LIDAR data product.

Several key elements of the 2B-FLXHR-LIDAR algorithm, its inputs, and its primary outputs are summarized for a half granule data (NH) from 1 June 2007 in Fig. 3.7. Calibrated reflectivity observations from the CPR are shown in Fig. 3.7a followed by the 2B-GEOPROF cloud mask product and the corresponding LW downwelling and SW upwelling fluxes. Corresponding heating rates are presented in Fig. 3.7f - h.
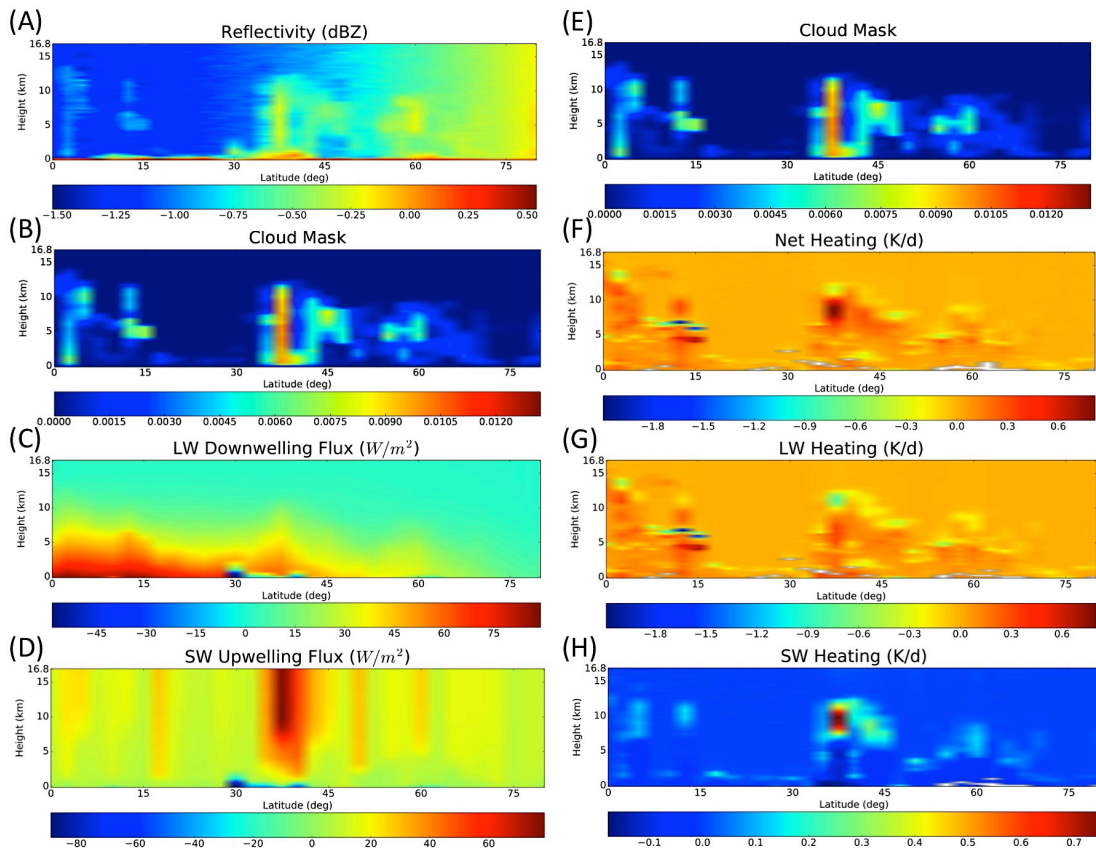
Figure 3.7 Inputs and outputs from the CloudSat 2B-FLXHR-LIDAR algorithm. (A) reflectivity, (B) cloud mask, (C) LW downwelling flux, (D) SW upwelling flux, (E) cloud mask (repeated), (F) net heating, (G) LW heating, (H) SW heating (in K d⁻¹).

3.4   Methodology

The 2B-FLXHR-lidar dataset is comprised of 285 x 10^6 radiative flux profile from 82.5° S to 82.5° N. In this study, all the monthly data collected between January 2007 and December 2010 (Seasonal data are JJA/DJF between

December 2006 and August 2010) are gridded to 2.5° × 2.5°. Incomplete and missing input data are removed to control the data quality. The variables used from the dataset are the all-sky and the clear-sky upward and downward fluxes. The method of computing CRE using these fluxes was described in chapter 1. Fig. 3.8 provides a sample of SW, LW, and net CRE at the TOA and SFC using the same granule data as was used in Fig. 3.7. Comparing the Fig. 3.7b cloud mask with Fig. 3.8, higher CF appears between 30°- 45° N, where the SW CRE is stronger than at other latitudes which results in a cooling effect in the atmosphere. In Fig. 3.8, both SW CRE and LW CRE varies at the TOA and SFC, which reveals that CloudSat/CALIPSO can provide radiative information at SFC, unlike previous projects like ERBE that could only detect TOA fluxes.
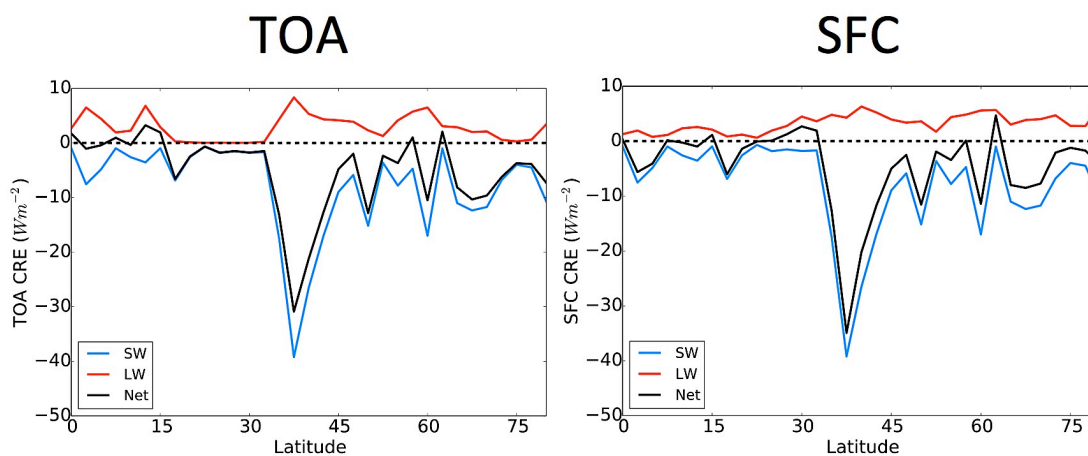

Figure 3.8 Sample data of zonal SW, LW, and net CRE at TOA and SFC.

Fig. 3.9 shows a global map of one granule of data of SW CRE from 1 June 2007. Blue dots represent strong SW forcing and red dots represent weak SW forcing. The North Pacific Ocean looks cloudy and has a strong SW forcing. Fig. 3.10 shows the corresponding vertical SW CRH in Fig. 3.9. High clouds are abundant at 45° N and 20° S in this granule data.
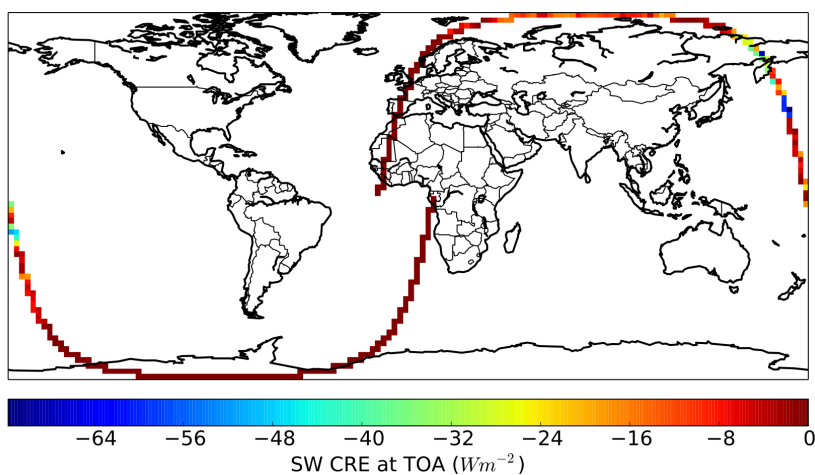

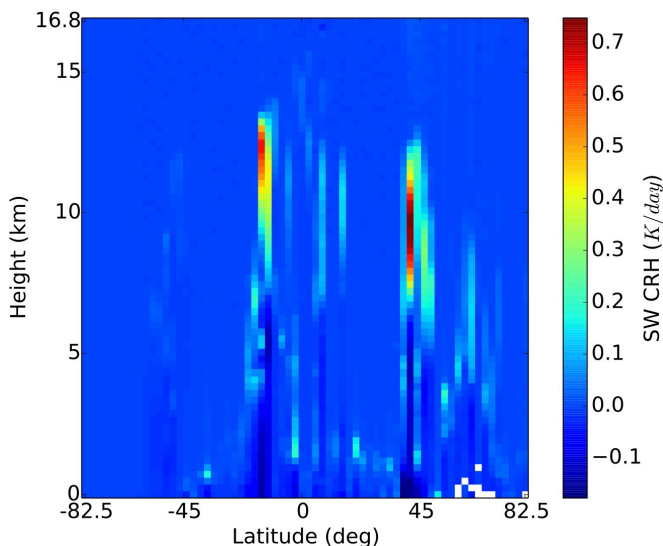**Figure 3.9 Sample data of global SW CRE at TOA.**

Figure 3.10 Sample data of vertical SW CRH.

In this study, CF, CRH, and CRH are sorted by nine cloud types. Eight of these cloud types are defined in the 2B-CLDCLASS-LIDAR dataset, and an additional cloud type is introduced here: the *multilayered cloud* that includes all pixels that contain more than one cloud layer. SW fluxes appear only during the day and the length of daytime varies dramatically with the seasons. To correct for the SW diurnal cycle, all of the SW fluxes are normalized by 12-month averages of the SW fluxes. In other words, the SW downward TOA flux is collected from FLXHR-LIDAR and binned at 2.5° resolution for annual averages and monthly averages; then each monthly map is divided by its global average. This represents the fraction of incoming solar radiation by the global mean. Finally, all global SW fluxes are compared to the normalization to

account for the fact that higher latitudes receive less sunlight on average than the tropics. The effects of three common cloud classes will be highlighted in detail: Ci, Sc, and D.C. clouds, in order to contrast their dramatically different effects on climate. In addition, cloud types will be regrouped in order to compare the results with classical cloud classifications based on passive sensors including those from the ISCCP and ERBE archives. For quality control, profiles that include bad or missing input data are removed from the dataset. The criteria are described in more detail in Table 14 of the CloudSat FLXHR-LIDAR Data Product Documentation (Henderson and L'Ecuyer, 2011).

Chapter 4

Global Observations

4.1   Global Distribution of Cloud Fraction

Cloud fraction, also referred to as cloud frequency of occurrence, is defined as the number of cloudy pixels divided by the total number of pixels observed (NASA Privacy Policy and Important Notices, 2011). Fig. 4.1 shows global mean CF averaged over January 1984 to December 1999 (Probst et al., 2012). The blue line shows the total cloud fraction from D2 ISCCP observations and the red bars show the total cloud fraction for each the 21 models participating in the 3rd Climate Model Intercomparison Project (CMIP3). Overall, the models do a poor job at estimating global CF and large differences exist among models. Of the 21 models, twenty underestimate the observed CF while only the CNRM-CM3 model overestimates compared to the ISCCP observations. Fig. 4.2 shows the CF zonal means from ISCCP observations and the 21 CMIP3 models. All models show good agreement with ISCCP at mid latitudes, while some are

biased low in the tropics. However, most models disagree with ISCCP observations in the polar regions, and large differences also exist among different CMIP3 models. It is evident that CF needs to be studied in greater detail to explore their roles in the global energy budget and thus reduce cloud biases in climate models.
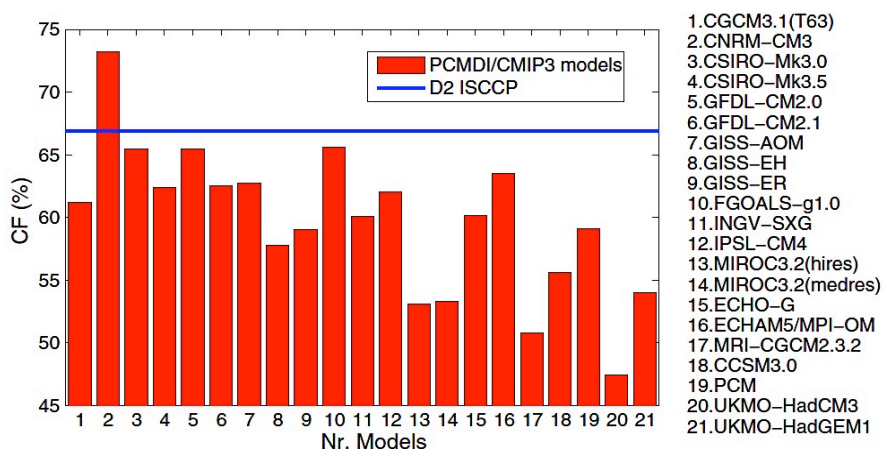

Figure 4.1 Global mean CF averaged over Jan 1984–Dec 1999 (Probst et al., 2012).
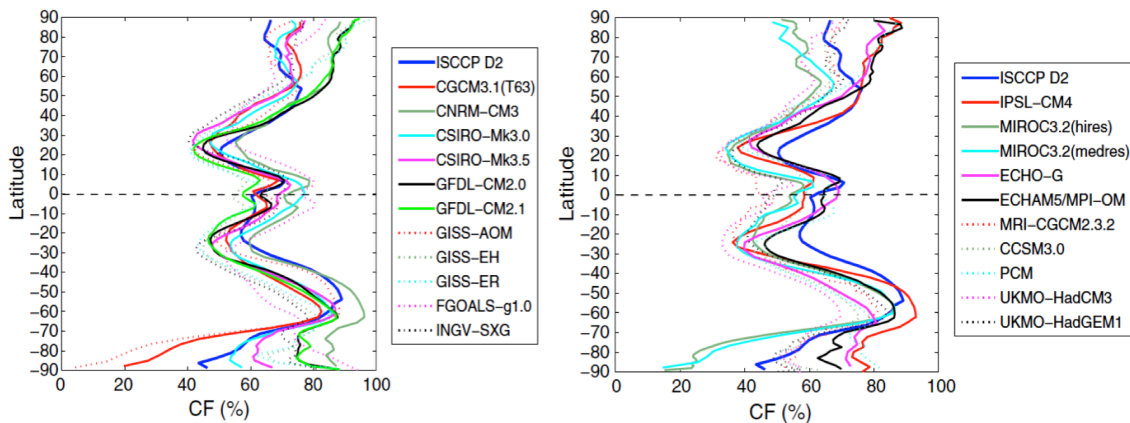
Figure 4.2 CF zonal means of ISCCP and of PCMDI-CMIP3 models (Probst et al., 2012).

Fig. 4.3 presents the total CF observed from CloudSat/CALIPSO for 2007-2010. Satellite observations show that clouds occur most frequently near the equator and poles, while continents tend to be less cloudy than adjacent oceans. In the Western Hemisphere (WH), CF is greater than 70% over the Intertropical Convergence Zone (ITCZ), where easterly trade winds in the Northern and Southern Hemispheres converge. While clouds are considerably less frequent in the subtropics, at latitudes poleward of 60° CF over ocean exceeds 80% due to the presence of storm tracks. In the Eastern Hemisphere (EH), high CF is observed in the Southern Ocean, North Indian Ocean, Tropical Western Pacific, and Western China. Conversely, CF is less than 30% over desert regions in Australia, Egypt, and Saudi Arabia.
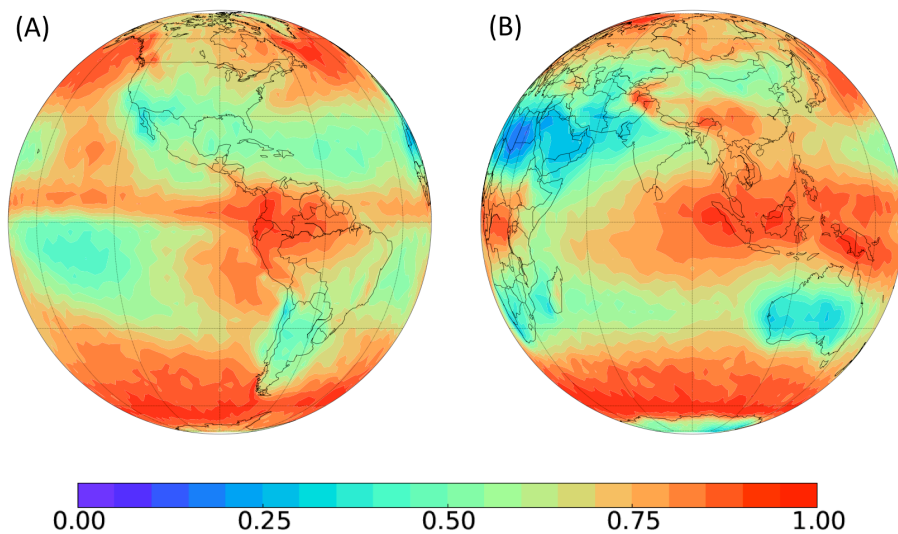
Figure 4.3 Total CF from CloudSat/CALIPSO 2B-FLXHR-LIDAR dataset for 2007-2010.

However, total cloud fraction is a poor predictor of cloud radiative forcing, which can be better represented by regional CF dominated by clouds of a single radiative type (Ockert-Bell et al., 1992). In this study, total CF is separated into nine individual cloud types, as shown in Fig. 4.4 and Fig. 4.5.
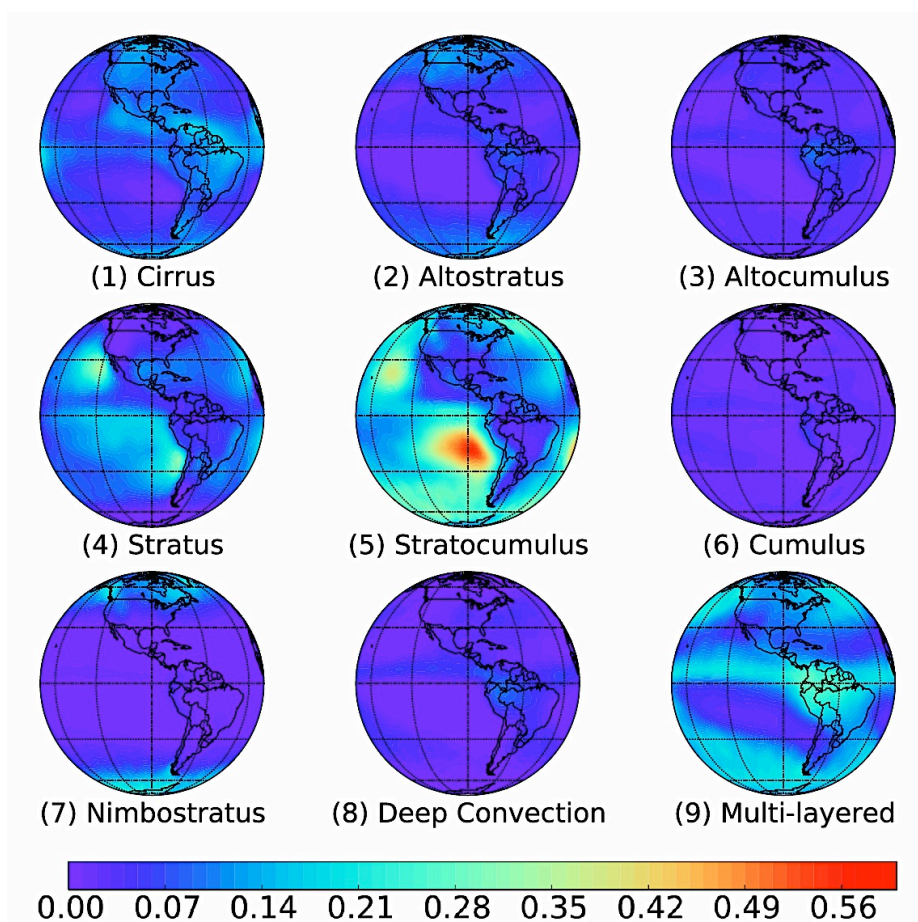
Figure 4.4 WH individual CF from CloudSat/CALIPSO 2B- FLXHR-LIDAR dataset for 2007-2010.
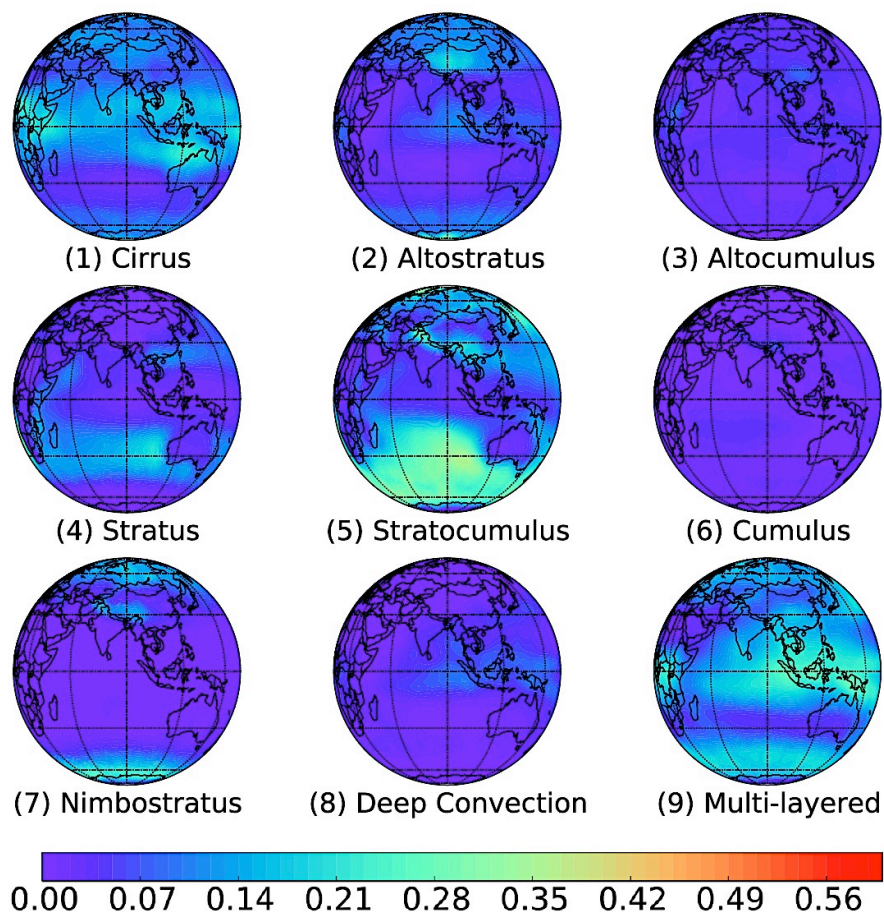
Figure 4.5 EH Individual CF from CloudSat/CALIPSO 2B-FLXHR-LIDAR dataset for 2007-2010.

A comparison between Fig. 4.3 and Fig. 4.4/4.5 shows that each cloud type has a unique spatial pattern of cloud fraction. Ci and D.C. clouds are common at the ITCZ due to large transport of water vapor into the upper levels by the persistent convection. At high latitudes, CF is high for As and Ns clouds while low for Cu clouds. St and Sc clouds are most frequent over the eastern

basins of subtropical ocean due to subsidence from the downward branches of the Hadley and Walker circulations. Equatorial regions of South America, western Africa, Indonesia and the western Pacific Ocean are locations where M.L. clouds are most common.

4.2   Implications for Cloud Radiative Effects

Fig. 4.6a shows the annual mean total cloud fraction from ISCCP while Fig. 4.6b highlights the mean annual net cloud radiative effect from CERES. Although the time periods covered in these figures differ, results show that CF alone does not directly explain observed CRE. Over western Northern America, for example, CF is relatively high (60%) even though the CRE is nearly zero. Over the South Pacific Ocean (red circle), however, CF is also 60% but the CRE is considerably stronger at -40 W m^{-2}. It is concluded, therefore, that total CF is not a good indicator of cloud forcing. Not only CF but also CRE needs to be classified into different cloud types. Total CF from CloudSat/CALIPSO and net CRE at TOA from 2B-FLXHR-LIDAR are displayed in Fig. 4.7. Compared to passive retrievals from ISCCP, CloudSat/CALIPSO observes a greater frequency of clouds over polar regions. Over the ITCZ, FLXHR-LIDAR estimates of CRE are stronger than estimates from CERES.
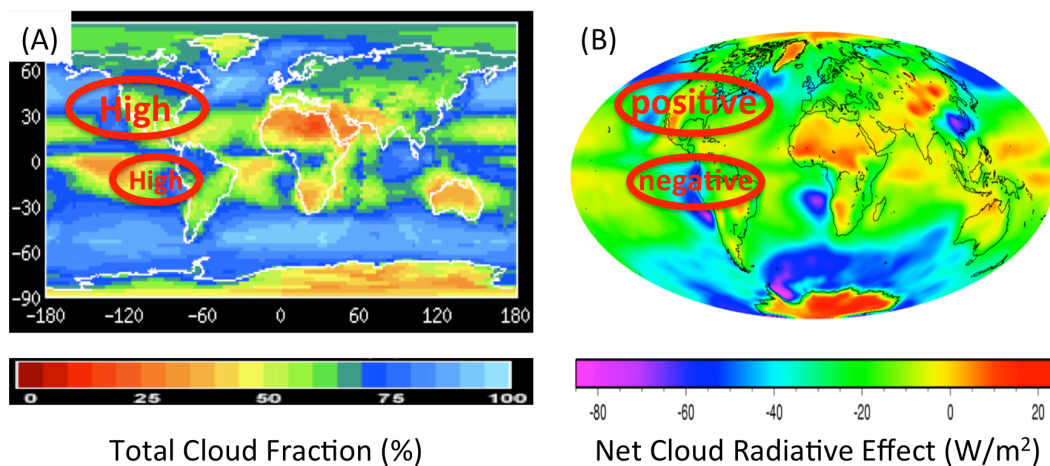
Figure 4.6 (A) ISCCP mean annual CF, Jul. 1983 – Dec. 2009, (B) CERES mean annual net CRE at TOA, Mar. 2000 – Feb. 2001 (UCAR, 2016 and Cambridge University, 2007).
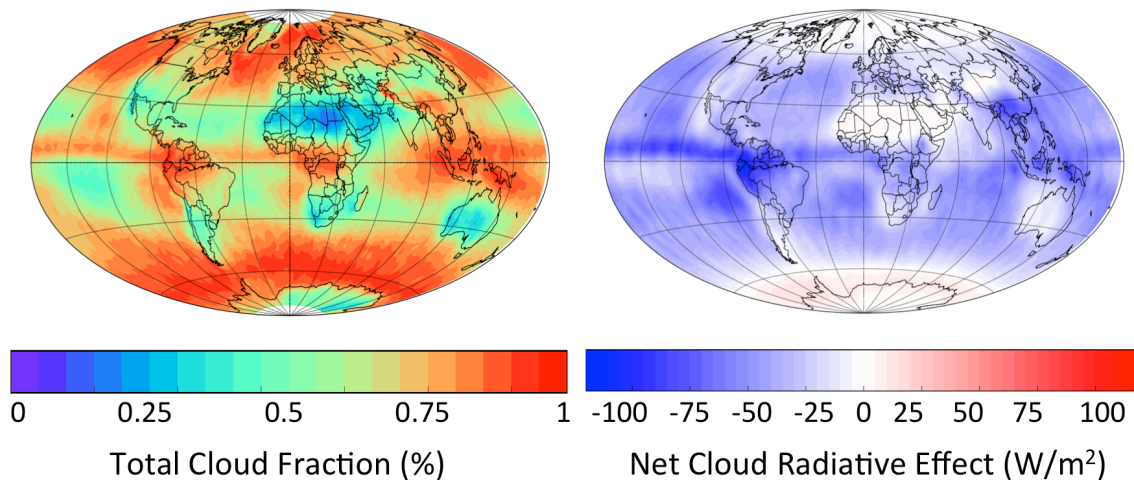
Figure 4.7 CloudSat/CALIPSO mean annual CF and net CRE at TOA.

Ockhart-Bell and Hartmann (1992) introduced four simplified cloud-type models in Fig. 4.8, with cloud types grouped according to pressure and optical depth. These include a three cloud-type model (high, middle, and low clouds), a five cloud-type model, and a seven cloud-type model by Rossow and Schiffer (1991). The one-type description is a regression on total cloud cover.

Figure 4.8 Four cloud-type models (Ockert-Bell and Hartmann, 1992).

Table 4.1 shows the corresponding fraction of explained variance of net CRE at TOA by multiple regressions on ISCCP cloud data over six regions (Ockert-Bell and Hartmann, 1992). Most regions show a significant increase in

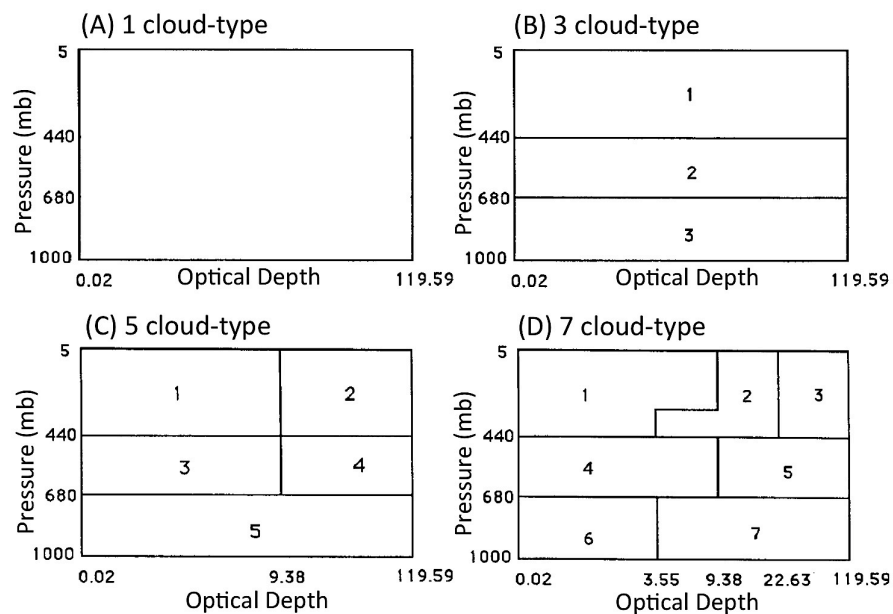the explained variance of net CRE when the fractional area coverage of cloudiness is divided into contributions from different cloud types. This indicates cloud-type information is as important as total CF in the radiation budget. If the total CF is separated by the contributions from different cloud types, the CRE of individual cloud types will have a more robust prediction of radiative impact. A limitation of this approach toward classifying clouds is that passive sensors don't provide enough information about cloud vertical structure.

Region name	Latitude range	Longitude range	Cloud type
TCL (land)	0°–5°S	62.5°–70°W	convective
TCO (ocean)	5°–10°N	142.5°–150°E	convective
STO (ocean)	12.5°–17.5°S	80°–87.5°W	stratus
MSL (land)	35°–40°N	82.5°–90°W	synoptic
MSO (ocean)	32.5°–37.5°N	40°–47°W	synoptic
HiLat (land)	60°–65°N	60°–67.5°E	synoptic

(six region)

Net radiation (R_{net})	TCL	TCO	STO	MSL	MSO	HiLat
April 1985						
7 cloud-type	0.55	0.52	0.35	0.43	0.66	0.41
5 cloud-type	0.56	0.50	0.32	0.42	0.57	0.33
3 cloud-type	0.13	0.23	0.32	0.30	0.22	0.27
1 cloud-type	0.11	0.08	0.19	0.27	0.16	0.22
July 1985						
7 cloud-type	0.40	0.64	0.57	0.41	0.62	0.77
5 cloud-type	0.39	0.61	0.56	0.43	0.47	0.73
3 cloud-type	0.29	0.26	0.49	0.26	0.17	0.63
1 cloud-type	0.13	0.14	0.37	0.22	0.07	0.60
October 1985						
7 cloud-type	0.54	0.58	0.67	0.50	0.22	0.11
5 cloud-type	0.52	0.60	0.60	0.50	0.21	0.12
3 cloud-type	0.31	0.32	0.59	0.36	0.15	0.04
1 cloud-type	0.07	0.15	0.54	0.25	0.10	NS*
January 1986						
7 cloud-type	0.30	0.29	0.53	0.45	0.54	
5 cloud-type	0.29	0.29	0.48	0.37	0.53	
3 cloud-type	0.09	0.06	0.42	0.18	0.29	
1 cloud-type	0.06	0.06	0.36	NS*	NS*	

Table 4.1 Fraction of explained variance of net CRE at TOA by multiple regressions on ISCCP cloud data in six regions. The cloud-type descriptions are shown in Fig. 4.8 (Ockert-Bell and Hartmann, 1992).

4.2.1   Cirrus Cloud Radiative Effect

Based on CloudSat/CALIPSO-based observations of total CF and TOA CRE shown in Fig. 4.7, this study explores the role of individual cloud types on the global energy budget. Since cirrus is high and optically thin, this type of cloud primarily transmits incoming solar radiation but traps outgoing infrared radiation emitted by the Earth, thereby inducing a warming effect. Fig. 4.9 presents the average LW and SW CRE when Ci is observed (CRE_{Ci}), which shows that the characteristics of Ci clouds change regionally. High values of CRE_{Ci} signify that the Ci clouds are deeper and the cloud top temperature has a larger contrast relative to the surface temperature. Areas where the effects are weaker (e.g. Tibetan plateau, polar regions, and over the Rocky mountains) are indicative of either shallower Ci or colder underlying surfaces. Comparing SW and LW effects, results show that LW CRE_{Ci} has a larger effect on climate. The net radiative effect of Ci clouds ($< CRE_{Ci} >$) can be obtained by multiplying the

conditional mean values (CRE_{Ci}) shown in Fig. 4.9 by the fractional occurrence

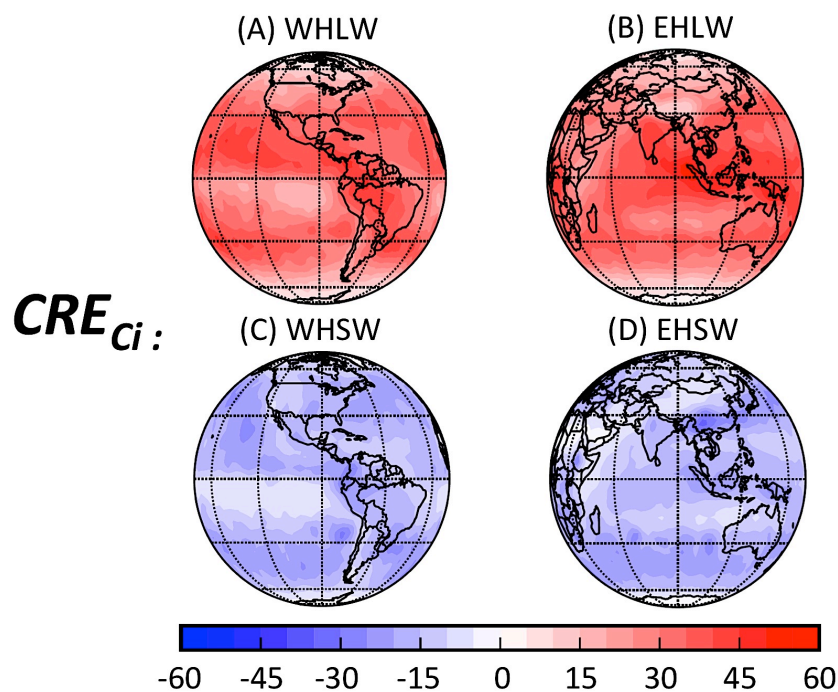of Ci clouds (CF_{Ci}) in Fig. 4.4/4.5. The results are shown in Fig. 4.10.

Figure 4.9 Average LW and SW CRE (W m^{-2}) when CloudSat and CALIPSO observe Ci (CRE$_{Ci}$). (A) WH LW CRE$_{Ci}$ (B) EH LW CRE$_{Ci}$ (C) WH SW CRE$_{Ci}$ (D) EH SW CRE$_{Ci}$.
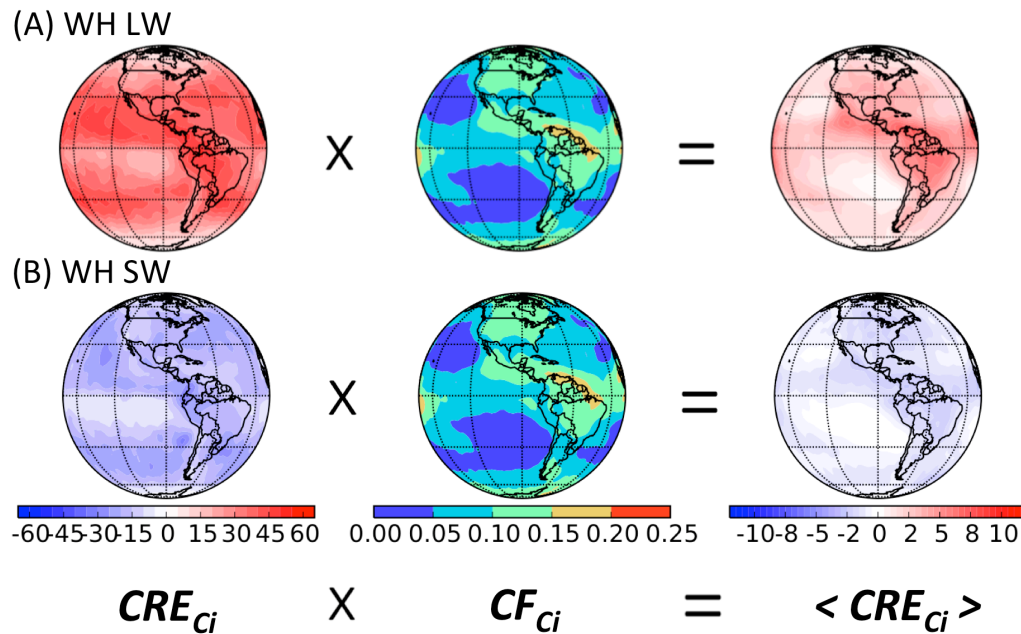
Figure 4.10 WH LW, SW < CRE$_{Ci}$ > (W m^{-2}). CRE$_{Ci}$ is the total CRE when Ci is observed, CF$_{Ci}$ is Ci cloud fraction, < CRE$_{Ci}$ > is the contribution of CRE from Ci only.

In Fig. 4.10, CRE$_{Ci}$ is realively weak and the maximum is only around 60 W m^{-2}. Ci reaches a maximum CF of 0.2 near the northeast coast of South America. After multiplying < CRE$_{Ci}$ > by CF, results show much more variability. This suggests that variability in the spatial distribution of cirrus plays a bigger role in determining their effects on the climate than variability in Ci microphysical structure (i.e. the figure on the far right < CRE$_{Ci}$ > matches the CF better than the CRE$_{Ci}$ on the left). In the WH, LW < CRE$_{Ci}$ > is around 6 W m^{-2}, and the maximum area is Tropical West Pacific. SW < CRE$_{Ci}$ > is much

weaker, only around -2 W m^{-2} globally thus Ci has a warming effect due to its higher LW radiation and its relatively high CF.

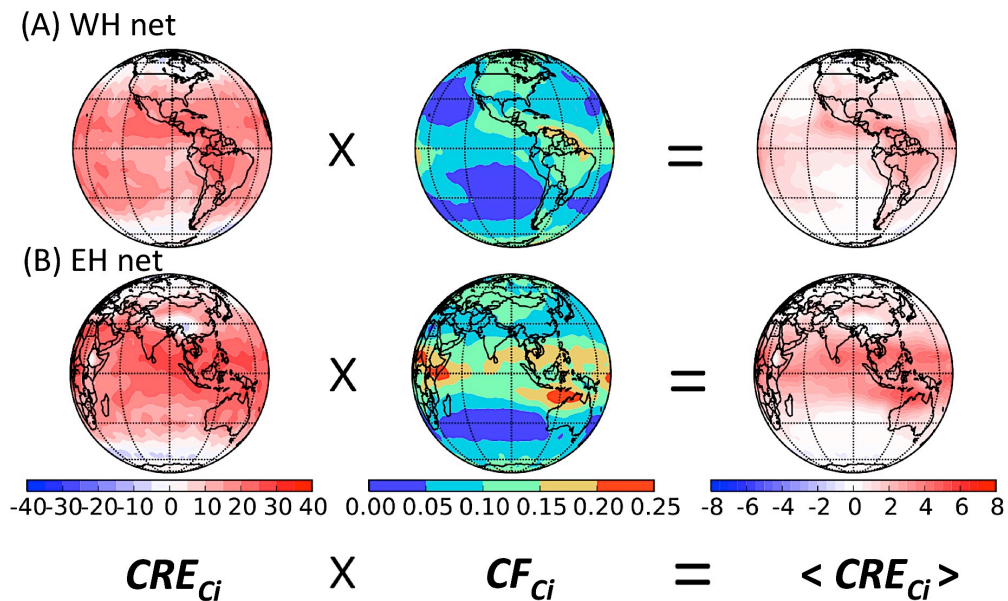(A) WH net

(B) EH net

-40 -30 -20 -10 0 10 20 30 40   0.00 0.05 0.10 0.15 0.20 0.25   -8 -6 -4 -2 0 2 4 6 8

CRE_{Ci} X CF_{Ci} = $<CRE_{Ci}>$

Figure 4.11 WH and EH net < CRE$_{Ci}$ > (W m^{-2}).

Fig. 4.11 displays the net < CRE$_{Ci}$ > in the WH and EH. CRE$_{Ci}$ tends to produce larger effect in the EH (30 W m^{-2}) than the WH. CF$_{Ci}$ is also higher in the EH with a maximum of nearly 0.25 over the West Indian Ocean and western Australia. Cirrus clouds exert a net warming effect in both hemispheres, but especially in the mid latitudes where the radiative effect reaches 7 W m^{-2}.

4.2.2   Stratocumulus Cloud Radiative Effect

Compared to cirrus, stratocumulus (Sc) clouds are lower and thicker, and have opposite radiative effects. Fig. 4.12 presents SW and LW CRE_{Sc} in each hemisphere. In Fig. 4.9, the same color bar was adopted for SW and LW CRE_{Ci} due to their similar magnitudes, but for Sc cloud different scales are needed due to the much higher SW radiative forcing. Conditional mean LW cloud forcing from Sc, CRE_{Sc} is very constant globally with values 30 W m^{-2} except over the west coast of North and South America where weaker values are observed, consistent with the high lower tropospheric stability in these regions. SW effects, which are more variable and much larger in both hemispheres, are ten times as strong as the LW effect. The maximum SW effects (-350 W m^{-2}) occur over the Brazilian Amazon Basin, which might be influenced by smoke aerosol particles that have been found to suppress the formation of tropical D.C. clouds (Andreae et al., 2004).
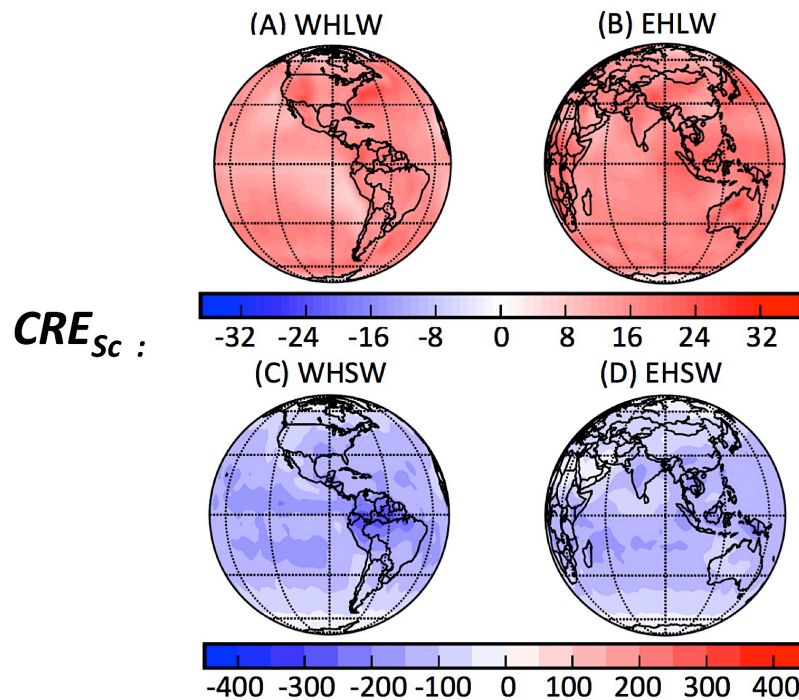
(A) WHLW (B) EHLW

CRE_{Sc} :

-32 -24 -16 -8 0 8 16 24 32

(C) WHSW (D) EHSW

-400 -300 -200 -100 0 100 200 300 400

Figure 4.12 WH and EH LW, SW CRE$_{Sc}$ (W m^{-2}).

Fig. 4.13 is the same as Fig. 4.10, but for Sc cloud. Compared to cirrus, stratocumulus clouds have weaker LW effects but stronger SW effects. Sc clouds dominate the Southeast Pacific Ocean, where annual mean CF exceeds 50%. Over this region, Sc clouds exert a significant cooling effect with a SW < CRE$_{Sc}$ > of -100 W m^{-2}.
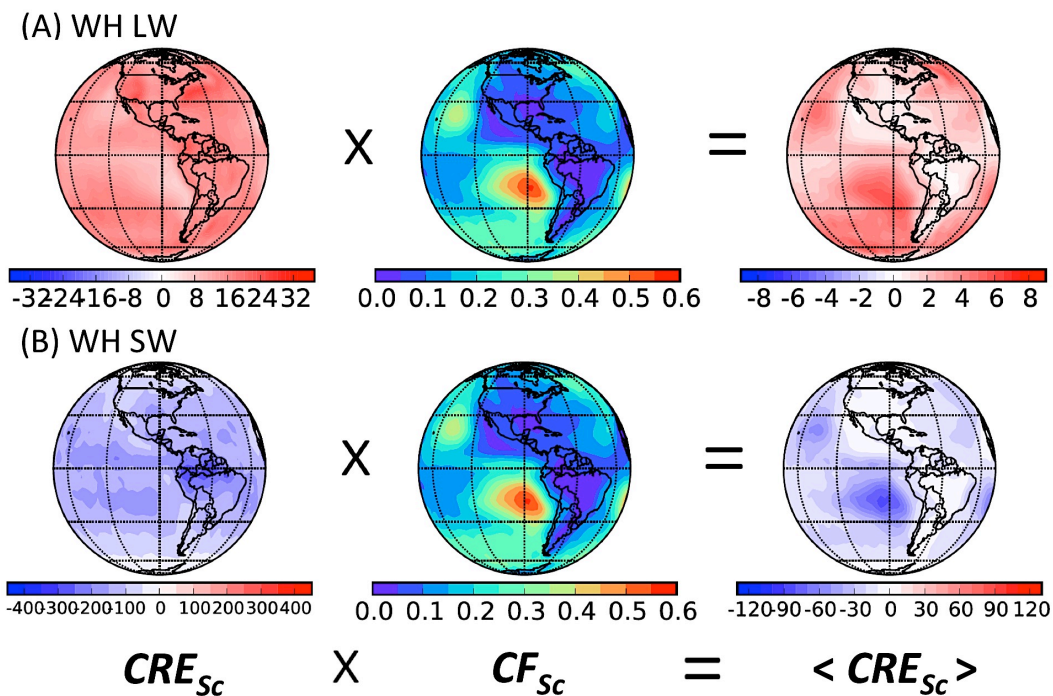
Figure 4.13 WH LW and SW < CRE$_{Sc}$ > (W m^{-2}).

Fig. 4.14 is the same as Fig. 4.11, but for Sc cloud. Sc cloud has a higher CF in SH than NH. While Ci clouds warm the planet, this effect is more than compensated by the strong cooling from Sc clouds that reaches a maximum of -110 W m^{-2} in Southeast Pacific Ocean. It should be noted, however, that these effects do not coincide geographically and, therefore, Sc cooling does not necessarily dominate regionally.
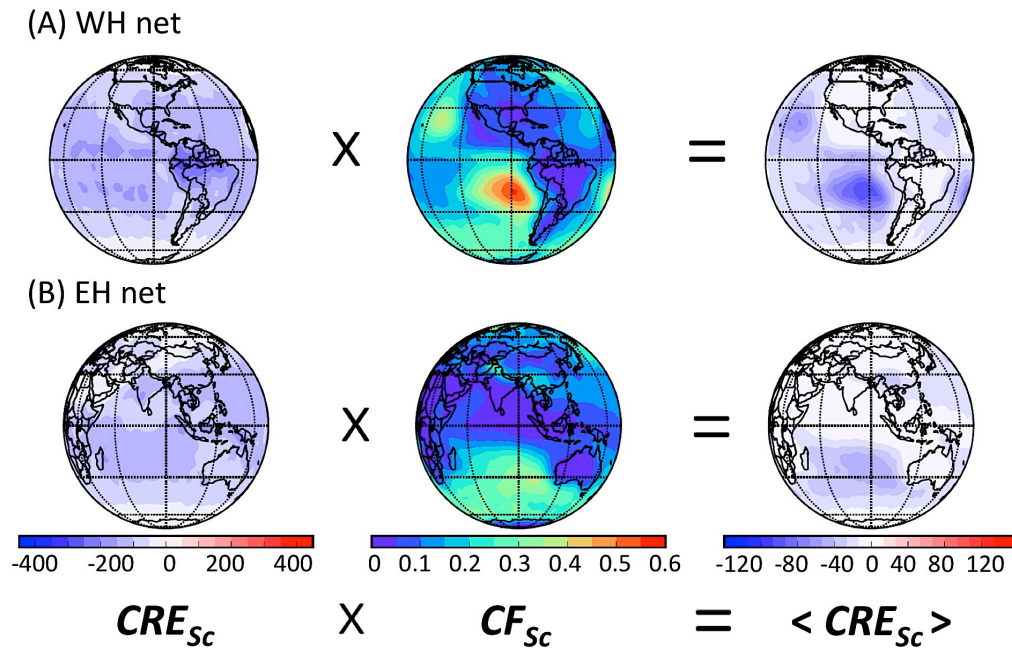
(A) WH net

(B) EH net

-400 -200 0 200 400   0 0.1 0.2 0.3 0.4 0.5 0.6   -120 -80 -40 0 40 80 120

CRE_{Sc} X CF_{Sc} = $< CRE_{Sc} >$

Figure 4.14 WH and EH net $< CRE_{Sc} >$ (W m^{-2}).

There are two other types of clouds that are also typically composed of liquid droplets. Table 4.2 is the WH LW, SW, and net $< CRE_{St} >$, $< CRE_{Sc} >$, $< CRE_{Cu} >$. St, Sc, Cu are all low clouds, which reflect solar radiation and cool the Earth. Comparing these three low clouds with their CFs in Fig. 4.4, St cloud often appears in the Southeast Pacific Ocean which results in a weak cooling effect. Sc cloud is thicker and lower than the other two clouds, which is closer to the ground and reflect more solar radiation to space. As shown in Fig. 4.4, St cloud also has a fairly large CF, especially at South Pacific Ocean. Therefore, Sc has a large cooling effect, approaching its net CRE (Sc) maximum around -

60 W m^{-2} over the Southeast Pacific Ocean. Cu cloud is observed less frequently globally.
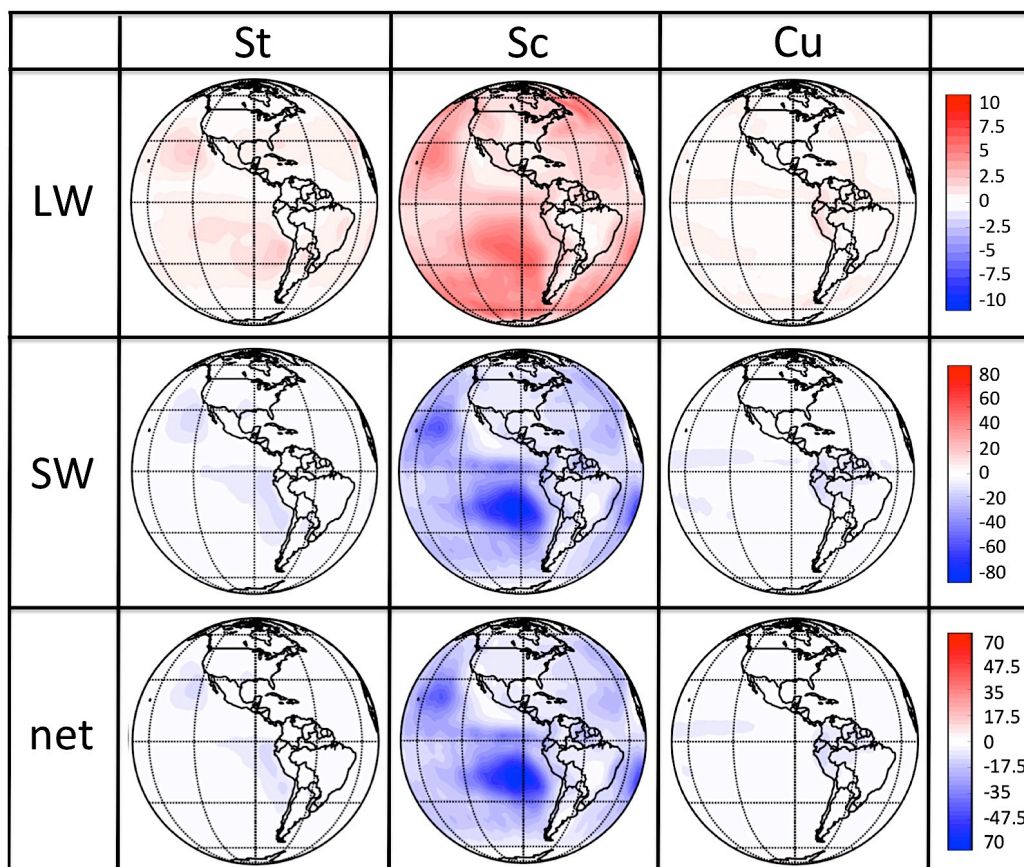

	St	Sc	Cu	
LW				
SW				
net				

Table 4.2 WH LW/SW/net $< CRE_{St} >, < CRE_{Sc} >, < CRE_{Cu} >$ (W m^{-2}).

4.2.3   Deep Convection Cloud Radiative Effect

Compared to high thin clouds and low thick clouds, deep convective clouds are thicker with a low cloud base and a high cloud top. As shown in Fig. 4.15, deep convective clouds exhibit characteristics from both of the previous examples by strongly reflecting SW radiation while also trapping LW radiation.
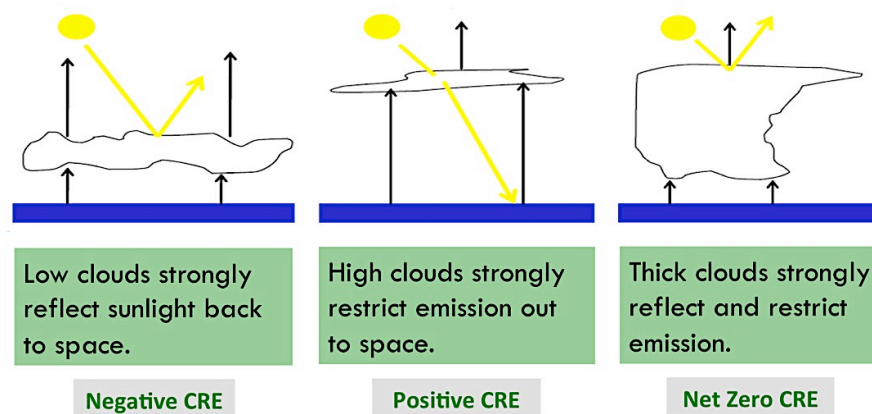
Figure 4.15 Three cloud types radiative mechanisms.

Fig. 4.16, which shows WH LW, SW, and net $< CRE_{D.C.} >$, illustrates that D.C. clouds have a strong LW warming effect at the ITCZ due to their high, cold cloud top. Compared to the warming effect from Ci clouds, D.C. cloud forcing is stronger by around 4 W m^{-2} which is comparable to the radiative forcing from doubling carbon dioxide concentrations. Fig. 4.16b illustrates that D.C. cloud also has a cooling effect due its thickness. Thick D.C. cloud reflects

much of the solar energy back to space. The SW and LW cloud forcing nearly cancel on the global average, as shown in Fig. 4.16c, while regionally the strongest net forcing is only -10 W m^{-2} at the ITCZ. While results suggest that cirrus and stratocumulus clouds exert a net warming and cooling effect, respectively, the net effect of deep convective clouds is relatively neutral by comparison.
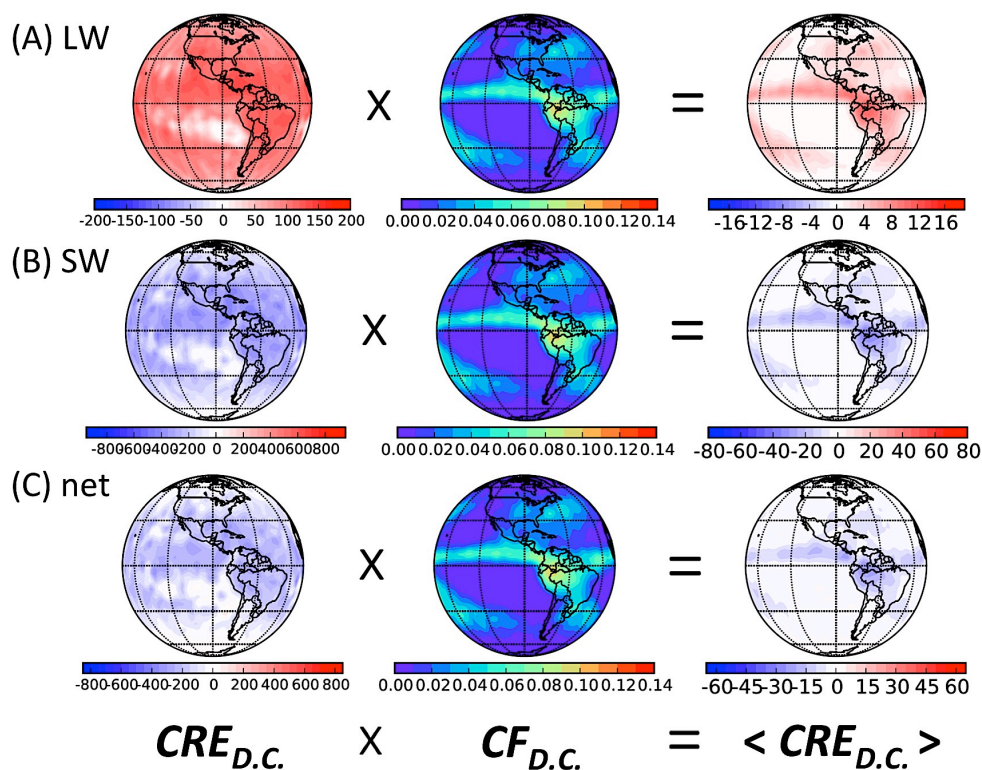
Figure 4.16 WH LW, SW, net < $CRE_{D.C.}$ > (W m^{-2}).
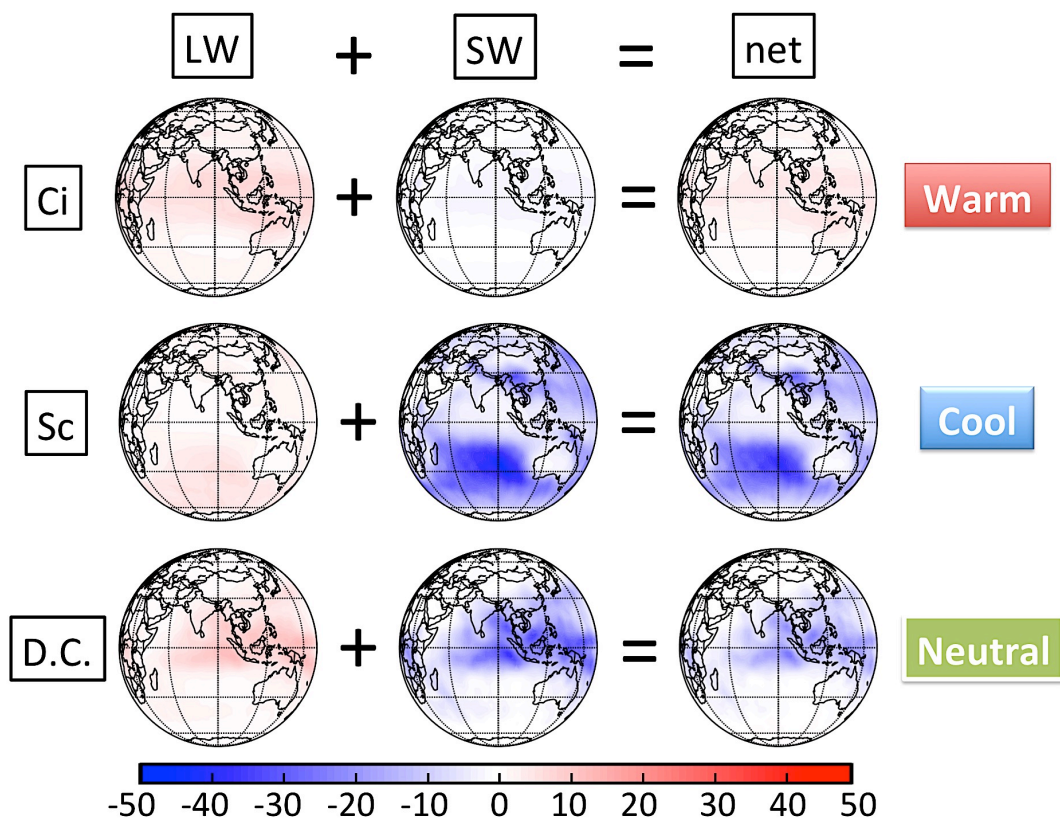
Figure 4.17 LW, SW, and net < CRE$_{Ci}$ >, < CRE$_{Sc}$ >, < CRE$_{D.C.}$ > (W m^{-2}).

Fig. 4.17 compares <CRE$_{Ci}$>, <CRE$_{Sc}$>, and <CRE$_{D.C.}$> in the Eastern Hemisphere. The first column highlights the LW effect of these three cloud types, the second column is the same thing but for SW, and the third column is net. All the globes have the same color bar. It is shown that after adding LW and SW together, the high thin Ci cloud tends to enhance the heating effect, and low thick Sc cloud has the opposite effect, while the D.C. cloud is neutral.

4.2.4 The Effects of All Cloud Types

Fig. 4.18 shows the net LW <CRE$_i$> for individual cloud types (i represents cloud type). In the Eastern Hemisphere, Ci, As, D.C., and M.L clouds have the strongest LW radiative effects over the Western Pacific Ocean and Northern Indian Ocean. Interestingly, M.L. clouds (scenes that consist of more than one cloud layer in the column) have the largest effects. Ns and M.L. cloud has a significant LW <CRE$_i$> at higher latitudes. Ac, St, Cu clouds have few LW <CRE$_i$> due to their low height and thick thickness. The total cloud LW net <CRE$_i$> has a relatively high value around 60 W m^{-2} in the tropics.
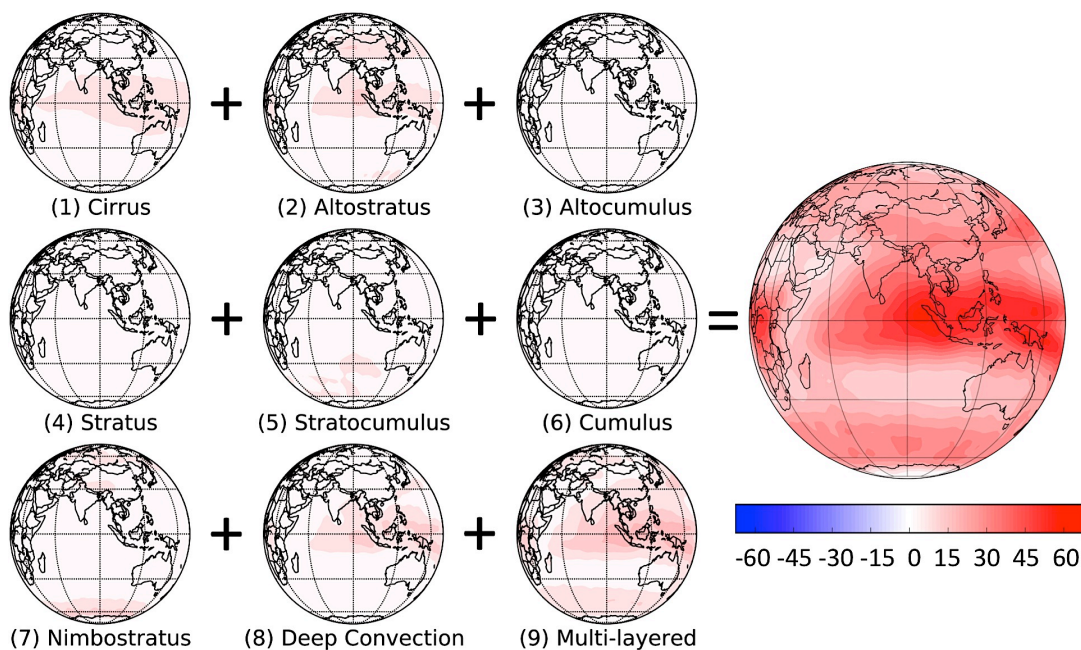
Figure 4.18 EH individual cloud type's LW <CRE$_i$> at TOA (W m^{-2}).

Fig. 4.19 shows the same thing in Fig. 4.18 but for SW $<CRE_i>$. Of the nine cloud types, Sc cloud dominates in the South Indian Ocean (-60 W m^{-2}) while D.C. (-40 W m^{-2}) and M.L. (-70 W m^{-2}) clouds dominate in the tropics. Ci, St, Cu, Ns clouds have low SW $<CRE_i>$ globally. The strongest total SW cloud forcing is -110 W m^{-2}, which is much stronger than the total LW forcing shown in Fig. 4.18.
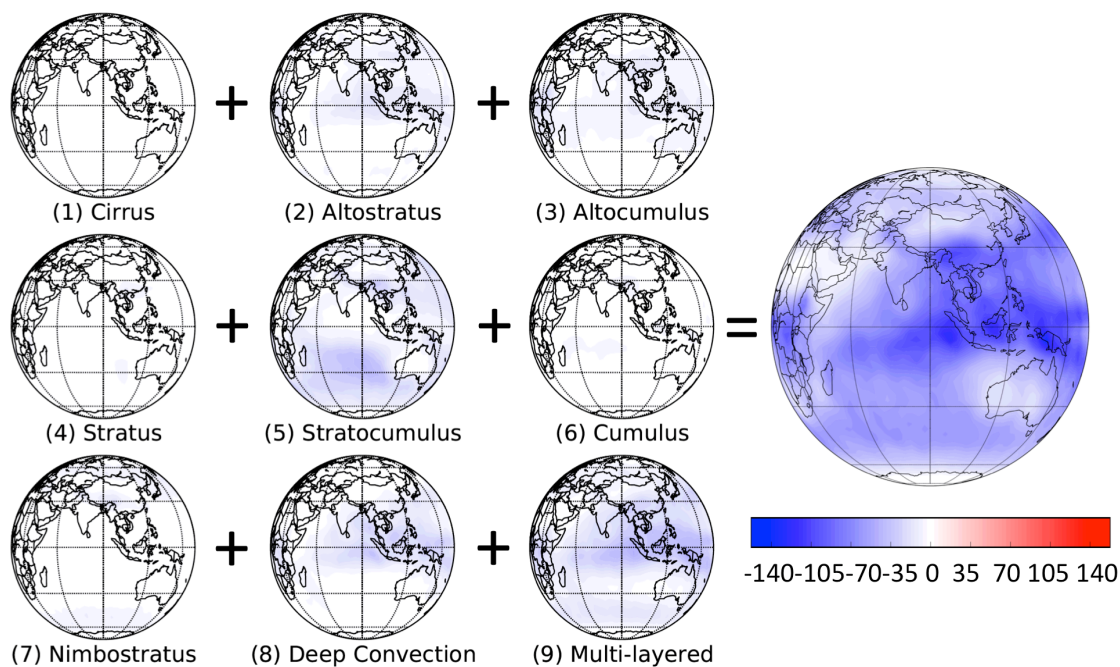
Figure 4.19 EH individual cloud type's SW $<CRE_i>$ at TOA (W m^{-2}).

Fig. 4.20 combines LW and SW $<CRE_i>$ to present the contributions of each cloud type to the net $<CRE_i>$ globally. Only Ci clouds exert a net warming

influence on the globe while the other eight cloud types exert negative $<CRE_i>$.
Overall, cloud cover leads to a cooling effect to the Earth. Among the eight
cooling globes, Sc is the strongest with a maximum value at -40 W m^{-2}. High Sc
cloud cooling effect appears in North Pacific Ocean and South Indian Ocean.
D.C. cloud has a SW $<CRE_i>$ as high as Sc cloud in previous Fig. 4.19, which
is canceled by its LW CRE(i) in Fig. 4.18 and results in a mild net $<CRE_i>$ in
tropics in Fig. 4.20. Altostratus clouds have both cooling and warming effects
depending on their location. It has positive net CRE(i) over western China and
negative CRE(i) over the tropics. Overall, the total net CRE(i) has a cooling
effect globally except northern Africa, western China, western Australia, and
pole areas. Antarctica has a positive warming effect of 20 W m^{-2}.
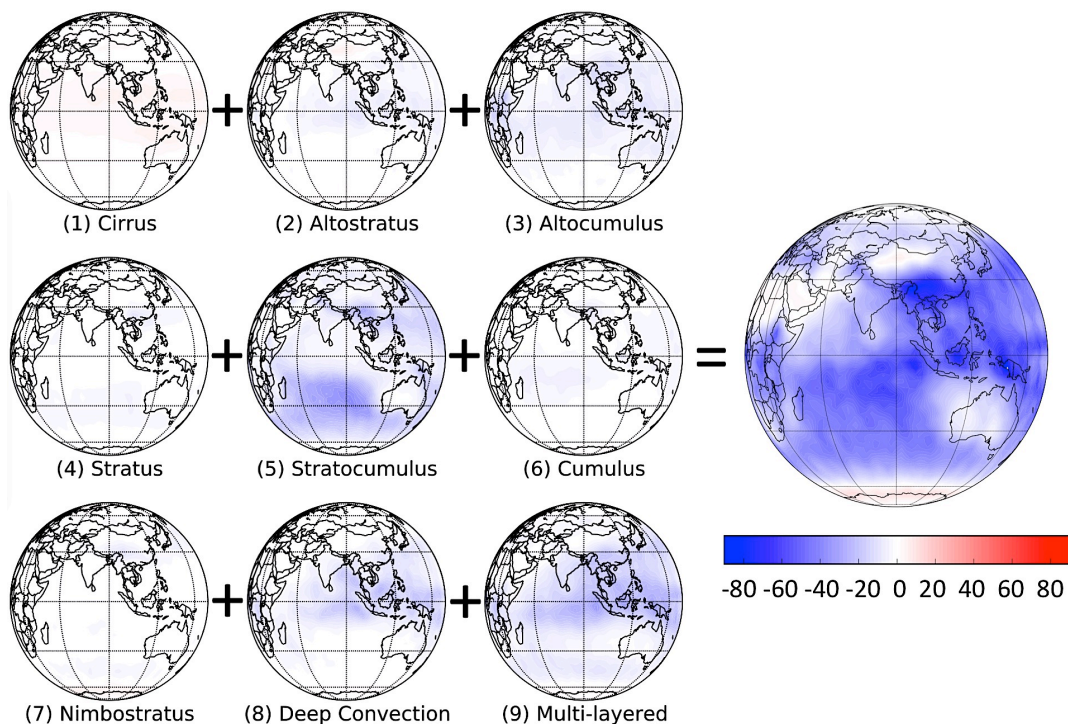
Figure 4.20 EH individual cloud type's net <CRE$_i$> at TOA (W m^{-2}).

4.3 Nine Cloud Types Radiative Kernels

Soden et al. (2007) present a method to quantify climate feedbacks through the use of "radiative kernels (K)" that describe the different response of the TOA radiative fluxes to changes in the feedback variables. The kernel allows the effects of each cloud type on TOA radiative fluxes to be partitioned into two terms – one that describes the sensitivity of the TOA flux to a change in cloud fraction and the other that quantifies the anticipated response of cloud fraction to changing SST. To the extent that cloud characteristics remain unchanged, this separation allows us to project future CRE associated with possible changes in cloud distributions in a warmer climate. Thus, the kernel is defined as follows:

$$K(i) = \frac{dCRE}{dCF(i)} = \frac{CRE(i) - \Delta CRE(i)}{\Delta CF(i)} \quad (i \text{ is cloud type}) \tag{5.1}$$

where 1% change in CF ($\Delta CF(i)$)is used to estimate the radiative effects for each cloud type in this study.

Fig. 4.21 is the radiative kernel of EH LW <CRE$_i$> with 1% change in CF. It is shown that M.L. cloud is the most sensitive one to CF, especially at Topical West Pacific (TWP) and pole areas. D.C. cloud, As cloud and Ci cloud are sensitive to CF in TWP, which gain LW <CRE$_i$> by 0.25 W m^{-2}, 0.2 W m^{-2}, and 0.1 W m^{-2} separately with the 1% increase in CF. Altostratus cloud is also sensitive in the western China while Ns cloud is more sensitive over polar regions by a 0.15 W m^{-2} increase. Overall, the total LW <CRE$_i$> is sensitive to CF change in TWP and pole areas, the largest value is about 0.7 W m^{-2} over Indonesia.

EH CloudSat/CALIPSO LW CREs with 1% change in CF 2007-2010 (W/m^2)
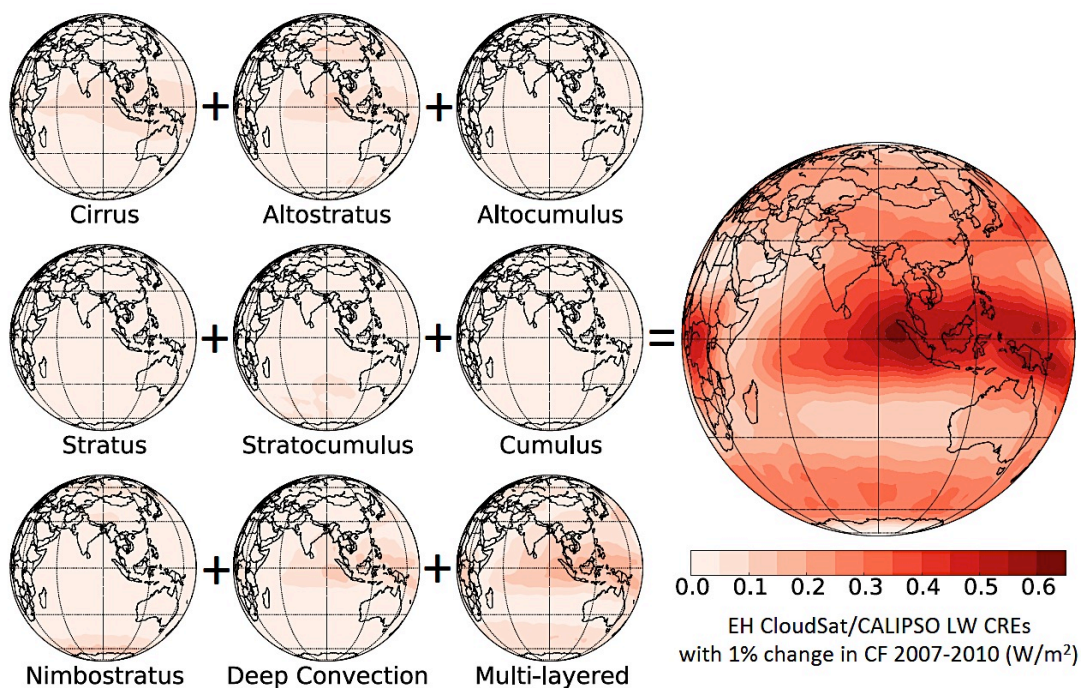
Figure 4.21 EH LW <CRE$_i$> with 1% change in CF (W m^{-2}).

Fig. 4.22 is WH CloudSat/CALIPSO SW <CRE$_i$> with 1% change in CF. With 1% increase in CF, Sc cloud, D.C. cloud and M.L. cloud SW <CRE$_i$> have large decreases. Sc cloud is sensitive to CF changes over the South Pacific Ocean, where the maximum is -1 W m^{-2}. However, M.L. cloud and D.C. cloud are sensitive to CF change at ITCZ, with a decrease by -0.6 W m^{-2} and -0.4 W m^{-2} separately. Overall, the total cloud SW <CRE$_i$> decreases globally by CF increases, the maximum is around – 1.6 W m^{-2} at the ITCZ. Compared to Fig. 4.20, SW <CRE$_i$> is more than twice as sensitive to CF than LW CREs. In conclusion, cloud types and cloud cover amount indeed matter in both LW <CRE$_i$> and SW <CRE$_i$>, especially the role of radiative cooling effect in energy balance.
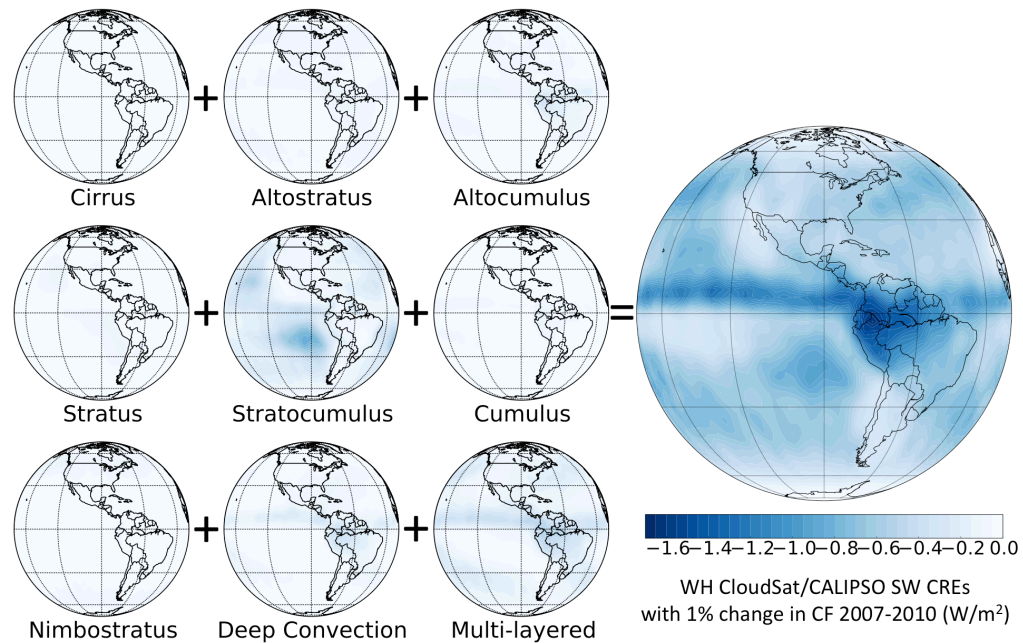
Figure 4.22 WH SW $\langle CRE_i \rangle$ with 1% change in CF (W m^{-2}).

4.3.1 Cloud Radiative Effects at the Surface

Since CloudSat/CALIPSO observe cloud vertical structure better than passive sensors, it is expected that this vertically-resolved information improves satellite-based estimates of CRE at the surface. Fig. 4.22 compares the effects of deep convective clouds on the net CRE at TOA and surface in both hemispheres. D.C. clouds reach a maximum CRE of -15 W m^{-2} at TOA while SFC CRE peaks at -25 W m^{-2}; therefore, D.C. cloud has a larger effect on

surface radiation balance than at TOA. The energy imbalance between TOA and surface due to the increasing CO_2 is absorption at surface. The Earth's surface is cooler than it would be if the atmosphere had no clouds.
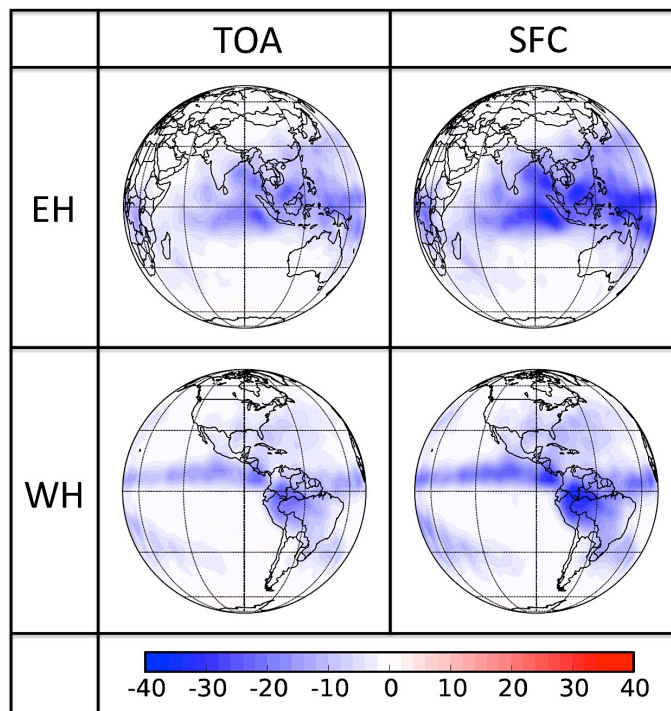
Figure 4.22 EH and WH D.C. cloud's net CRE at TOA and surface (W m^{-2}).

4.4 Cloud Impacts on Atmospheric Radiative Heating

Since we are able to measure CRE at both the top of the atmosphere and the surface, the difference can be used to estimate the impact of clouds on radiative

heating within the atmosphere, CRH is the difference in CRE at TOA minus SFC.

Fig. 4.23 presents estimates of global mean CF and atmospheric CRH from each cloud type consistent with CloudSat/CALIPSO observations from 2007 to 2010. It is seen that the whole globe clear sky fraction is 0.3, and the most frequent clouds are Sc clouds, M.L. clouds, and Ci clouds. Their CFs are about 0.16, 0.13 and 0.09 globally. For SW CRH, all clouds have warming effects, range from 0.02 to 0.18 K day^{-1}, D.C. clouds, Ns clouds, and Cu clouds have relatively large SW CRHs. For LW CRH, Ci clouds, As clouds, Ns clouds, D.C. clouds, and M.L. clouds have warming effects while the others have cooling effects. D.C. clouds and As clouds have large LW CRH around 0.38 K day^{-1} and 0.35 K day^{-1} separately. Low clouds have larger cooling LW CRH than mid and high clouds, average value is -0.25 K day^{-1}. Finally, As clouds and D.C. clouds have larger net CRHs than other clouds, at 0.45 K day^{-1} and 0.58 K day^{-1} separately. Globally, the whole average CF is 70%, SW CRH is about 0.06 K day^{-1} while LW CRH is only 0.02 K day^{-1}. Overall 70% of the Earth is covered in clouds but the net impacts on SW and LW atmospheric heating are both minimal and basically cancel leading to a negligible impact on net atmospheric radiative heating. Additionally, 0.02 K day^{-1} is probably within the error bars on the observations.
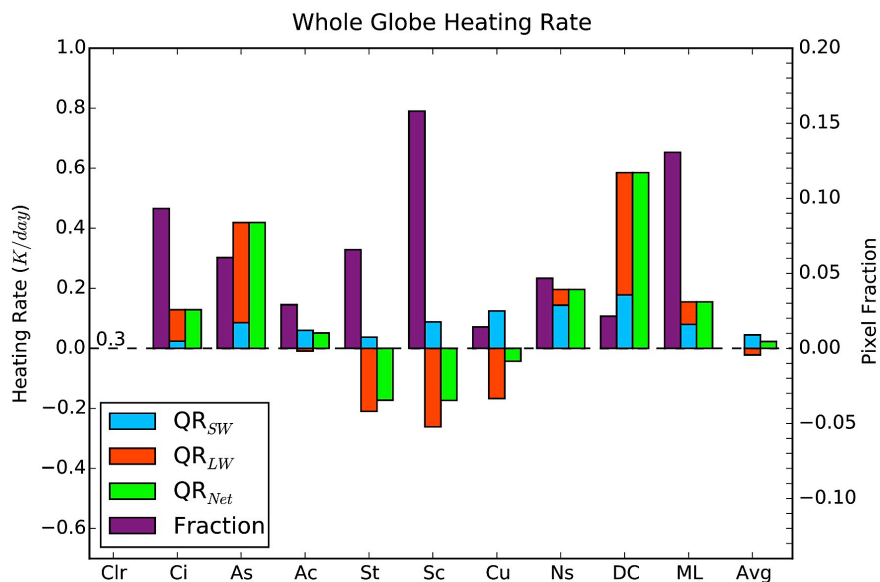
Figure 4.23 CloudSat/CALIPSO global mean CRH (K day⁻¹) and CF in 2007-2010. The X axis represents clear sky, nine cloud cloud types, and average cloud. The left Y axis represents CRH, which unit is K day⁻¹ while the right Y axis is cloud pixel fraction. The number at the first column represents clear sky fraction. Four colors of bars are shown in this chart: blue is SW CRH, red is LW CRH, green is net (LW+SW) CRH, and purple is cloud fraction.

What makes this even more remarkable is that it arises from the near perfect cancellation of a marked cloud atmospheric warming effect in tropical regions and a marked cooling at higher latitudes as shown in Fig.4.24. In the tropics, M.L. clouds, Ci clouds and Sc clouds have higher cloud fractions than the other clouds. However, D.C. clouds, As clouds, and Ns clouds are most

frequent clouds that have high net CRH at 0.95 K day^{-1}, 0.76 K day^{-1}, 0.5 K day^{-1} separately. Compared with the other three bands, tropic has the largest SW CRH. Both SW and LW CRH are positive in this area. Over the subtropics, the clear sky fraction is the highest at 0.42 among these four bands, and low clouds and M.L. clouds have large CF. This area has the lowest LW CRH on average, almost zero. Mid-latitude is the cloudiest band; Sc clouds and M.L. clouds have high fractions at 0.19 and 0.15 separately. This area has a high cooling effect due to high frequency of low clouds. Finally, the poles contribute a cooling effect to the whole globe with almost no SW heating and all clouds exhibiting high LW cooling except D.C. in this region. Given the substantial diversity in both the distribution and radiative effects of clouds globally (e.g. Fig. 4.18 and Fig. 4.19) it is somewhat remarkable that the net impact of clouds on atmospheric radiative heating nearly cancels globally.
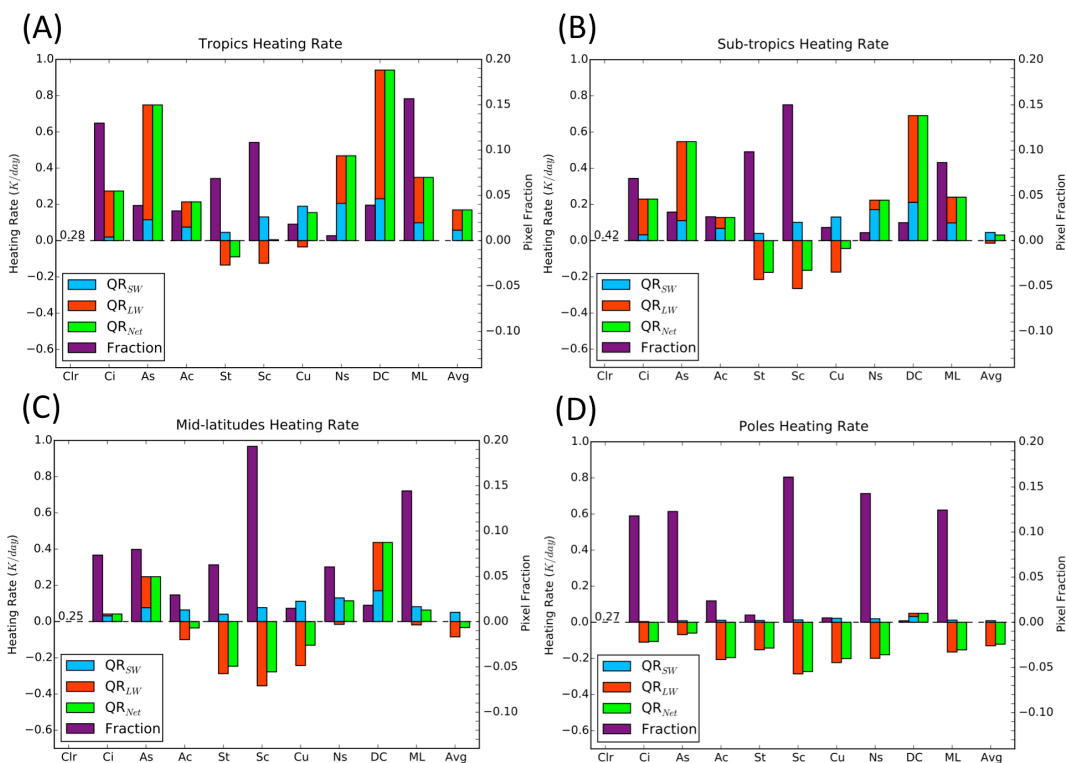
Figure 4.24 CloudSat/CALIPSO latitudinal CRH (K day⁻¹) and CF in 2007-2010: (A) Tropics, (B) Sub-tropics, (C) Mid-latitudes, (D) Poles. The tropics band is -15º to 15º, the sub-tropics are -35º to 15º and 15 º to 35 º averaged together, the mid-latitudes are -55 º to -35 º and 35 º to 55 º averaged together, and the poles are -82.5 º to -65 º and 65 º to 82.5 º averaged together.

Chapter 5

Advances Relative to Previous Assessments

Hartmann et al. (1992) combined ISCCP C1 cloud classification data and ERBE broadband energy flux data from March 1985 through February 1986 to explore the role of cloud types in the energy budget. In this chapter, we revisit this analysis but utilize four years of active sensor data from CloudSat/CALIPSO from December 2006 to August 2010.

5.1   Cloud Class Comparison

Hartmann et al. (1992) grouped the 35 possible ISCCP cloud types (Rossow and Schiffer, 1991) into five broad classes according to their cloud top pressures and visible optical depths. As shown in Fig. 5.1, pressures higher than 680 mb are considered low clouds, pressures between 440 to 680 mb represent mid cloud, and pressures lower than 440 mb are high clouds. For mid- and high-clouds, an optical depth threshold of 9.38 is used to separate thin and thick

clouds since cloud albedo is less sensitive to changes in optical depths greater than 9.38.
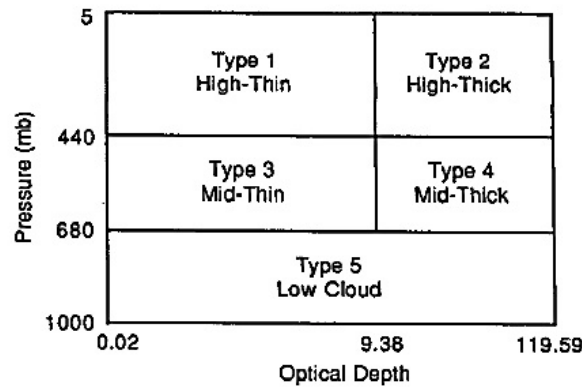
Figure 5.1 Five cloud types in Hartmann's analysis (Hartmann et al., 1992).

Fig. 5.2 presents the five cloud regimes that will be employed in this study, based on the cloud classification types identified in CloudSat's 2B-CLDCLASS-LIDAR algorithm. In this diagram, cirrus cloud is type 1 high-thin cloud; deep convective cloud and multi-layered cloud are type 2 high-thick clouds. Altostratus cloud makes up the type 3 mid-thin cloud while the combination of altocumulus and nimbostratus clouds are considered type four mid-thick clouds. Type 5 low clouds include all stratus, stratocumulus, and cumulus clouds.

Type 1 High-Thin (Ci)	Type 2 High-Thick (D.C., M.L.)
Type 3 Mid-Thin (As)	Type 4 Mid-Thick (Ac, Ns)
Type 5 Low Cloud (St, Sc, Cu)	
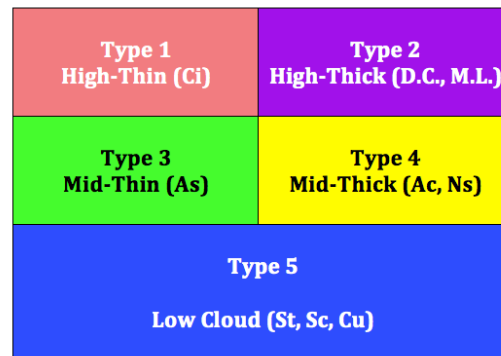
Figure 5.2 Five cloud types in this study.

5.2   Seasonal Cloud Fraction Comparison

Fig. 5.3 compares total cloud fraction in June-July-August (JJA) and December-January-February (DJF) from ISCCP and CloudSat/CALIPSO. The overall large-scale patterns of cloud cover agree very well between the two datasets. Both datasets show the highest total cloud cover over high-latitude ocean where stratus clouds predominate. There is also high cloud cover over tropical regions impacted by seasonal monsoons, including the Bay of Bengal in JJA, the Amazon Basin in DJF, and Indonesia in DJF. Compared to ISCCP, however, CloudSat/CALIPSO show a higher total CF over Europe and Africa where optically thin high and low cloud detected by the active sensors aboard CloudSat and CALIPSO are likely undetected by passive sensors.
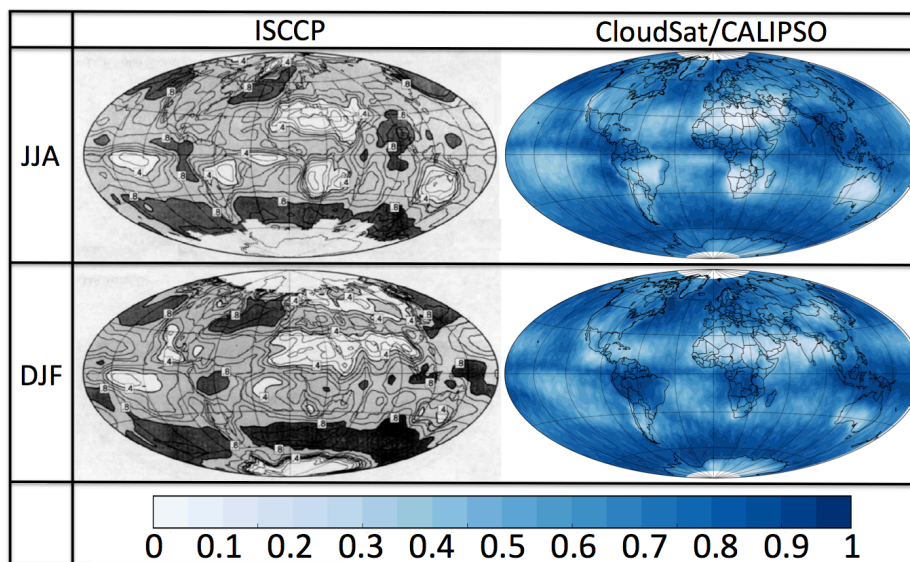
Figure 5.3 Global JJA and DJF total CF from ISCCP (contour interval 0.1, shading changes at 0.4 and 0.8) and CloudSat/CALIPSO.
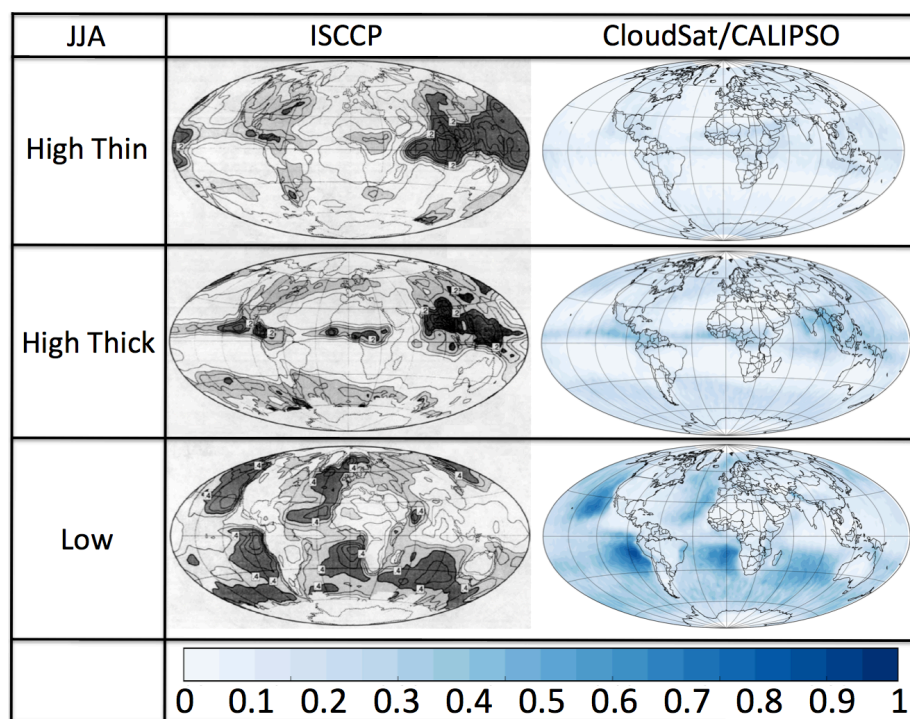
Figure 5.4 Global JJA fractions of high thin cloud, high thick cloud, and low cloud (high thin cloud: contour interval 0.05, values greater than 0.1-light shading, values greater than 0.2-heavy shading; high thick cloud and low cloud: contour interval 0.1, shading changes at 0.2 and 0.4).
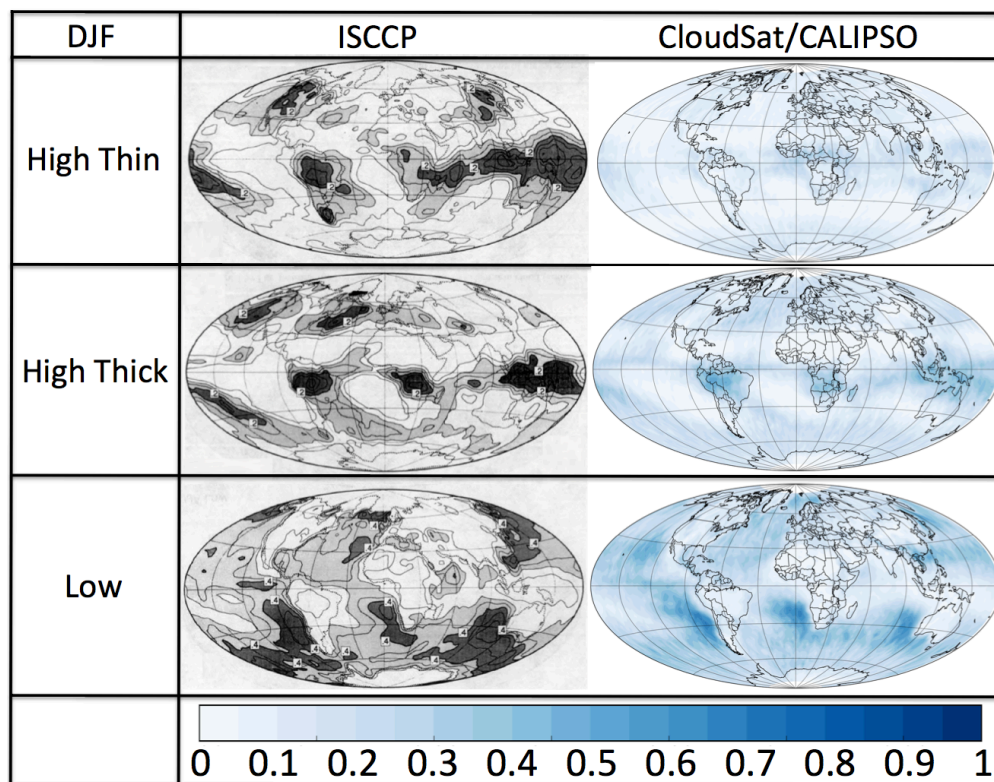
Figure 5.5 As in Fig. 5.4 except for the DJF.

To see this more clearly, Fig. 5.4 shows the global fractions of high thin cloud, high thick cloud, and low cloud for ISCCP and CloudSat/CALIPSO during summer. For high thin cloud, both datasets are in agreement that the

maximum CF is around 0.2. However, for ISCCP the cloudiest areas are South Asia and North Pacific Ocean while CloudSat/CALIPSO detect more high thin clouds over Africa. For high thick cloud, both ISCCP and CloudSat/CALIPSO agree well on the magnitudes and spatial distributions of CF. Low clouds appear to be most abundant over ocean, especially in the eastern subtropical Atlantic and Pacific. Globally, CloudSat/CALIPSO observes higher low cloud fraction than the ISCCP dataset. CALIPSO has a greater capability to detect very thin high clouds (sub-visual cirrus) that are difficult to detect using passive observations. It is also possible that CALIPSO observes more low clouds at night when ISCCP is unable to perform retrievals since it uses algorithms based on reflected sunlight.

Fig. 5.5 presents a similar comparison during the winter season, as defined as December through February. Compared to ISCCP, CloudSat/CALIPSO observes more high thin clouds over Africa. Low clouds are also more frequently observed globally by CloudSat/CALIPSO. However, ISCCP detects a greater occurrence of high thick clouds over the North Atlantic and North Pacific.

5.3   Seasonal Cloud Radiative Effect Comparison

Fig. 5.6 shows the zonally-averaged SW cloud forcing for individual cloud types, which is not provided by ISCCP+ERBE in Hartmann's (1992) results. High thin cloud (Type 1) has a negligible contribution in SW cloud forcing in both seasons due to the low optical thicknesses and high altitudes of these clouds. High thick cloud (Type 2) and low cloud (Type 5) both have large SW forcing, especially in the summer hemisphere. The contributions from high thick clouds reach a maximum in the tropics while low clouds exert the strongest radiative forcing at mid latitudes. Mid clouds have higher SW forcing at mid latitude than tropics. The total SW cloud forcing peaks at tropics during JJA, but has two maximums in mid latitudes and tropics during DJF.
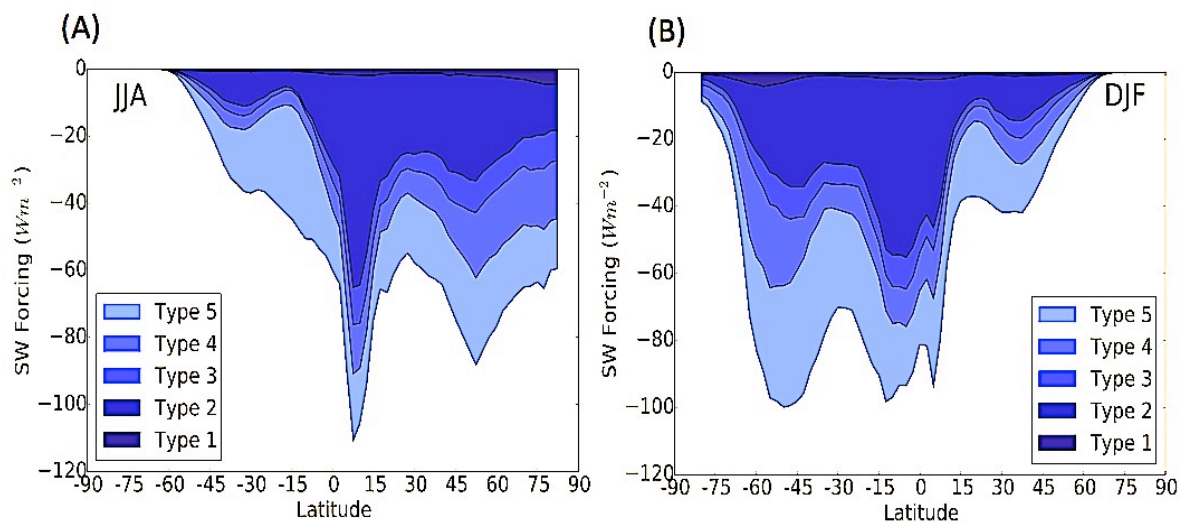
Figure 5.6 CloudSat/CALIPSO zonal average forcing of SW radiation by individual cloud types during JJA (A) and DJF (B).

Regrouping CloudSat's CLDCLASS-LIDAR cloud types into categories comparable to those defined by Hartmann et al. (1992) allow their estimates of cloud forcing to be evaluated against current, state-of-the-science spaceborne observations. Figure 5.7 shows LW cloud forcing estimated by ISCCP+ERBE (a and c) and CloudSat/CALIPSO (b and d) in JJA and DJF. The new estimates of the zonal distribution of high, thin cloud are very similar to the earlier studies in both seasons. Generally, CloudSat/CALIPSO has a lower LW cloud forcing than ISCCP+ERBE dataset. The highest LW cloud forcing of ISCCP+ERBE is 48 W m^{-2} over tropical regions while it is 12 W m^{-2} less from CloudSat/CALIPSO. Previously, there are nearly equal contributions from high, thin cloud (Type 1) and high, thick cloud (Type 2) (Fig. a and c). However, CloudSat/CALIPSO estimates of LW forcing are lower for high, thin cloud, which is 8 W m^{-2} less than ISCCP+ERBE. These two datasets exhibit good agreement on high, thick cloud (Type 2). Both mid cloud (Type 3 and Type 4) and low cloud (Type 5) have small contributions to LW cloud forcing in the SH (Fig. a and c), which is not evident in CloudSat/CALIPSO. CloudSat/CALIPSO has a lower total LW cloud forcing than ISCCP+ERBE at 30°-50° N (Fig. b and

d). For all cloud types, LW forcing reaches a minimum around 20° latitude in the winter hemisphere.
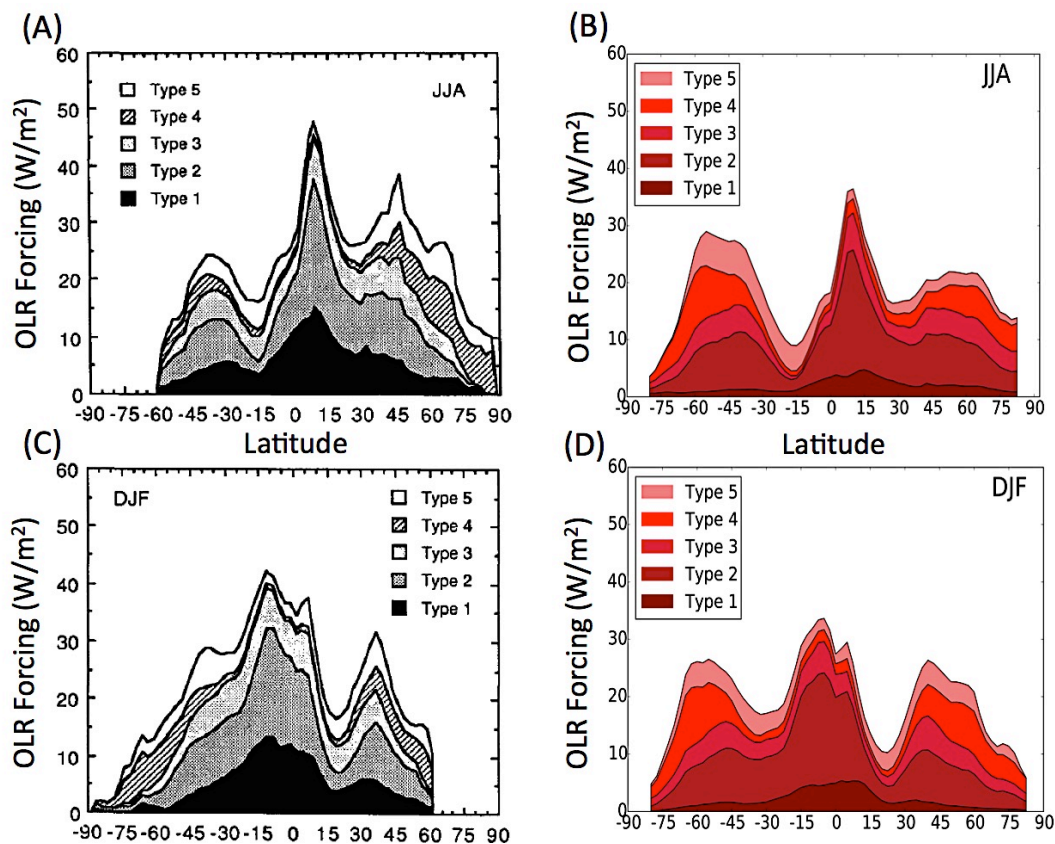
Figure 5.7 Area diagram of contributions by individual cloud types to the total zonal average LW effect of clouds on net radiation. Shaded areas indicate contributions by each cloud type to the total cloud forcing. Areas are shown cumulatively, so that the top curve represents the latitudinal distribution of total LW cloud forcing. Fig. (A) and (C) are Hartmann's (1992) results from ISCCP+ERBE, Fig. (B) and (D) are results from CloudSat/CALIPSO.
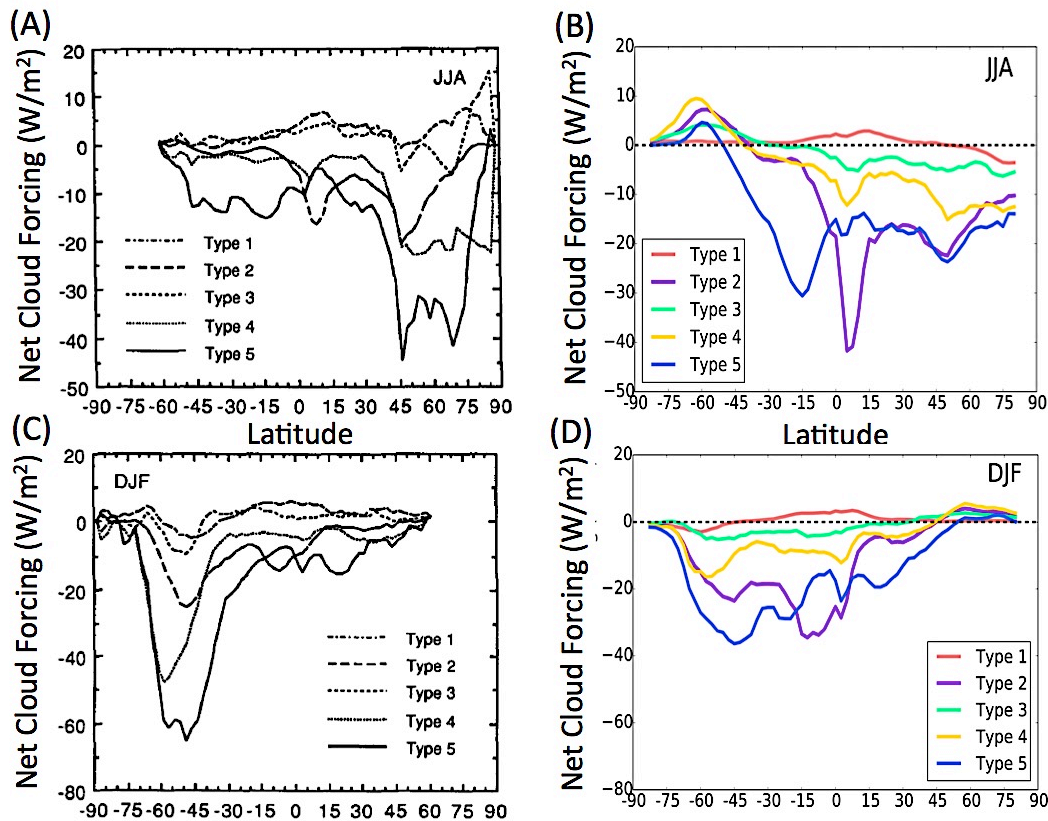
Figure 5.8 Zonal average forcing of net radiation by individual cloud types. Fig. (A) and (C) are Hartmann's (1992) results from ISCCP+ERBE, Fig. (B) and (D) are results from CloudSat/CALIPSO.

Fig. 5.8 shows the zonally-averaged net radiative forcing of the five cloud types, in which net cloud forcing represents the sum of the SW and LW components presented in Figures 5.6 and 5.7. Here the contributions of each cloud type are presented individually since the net effect is complicated by the fact that their contributions can be either positive or negative. The largest contribution to net cloud forcing is from low clouds (Type 5) in both datasets,

especially at mid latitudes in the summer hemisphere. However, CloudSat/CALIPSO estimates of net cloud forcing are comparatively weaker for low clouds (Type 5), with a maximum around 10 W m^{-2} lower than ISCCP+ERBE in the tropics during JJA and about 30 W m^{-2} lower in the mid-latitudes during DJF. This constitutes a significant difference between these datasets but can be at least partially explained by the different classifications employed. Type 2 high, thick clouds also provide large contributions to the net cloud forcing. Both ISCCP+ERBE and CloudSat/CALIPSO have a good agreement during DJF, but CloudSat/CALIPSO resolves much stronger negative forcing (- 45 W m^{-2}) in the tropical regions during JJA. The contributions from mid-level thick clouds (Type 4) also varies significantly by these two datasets in both seasons. A rationale for these differences is that some of Type 2 (high-thick) and Type 4 (mid-thick) clouds in CloudSat/CALIPSO might be misclassified as Type 5 (low) clouds by Hartmann. Passive sensors, especially the older ones used in the early ISCCP period, historically have had difficulty unambiguously determining cloud top pressure in mixed-layer and thin cloud scenarios (Mace et al., 2006). In Fig. 5.8 a and c mid-thick cloud net cloud forcing range from – 50 W m^{-2} to 0 W m^{-2} while in Fig. 5.8 b and d the values range from – 20 W m^{-2} to 10 W m^{-2}. High thin cloud and mid thin cloud provide relatively small contributions to the whole net cloud forcing in both

datasets. Only thin clouds contribute a positive cloud forcing in ISCCP+ERBE (e.g. during JJA in northern hemisphere), whereas all five cloud types have positive values in CloudSat/CALIPSO in the southern hemisphere. It can be concluded that ISCCP+ERBE and CloudSat/CALIPSO have better agreement in winter than in summer.

The differences are most likely due to differences in the classifications related to uncertainty in the ISCCP approach based on passive observations. The active sensors aboard CloudSat and CALIPSO help refine these original categories by providing more robust measures of cloud top and base height.

Comparing Fig. 5.7 and Fig. 5.8, ISCCP cloud regimes overestimates or underestimates of SW forcing relative to the new observations might due to differences in cloud classification. This can be seen in Table 5.1.

(A)

	Type 1 High, thin		Type 2 High, thick		Type 3 Mid, thin		Type 4 Mid, thick		Type 5 Low		
	JJA	DJF	JJA	DJF	JJA	DJF	JJA	DJF	JJA	DJF	Average
C_i	10.2	10.0	8.5	8.8	10.7	10.7	6.5	8.2	27.2	25.9	63.3
LW	6.5	6.3	8.4	8.8	4.8	4.9	2.4	2.4	3.5	3.5	25.8
Net	2.4	2.3	−6.4	−7.5	1.4	0.8	−6.6	−8.5	−15.1	−18.2	−27.6

(B)

	Type 1 High, thin (Ci)		Type 2 High, thick (D.C., M.L.)		Type 3 Mid, thin (As)		Type 4 Mid, thick (Ac, Ns)		Type 5 Low (St, Sc, Cu)		
	JJA	DJF	JJA	DJF	JJA	DJF	JJA	DJF	JJA	DJF	Average
C_i	8.0	9.6	14.0	15.5	6.0	6.2	7.0	8.2	25.0	23.1	61.3
LW	2.1	2.4	8.3	8.9	3.4	3.6	3.1	3.4	3.1	3.1	20.7
Net	1.0	1.1	-10.3	-12.3	-1.0	-1.2	-4.1	-5.1	-15.6	-16.4	-32.0
SW	-1.1	-1.3	-18.6	-21.2	-4.4	-4.8	-7.2	-8.5	-18.7	-19.5	-52.7

Table 5.1 Global area-averaged cloud forcing by type of cloud. LW, net and SW radiation are given in W m^{-2} and cloud fractional coverage are given in percent. The last column is the sum over all cloud types and the average of the JJA and DJF season. (A) is ISCCP+ERBE from Hartmann's (1992) work, which regions poleward of about 60° in the winter hemisphere are not included in the area average. (B) is from CloudSat/CALIPSO.

Table 5.1 shows global area-averaged cloud forcing by cloud type, where a is derived from ISCCP+ERBE, b is derived from CloudSat/CALIPSO. It is shown that ISCCP+ERBE underestimates high, thick clouds CF which might ignore multilayered clouds, and overestimates mid, thin clouds CF. Table 5.1 also indicates that low clouds from both datasets provide the largest net cloud forcing –-16 W m^{-2} of the total net cloud forcing. According to CloudSat/CALIPSO estimates, high- and midlevel thick cloud contribute -11 W m^{-2} and -5 W m^{-2}, respectively, to the net radiation, which are much higher and lower than ISCCP+ERBE. Both datasets agree that high, thick clouds make a larger contribution to net cooling per unit area than low clouds. High- and mid-level thin clouds make small contributions to global net cloud forcing, as SW and LW forcing nearly offset each other. Mid thin cloud net cloud forcing is negative in CloudSat/CALIPSO (-1 W m^{-2}) but positive in ISCCP+ERBE (5 W m^{-2}), which causes the difference in the previous zonal figures.
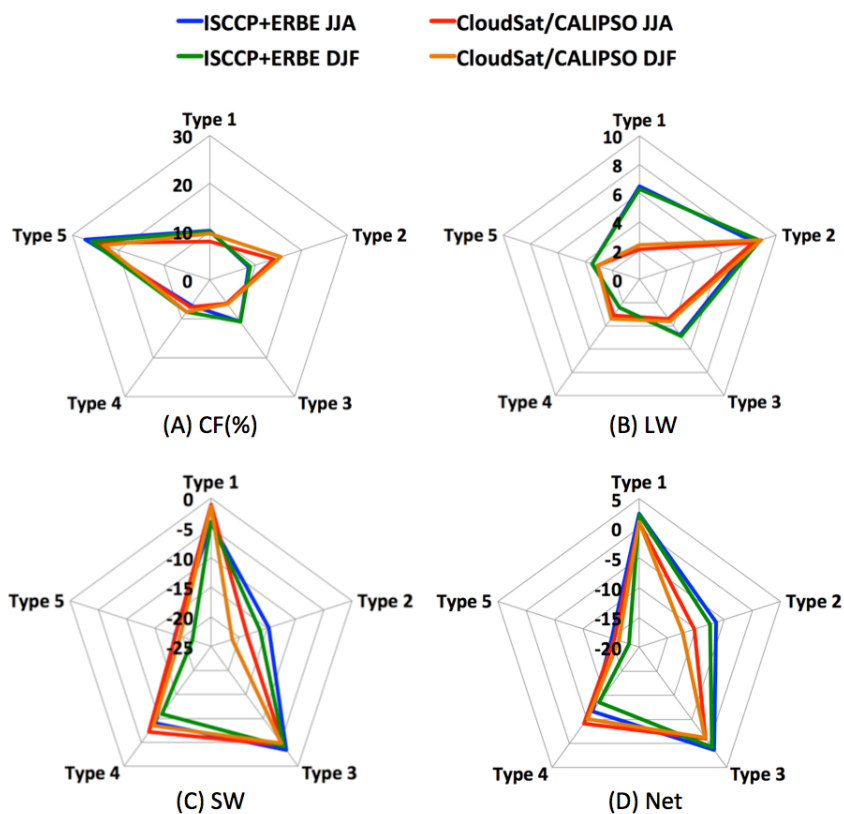
Figure 5.9 Seasonal CF (%) and SW/LW/net CRE (W m^{-2}). Type 1-5 represent five cloud types. The blue (JJA) line and green (DJF) line are derived from ISCCP+ERBE dataset, the red (JJA) line and orange (DJF) line are derived from CloudSat/CALIPSO dataset.

Fig. 5.9, which displays data from Table 5.1, indicates the seasonal

cycles of CF and CRE from both datasets. The blue (JJA) line and green (DJF)

line are derived from ISCCP+ERBE dataset and the red (JJA) line and orange

(DJF) line are derived from CloudSat/CALIPSO dataset. It is shown that CF

and LW CRE almost have no seasonal cycle while SW/net CRE varies apparently between JJA and DJF.
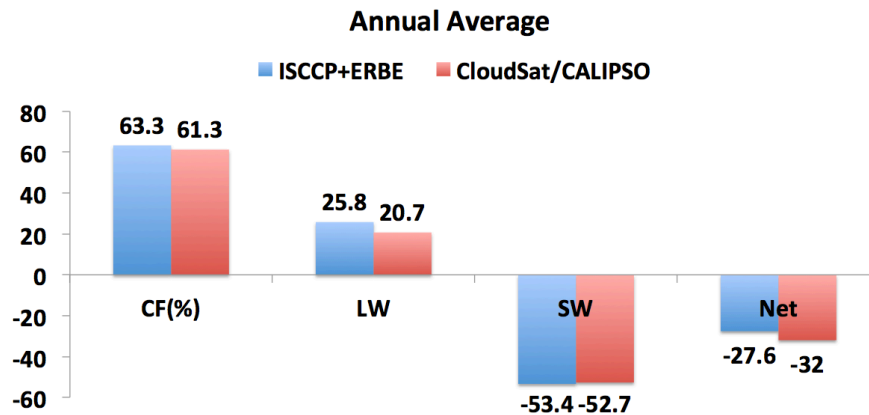
Figure 5.10 Annual average CF (%) and LW/SW/net CRE (W m^{-2}).

Fig. 5.10 shows the annual average CF and CRE from ISCCP+ERBE and CloudSat/CALIPSO derived from Table 5.1. Comparing average values from these two datasets, both have a global CF around 62%. CloudSat/CALIPSO has a 20% lower LW forcing than ISCCP+ERBE, which has a good agreement with CERES data. It can be calculated from Hartmann's (1992) results, SW average forcing is about -53 W m^{-2}, which is exactly the same in CloudSat/CALIPSO.

5.4   A Classification for a New Era

Fig. 5.11 summarizes the four-year record of zonal-mean TOA cloud forcing from CloudSat/CALIPSO by each of the nine individual cloud types. Ci, D.C., M.L., As, Ns, Sc clouds have high LW cloud forcing while D.C., M.L., Sc clouds have high SW forcing. After balance between SW and LW forcing, Fig 5.11c shows the net cloud radiative forcing. Cirrus clouds have the only warming effect among nine cloud types, peaking at about 4 W m^{-2} in the tropics. Stratus clouds contribute the largest cooling effect to the total net cloud radiative forcing; the maximum is -25 W m^{-2} at mid latitudes. D.C. clouds have high SW forcing in the tropics where it is balanced by its LW forcing. Mid clouds exert significant cooling effects on global energy balance.
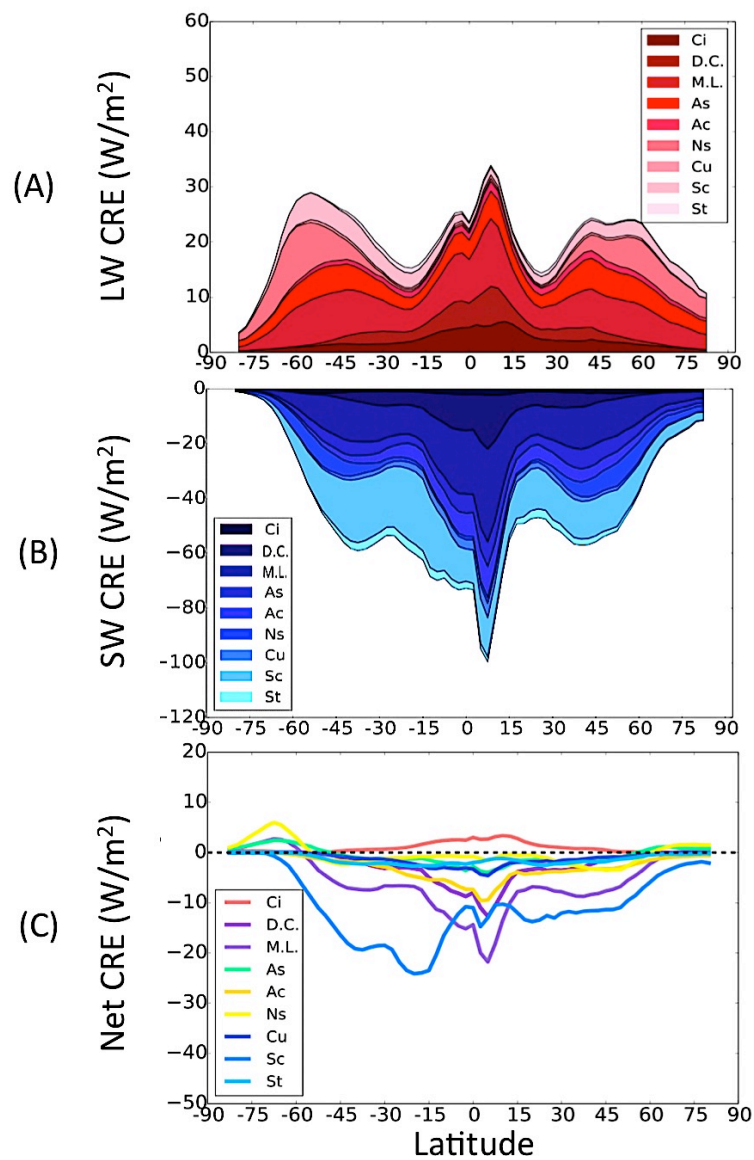
Figure 5.11 CloudSat/CALIPSO zonal average forcing of LW, SW and net radiation by individual cloud type.

Figure 5.12 summarizes how each of the CloudSat/CALIPSO cloud types

contributes to the global mean LW, SW, and net CRE. The four-year full

seasons result is consistent to previous seasonal results. Total LW forcing is 21.6 W m^{-2}, Ci, M.L., and As clouds contribute the most parts. Total SW forcing is -53.4 W m^{-2}, Sc cloud accounts for nearly 30% of the total amount. After adding SW and LW forcing together, the total net forcing is -31.8 W m^{-2}. Cirrus cloud is the only cloud type which exerts a warming effect on energy balance. Stratocumulus cloud has the most significant cooling effect of about -13 W m^{-2}, which accounts for more than 40% of the total cloud forcing. M.L., Ac, D.C. clouds also have significant cooling effects.
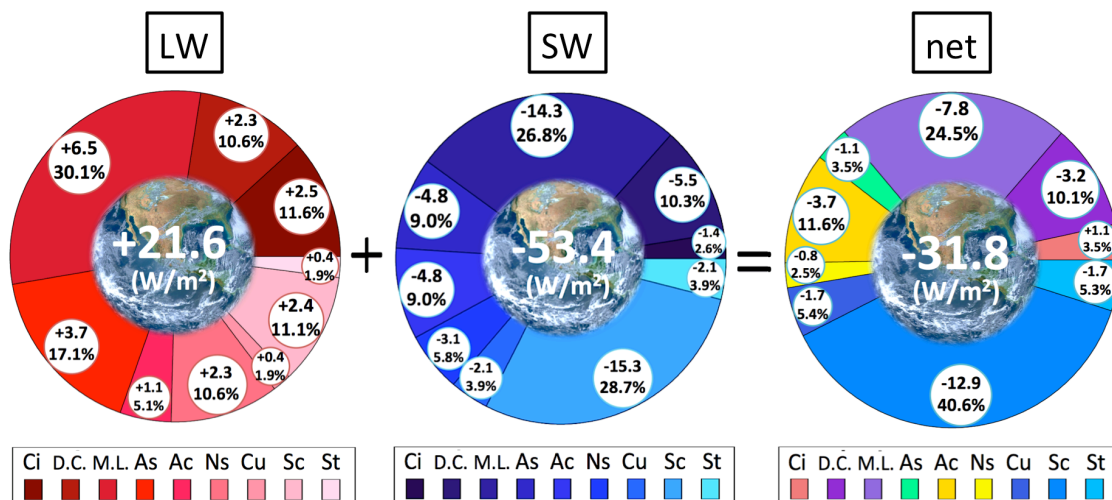
Figure 5.12 CloudSat/CALIPSO latitude weighted cloud radiative forcing of LW, SW and net radiation by individual cloud type.

Chapter 6

Summary and Future Work

6.1 Summary and Conclusion

Atmospheric clouds contribute a significant source of uncertainty in our ability to predict future climate. Improved representation of cloud radiative processes in global models is the key to reducing these uncertainties. Multi-sensor observations from the A-Train satellite constellation provide observational constraints needed to reduce uncertainties in model simulations of cloud radiative effects.

CloudSat's new multi-sensor radiative flux and heating rates product (2B-FLXHR-LIDAR) is used to evaluate cloud radiative effects globally. This approach leverages the capability of CloudSat and CALIPSO to retrieve vertically-resolved estimates of clouds properties. Whereas previous satellite-based assessments are typically limited to daytime cloud-free measurements of clouds properties, the 2B-FLXHR-LIDAR data product has the ability to quantify cloud radiative effects over thick low clouds, under thin cirrus, and at

night.

Based on the 2B-FLXHR-LIDAR data product, the nine distinct cloud types are grouped and compared with passive sensors including those from the International Satellite Cloud Climatology Project (ISCCP) and Earth Radiation Budget Experiment (ERBE) archives. The effects of three common cloud classes are highlighted in detail: cirrus, stratocumulus, and deep convection, to contrast their dramatically different effects on climate. The findings support the qualitative conclusion that cirrus clouds warm the planet and stratocumulus clouds cool the planet, while the longwave and shortwave cloud radiative effect of deep convective cloud cancel each other in the tropics. In addition, the new CloudSat/CALIPSO estimate of annual average shortwave forcing is -53 W m^{-2} in good agreement with previous estimates but CloudSat/CALIPSO observations suggest a 20% lower longwave forcing than other sources. This analysis provides an improved distinction of the radiative effects of low-level clouds, and the cloud boundary information from the active sensors used greatly enhances our ability to accurately discern cloud forcing at the Earth's surface.

6.2   Future Work

Except cloud radiative effect, 2B-FLXHR-LIDAR product can also be used to calculate cloud heating rate profiles. Previously, Haynes (2013) et al. explored radiative heating characteristics of earth's cloudy atmosphere. Fig. 6.1 is CloudSat/CALIPSO total cloud longwave cloud radiative heating during DJF. The future work will analyze clouds heating rate profiles classified by cloud types based on his results.
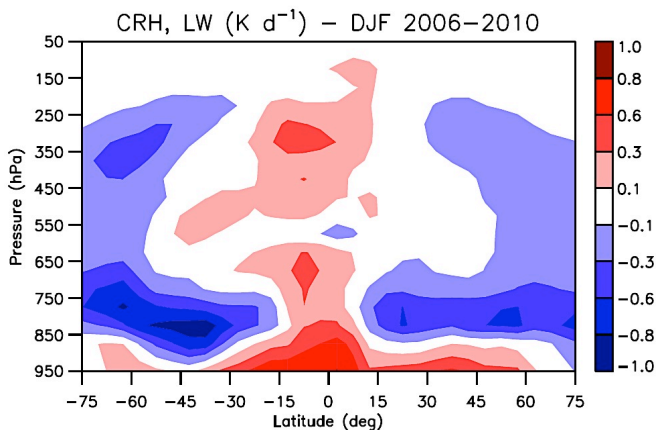
Figure 6.1 LW CRH, DJF 2006-2010 (Haynes et, al., 2013).

Bibliography

Ackerman T. P. and G. M. Stokes, 2003: The Atmospheric Radiation Measurement Program, *Physics Today*, 56(1): 38-44.

Andreae, M. O., D. Rosenfeld, P. Artaxo, A. A. Costa, G. P. Frank, K. M. Longo, M. A. F. Silva-Dias, 2004: Smoking Rain Clouds over the Amazon, *Science*, 303, 1337- 1342.

Barker, H. W., J. N. S. Cole, J.-J. Morcrette, R. Pincus, P. Raisaenen, K. von Salzen, and P. A. Vaillancourt, 2008: The Monte Carlo Independent Column Approximation: An assessment using several global atmospheric models, *Q. J. R. Meteorol. Soc.*, 134, 1463–1478.

Barkstrom, B. at al., 1989: Earth Radiation Budget Experiment, *Bulletin American Meteorological Society*, 70(10), 1254-1262.

Bodas-Salcedo, A., et al., 2013: Origins of the Solar Radiation Biases over the Southern Ocean in CFMIP2 Models. *Journal of Climate*, 27, 41–56.

Boucher, O., and D. Randall, 2014: Clouds and Aerosols. *IPCC Fifth Assessment Report*, Chapter 7.

Calisto M., D. Folini, M. Wild, and L. Bengtsson 2014: Cloud radiative forcing intercomparison between fully coupled CMIP5 models and CERES satellite data, *Annales Geophysicae*, 32, 793-807.

Ceppi P., Y. Hwang, D. M. W. Frierson, and D. L., 2012: Hartmann, Southern Hemisphere Jet Latitude Biases in CMIP5 Models Linked to Shortwave Cloud Forcing, *Geophysical Research Letters*, 39, L19708.

Cess, R. D., and Coauthors, 1990: Intercomparison and interpretation of cloud climate feedback processes in nineteen atmospheric general circulation models. *J. Geophys. Res.*, 95, 601–615.

Chen, T., W. B. Rossow, and Y. Zhang, 1999: Radiative Effects of Cloud-Type Variations, *Journal of Climate*, 13, 264–286.

Comstock J. M. and T. P. Ackerman, 2002: Ground-based lidar and radar remote sensing of tropical cirrus clouds at Nauru Island: Cloud statistics and radiative impacts, *J. Geophys. Res.*, 107, D23, doi:10.1029/2002JD002203.

Dong, X. Q., et al., 2006: A climatology of midlatitude continental clouds from the ARM SGP central facility. Part II: Cloud fraction and surface radiative forcing, *Journal of Climate*, 19, 1765–1783.

Hahn, C. J., S. G. Warren, J. London, 1995: The Effect of Moonlight on Observation of Cloud Cover at Night, and Application to Cloud Climatology, *Journal of Climate*, 8, 1429-1446.

Hartmann, D. L., M. E. Okhert-Bell, and M. L. Michelson, 1992: The effect of cloud type on Earth's energy balance: Global analysis, *Journal of Climate*, 5, 1281–1304.

Harrison, E. F., P. Minnis, B. R. Barkstrom, V. Ramanathan, R. D. Cess, and G. G. Gibson, 1990: Seasonal variation of cloud radiative forcing derived from the Earth Radiation Budget Experiment. *J. Geophys*. Res., 95, 18 687–18 703.

Harrop, B. E. and D. L. Hartmann, 2016: The Role of Cloud Radiative Heating in Determining the Location of the ITCZ in Aquaplanet Simulations. *Journal of Climate*, 29, 2741–2763.

Haynes, J. M. and G. L. Stephens, 2007: Tropical Oceanic Cloudiness and the Incidence of Precipitation: Early Results from CloudSat, *Geophysical Research Letters*, 34, L09811.

——, J. M., and C. Jakob et al., 2011: Major Characteristics of Southern Ocean Cloud Regimes and Their Effects on the Energy Budget, *Journal of Climate*, 24, 5061-5080.

——, J. M., T. H. Vonder Haar, T. L'Ecuyer, and D. Henderson, 2013: Radiative heating characteristics of Earth's cloudy atmosphere from vertically resolved active sensors, *Geophys. Res. Lett.*, 40, 624–630, doi:10.1002/grl.50145.

Henderson, D. S. and T. S. L'Ecuyer, 2011: Level 2B Fluxes and Heating Rates and 2B Fluxes and Heating Rates w / Lidar Process Description and Interface Control Document. *Tech. Rep. D*, 1–28 pp.

——, T. L'Ecuyer, G. Stephens, P. Partain, and M. Sekiguchi, 2013: A multi-sensor perspective on the radiative impacts of clouds and aerosols, *J. Appl. Meteorol. Climatol.*, 52, 853–871, doi:http://dx.doi. org/10.1175/JAMC-D-12-025.1.

Im, E., C. Wu, S. L. Durden, 2005: Cloud Profiling Radar for the CloudSat Mission*, IEEE International Radar Conference*, 483-486.

Johansson, E., A. Devasthale, T. L'Ecuyer, A. M. L. Ekman, and M. Tjernström, 2015: The Vertical Structure of Cloud Radiative Heating over the Indian Subcontinent during Summer Monsoon, *Atmos. Chem. Phys.*, 15, 11557–11570.

Kay, J. E., K. Raeder, A. Gettelman, and J. Anderson, 2011: The boundary layer response to recent Arctic sea ice loss and implications for high-latitude climate feedbacks. *Journal of Climate*, 24, 428–447.

——, T. L'Ecuyer, A. Gettelman, G. Stephens, and C. O'Dell, 2008: The contribution of cloud and radiation anomalies to the 2007 Arctic sea ice extent minimum. *Geophysical Research Letters*, 35, L08503.

Kiehl, J. T. and K. E. Zhang, 1997: Earth's Annual Global Mean Energy Budget. *Bulletin of the American Meteorological Society*, 78, 197-208.

Klein, S. A., Zhang, Y., Zelinka, M. D., Pincus, R., Boyle, J., and Gleckler, P. J., 2013: Are climate model simulations of clouds improving? An evaluation using the ISCCP simulator, *J. Geophys. Res*., 118, 1329–1342.

Kotarba, A. Z., 2009: A Comparison of MODIS-derived Cloud Amount with Visual Surface Observations*, Atmospheric Research*, 92, 522-530.

L'Ecuyer, T. S., and J. H. Jiang, 2010: Touring the atmosphere aboard the A-Train, *Phys. Today,* 63, 36–41.

——, N. B. Wood, T. Haladay, G. L. Stephens, and P. W. Stackhouse, 2008: Impact of clouds on atmospheric heating based on the R04 CloudSat fluxes and heating rates data set, *J. Geophys. Res.,* 113, D00A15, doi:10.1029/2008JD009951.

Li, Y., R. Yu, Y. Xu et al., 2004: Spatial Distribution and Seasonal Variation of Cloud over China Based on ISCCP Data and Surface Observations, *Journal of the Meteorological*

Society of Japan, 82, 761-773.

Lin, L., Q. Fu, Zhang, J. Su, Q. Yang, Z. Sun, 2013: Upward mass fluxes in tropical upper troposphere and lower stratosphere derived from radiative transfer calculations, *Journal of Quantitative Spectroscopy & Radiative Transfer*, 117, 114-122.

Liu, L., X. Sun, T. Gao, S. Zhao, 2013: Comparison of Cloud Properties from Ground-Based Infrared Cloud Measurement and Visual Observations, *Journal of Atmospheric and Oceanic Technology*, 30, 1171-1179.

Loeb, N. G., N. Manalo-Smith, 2005: Top-of-Atmosphere Direct Radiative Effect of Aerosols over Global Oceans from Merged CERES and MODIS Observations, *Journal of Climate*, 18, 3506-3526.

Mace. G. G., S. Benson, and K. L. Sonntag et al., 2006: Cloud radiative forcing at the Atmospheric Radiation Measurement Program Climate Research Facility: 1. Technique, validation, and comparison to satellite-derived diagnostic quantities, *J. Geophys. Res*., 111, d11S90.

——, S. Benson, and E. Vernon, 2006: Cirrus clouds and the largescale atmospheric state: Relationships revealed by six years of ground-based data. *Journal of Climate*, 19, 3257–3278.

——, Q. Q. Zhang, M. Vaughan, R. Marchand, G. Stephens, C. Trepte, and D.Winker, 2009: A description of hydrometeor layer occurrence statistics derived from the first year of

merged Cloudsat and CALIPSO data. *J. Geophys. Res*., 114, D00A26.

Naud, C. M., A. Del Genio, G. G. Mace, S. Benson, E. E. Clothiaux, and P. Kollias, 2008: Impact of dynamics and atmospheric state on cloud vertical overlap. *Journal of Climate*, 21, 1758–1770.

Pincus, R., R. Hemler, and S. A. Klein, 2006: Using stochastically generated subcolumns to represent cloud structure in a large-scale model. *Mon. Weather Rev.,* 134, 3644–3656.

Platnick et al., 2003: The MODIS Cloud Products: Algorithms and Examples From Terra, *IEEE,* 41(2), 459-473.

Protat, A., A. Armstrong, M. Haeffelin, Y. Morille, J. Pelon, J. Delanoe, and D. Bouniol, 2006: Impact of conditional sampling and instrumental limitations on the statistics of cloud properties derived from cloud radar and lidar at SIRTA. *Geophysical Research Letters*, 33, L11805, doi:10.1029/2005GL025340.

—— et al., 2010: The Evaluation of CloudSat and CALIPSO Ice Microphysical Products Using Ground-Based Cloud Radar and Lidar Observations, *Journal of Atmospheric and Oceanic Technology,* 27, 794-810.

Ramanathan, V., 1987: The Role of Earth Radiation Budget Studies in Climate and General Circulation Reaserch, *J. Geophys. Res*., 92, 4075-4095.

——, R. D. Cess, E. F. Harrison, P. Minnis, B. R. Barkstrom, and D. L. Hartmann, 1989: Cloud-radiative forcing and climate: Results from the Earth Radiation Budget Experiment. *Science*, 243, 57–63.

Rose G. F. and D. A. Rutan et al., 2013: An Algorithm for the Constraining of Radiative Transfer Calculations to CERES-Observed Broadband Top-of Atmosphere Irradiance, *Journal of Atmospheric and Oceanic Technology,* 30, 1091- 1106.

Shonk, J. K. P., R. J. Hogan, and J. Manners, 2012: Impact of improved representation of horizontal and vertical cloud structure in a climate model. *Clim. Dyn.,* 38, 2365–2376.

Sohn B. and E. A. Smith, 1992: The Significance of Cloud-Radiative Forcing to the General Circulation on Climate Time Scales–A Satellite Interpretation, *Journal of the Atmospheric Sciences*, 845–860.

Rossow, W. B., and R. A. Schiffer, 1991: ISCCP cloud data products. *Bull. Amer. Meteor. Soc.,* 72, 2–20.

——, A. W. Walker, L. C. Garder, 1993: Comparison of ISCCP and Other Cloud Amounts, *Journal of Climate*, 6, 2394-2418.

Sassen, K., and B. S. Cho, 1992: Subvisual-thin cirrus lidar dataset for satellite verification and climatological research. *J. Appl. Meteor*., 31, 1275–1285.

Shaw, J. A., et al., 2005: Radiometric cloud imaging with an uncooled microbolometer thermal infrared camera, *Opt. Express*, 13, 5807– 5817.

Shupe, M. D., and J. M. Intrieri, 2004: Cloud radiative forcing of the Arctic surface: The influence of cloud properties, surface albedo, and solar zenith angle*, Journal of Climate,* 17, 616– 628.

Sommeria, G., and J. W. Deardorff, 1977: Subgrid-scale condensation in models of nonprecipitating clouds. *J. Atmos. Sci*., 34, 344–355.

Stephen, S and R. Toumi, 2008: Direct observation of cloud forcing by ground-based thermal imaging, *Geophysical Research Letters*, 35, L07814.

Stephens, G. L. and T. J. Greenwald, 1991: The Earth's Radiation Budget and Its Relation to Atmospheric Hydrology 2: Observations of Cloud Effects. *Journal of Geophysical Research*, 15, 325-340.

——, 2005: Cloud Feedbacks in the Climate System: A Critical Review, *Journal of Climate*, 18, 237–273.

——, et al., 2008: CloudSat mission: Performance and early science after the first year of operation*, J. Geophys. Res*., 113, D00A18, doi:10.1029/2008JD009982.

Su, H., J. H. Jiang, D. G. Vane, and G. L. Stephens, 2008: Observed vertical structure of tropical oceanic clouds sorted in large-scale regimes, *Geophys. Res. Lett.,* 35, L24704, doi:10.1029/2008GL035888.

Thurairajah, B., and J. A. Shaw, 2005: Cloud statistics measured with the infrared cloud imager (ICI), IEEE Trans. *Geosci. Remote Sens*., 43, 2000– 2007.

Town, M. S., et al., 2007: Cloud cover over the South Pole from visual observations, satellite retrievals, and surface-based infrared radiation measurements*, Journal of Climate*, 20, 544– 559.

Trenberth, K. E., et al., 2009: Earth's Global Energy Budget, *Bulletin of the American Meteorology Society ,* 90:3, 311-323.

Wang, Z., Vane D., et al., 2013: Deborah V., et al. Level 2 Combined Radar and Lidar Cloud Scenario Classification Product Process Description and Interface Control Document. CloudSat Project Jet Propulsion Laboratory, Pasadena California.

Watanabe, M., S. Emori, M. Satoh, and H. Miura, 2009: A PDF-based hybrid prognostic cloud scheme for general circulation models. *Clim. Dyn*., 33, 795–816.

Winker, M. D., J. R. Pelon, M. P. McCormick, 2003: CALIPSO mission: spaceborne lidar for observation of aerosols and clouds, *SPIE*, 4893.

Zhang, M. H., Lin, W. Y., Klein, S. A., Bacmeister et al., 2005: Comparing clouds and their seasonal variations in 10 Atmospheric General Circulation Models with Satellite measurements, *J. Geophys. Res*., 110, D15S02, doi:10.1029/2004JD005021.

Zhang, Y., W. B. Rossow, A. A. Lacis, 1995: Calculation of Surface and Top of Atmosphere radiative fluxes from physical quantities based on ISCCP data sets 1. Method and sensitivity to input data uncertainties, *J. Geophys. Res*., 100, 1149-1165.